저작자표시-비영리-변경금지 2.0 대한민국

이용자는 아래의 조건을 따르는 경우에 한하여 자유롭게

- 이 저작물을 복제, 배포, 전송, 전시, 공연 및 방송할 수 있습니다.

다음과 같은 조건을 따라야 합니다:

저작자표시. 귀하는 원저작자를 표시하여야 합니다.

비영리. 귀하는 이 저작물을 영리 목적으로 이용할 수 없습니다.

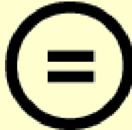
변경금지. 귀하는 이 저작물을 개작, 변형 또는 가공할 수 없습니다.

- 귀하는, 이 저작물의 재이용이나 배포의 경우, 이 저작물에 적용된 이용허락조건을 명확하게 나타내어야 합니다.
- 저작권자로부터 별도의 허가를 받으면 이러한 조건들은 적용되지 않습니다.

저작권법에 따른 이용자의 권리는 위의 내용에 의하여 영향을 받지 않습니다.

이것은 이용허락규약(Legal Code)을 이해하기 쉽게 요약한 것입니다.

Disclaimer

dCollection

[UCI]I804:31001-200000108665

ULSAN NATIONAL INSTITUTE OF
SCIENCE AND TECHNOLOGY

Doctoral Thesis

COUPLED SPIN-CHARGE TRANSPORT IN DOPED-GRAPHENE

Jungmin Park

Department of Materials Science and Engineering

Graduate School of UNIST

2018

ULSAN NATIONAL INSTITUTE OF
SCIENCE AND TECHNOLOGY

COUPLED SPIN-CHARGE TRANSPORT IN DOPED-GRAPHENE

Jungmin Park

Department of Materials Science and Engineering

Graduate School of UNIST

ULSAN NATIONAL INSTITUTE OF
SCIENCE AND TECHNOLOGY

COUPLED SPIN-CHARGE TRANSPORT IN DOPED-GRAPHENE

A thesis/dissertation
submitted to the Graduate School of UNIST
in partial fulfillment of the
requirements for the degree of
Doctor of Philosophy

Jungmin Park

July. 06. 2018 of submission

Approved by

Advisor
Jung-Woo Yoo

ULSAN NATIONAL INSTITUTE OF
SCIENCE AND TECHNOLOGY

COUPLED SPIN-CHARGE TRANSPORT IN DOPED-GRAPHENE

Jungmin Park

This certifies that the thesis/dissertation of Jungmin Park is approved.

July/06/2018 of submission

signature

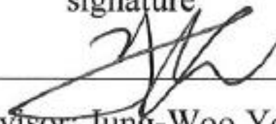

Advisor: Jung-Woo Yoo

signature

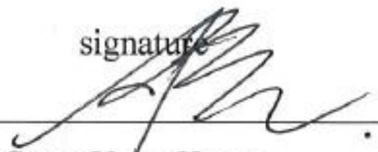

Soon-Yong Kwon

signature

Ki-Suk Lee

signature

Hosub Jin

signature

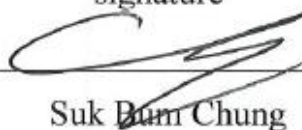

Suk Bum Chung

ULSAN NATIONAL INSTITUTE OF SCIENCE AND TECHNOLOGY

Abstract

Graphene, a single sheet of carbon atoms, is an attractive two-dimensional material due to electronic characters described with massless Dirac equation and has been widely studied in various field, such as semiconductor, photonics, and biotechnology. In particular, graphene has emerged as a leading candidate for electronic and spintronic device application because of the high electron mobility and very weak spin-orbit coupling. For electronics, graphene can replace silicon-based transistor due to high mobility, structural stability, and outstanding thermal conductivity if the band gap of graphene can be engineered. Graphene is also promising spin transporting channel because it has a long spin relaxation length and time. In addition, the disordered graphene with vacancy, adatom, and proximity effect by substrate can have unique electronic characteristics, such as a strong localization, a magnetic ordering, a large spin-orbit coupling, and topological edge state. These properties can lead to unprecedented spin-dependent transport features. Therefore, understanding spin and charge transport properties in disordered graphene is very important for the graphene spinrtonics and electronics.

In this thesis, I studied the spin and charge transport properties in graphene with adatoms and focusing on the spin Hall effect originated from the implanted spin-orbit interaction. In Au-clustered graphene, the dominance of the spin Hall effect which induced nonlocal resistance was observed at the particular carrier concentration. The presence of the spin-Hall induced nonlocal resistance was further confirmed through the Hanle curve and its temperature dependence. The behavior of spin relaxation time obtained from Hanle curves is consistent with the determined spin-orbit coupling symmetry, which is asymmetric near the Dirac point and symmetric at higher concentrations. Based on these results, I suggest that spin-valley relation in Au-decorated graphene can cause the gate-dependent spin current from the spin Hall effect with the enhanced spin-orbit coupling. Also, I researched localization and quantum edge state of disordered graphene prepared with doping with magnetic impurity Fe. The disordered graphene displayed strong localization and quantum spin edge state with splitting of Landau zeroth level. These phenomena could be understood with topological Anderson insulator state.

This thesis is organized as follows:

In chapter I, II and III, I reviewed a basic knowledge for graphene, graphene spintronics and spin Hall effect from the text book and related papers for transport study in doped graphene.

In chapter IV, I described fabrication of the graphene Hall bar device together with graphene growth, wet-transfer, e-beam and photo lithography, and measurement methods.

In chapter V, I discussed gate dependent nonlocal spin Hall resistance in Au-clustered graphene and discussed the behavior of nonlocal resistance and magneto-conductivity in the sample.

Finally, I presented metal insulator transition and quantum Hall edge state based on the gate voltahe dependent resistivity magneto-transport properties, especially at charge neutral point in Al_2O_3 / Fe / graphene system and discussed the results in chapter VI.

ULSAN NATIONAL INSTITUTE OF SCIENCE AND TECHNOLOGY

Contents

List of figures

I. Graphene

1.1 Band structure and electrical properties -- 4
1.2 Spin-orbit coupling ---11
1.3 Weak localization ---13
1.4 Strained graphene ---15

II. Graphene spintronics

2.1 Graphene based spin valve device ---17
2.2 Spin-orbit scattering and spin relaxation mechanism in graphene --------------------------------------20
2.3 Local magnetic moment from point defect ---24
2.4 Proximity effect on ferromagnetic substrate --26

III. Spin Hall effect

3.1 Spin hall effect ---28
3.2 Intrinsic mechanism ---32
3.3 Extrinsic mechanism ---36
3.4 Spin hall effect in graphene ---39

IV. Experimental method

4.1 Material preparation and fabrication --43
4.2 Measurement --45

V. Spin Hall induced nonlocal resistance in Au-clustered graphene

5.1 Introduction ---47
5.2 Experiment methods --49
5.3 Local and non-local electric transport ---50
5.4 Gate-dependent spin Hall effect ---56
5.5 Symmetry spin-orbit scattering --61
5.6 Discussion and summary --63

ULSAN NATIONAL INSTITUTE OF SCIENCE AND TECHNOLOGY

VI. Metal insulator transition and the splitting of zeroth Landau level in Al_2O_3/Fe/graphene system

6.1 Introduction ----------67
6.2 Metal insulator transition ----------68
6.3 The splitting of zeroth Landau level ----------73
6.4 Discussion and summary ----------75

VII. Conclusion

Reference

- Appendix -

The list of achievements----------87

Acknowledgement----------89

ULSAN NATIONAL INSTITUTE OF SCIENCE AND TECHNOLOGY

List of figures

Figure 1. Graphene band structure.

Figure 2. Transmission probability of Klein paradox in graphene.

Figure 3. Ambipolar electric field effect in graphene.

Figure 4. Integer quantum Hall effect in graphene.

Figure 5. Simple band structure of graphene with SOC.

Figure 6. The signature of weak and weak-anti localization.

Figure 7. The localization of graphene.

Figure 8. The band structure of graphene at k, k' in the presence of magnetic field and ununiform strain.

Figure 9. Schematic representation of four terminal nonlocal spin valve device

Figure 10. Spin transport of graphene in a four-terminal spin valve device.

Figure 11. CVD graphene spin valve device for pure spin transport.

Figure 12. Spin relaxation time in single and bi-layer graphene

Figure 13. Weak localization in graphene due to spin-orbit scattering.

Figure 14. Weak and weak antilocalization of graphene heterostructure.

Figure 15. Paramagnetism in graphite due to fluorine adatoms and vacancy.

Figure 16. The effect of hydrogen exposure on spin transport in graphene from spin valve measurement.

Figure 17. The anomalous Hall effect in graphene/YIG heterostructure.

Figure 18. Zeeman spin Hall effect in graphene/EuS heterostructures.

Figure 19. The proximity effect in graphene coupled to a $BiFeO_3$ nanoplate.

Figure 20. From the Hall effect to spin Hall effect.

Figure 21. The spin Hall effect in unstrained GaAs.

Figure 22. Electronic measurement of spin Hall effect in Al.

Figure 23. Extrinsic mechanism of spin Hall effect.

ULSAN NATIONAL INSTITUTE OF
SCIENCE AND TECHNOLOGY

Figure 24. Induced spin-orbit coupling in graphene due to impurity.

Figure 25. The spin Hall effect in hydrogenated graphene.

Figure 26. The spin Hall effect in CVD graphene.

Figure 27. No spin Hall effect in hydrogenated and adatom-decorated graphene.

Figure 28. The process of graphene wet transfer.

Figure 29. The preparation of the substrate with large electrode before graphene transfer.

Figure 30. The optical microscopy image of fabrication process and a device design with CAD software.

Figure 31. Schematic of the graphene H-bar geometry with 6-terminals for spin and charge transport.

Figure 32. The measurement setup for charge and spin transport.

Figure 33. Field effect property and quantum Hall effect in graphene H-bar device.

Figure 34. The enhancement of SOC in Au-clustered graphene.

Figure 35. Nonlocal device geometry and R_{NL} measured for the device A.

Figure 36. the Raman spectra and XPS result of Au-clustered graphene.

Figure 37. SEM image of Au-clustered graphene.

Figure 38. Characteristic nonlocal voltage induced by the thermoelectric effect.

Figure 39. The local and nonlocal resistance of the Au-clustered graphene device B at various temperatures.

Figure 40. Gate voltage dependence of R_{NL} *vs.* $B_{//}$ curves measured for the device B.

Figure 41. R_{NL} as a function of in-plane magnetic field measured at various gate voltage and at T = 3K.

Figure 42. Temperature dependence of $R_{NL}(B_{//})$ and p measured for the device B

Figure 43. R_{NL} as a function of in-plane magnetic field measured at various temperatures.

Figure 44. Gate voltage dependence of MC and the symmetry of the SOS rate.

Figure 45. Spin dynamics in adatom-decorated graphene.

Figure 46. Spin Hall angle of Adatom-decorated graphene.

Figure 47. The local (blue line) and nonlocal (red line) resistance of 4-terminal graphene geometry

ULSAN NATIONAL INSTITUTE OF
SCIENCE AND TECHNOLOGY

Figure 48. Hall bar geometry and charge transport for the Al_2O_3/Fe/graphene device.

Figure 49. Metal insulator transition in various gate voltage for the Al_2O_3/Fe/graphene device.

Figure 50. Magnetoresistance in a perpendicular magnetic field.

Figure 51. Transport properties of Al_2O_3/graphene device.

Figure 52. Quantum Hall effect of Al_2O_3/Fe/graphene device.

Figure 53. The splitting of zeroth Landau level in Al_2O_3/Fe/graphene device

ULSAN NATIONAL INSTITUTE OF SCIENCE AND TECHNOLOGY

I. Graphene

Graphene, which is one of major two-dimensional materials, is a single layer of carbon atoms bound in a hexagonal lattice structure. The band structure of graphene was first predicted with tight binding approximation by P.R. Wallace at 1947[1], and he showed the unusual semimetal behavior with linear energy-momentum dispersion. For a long time, scientist have considered the existence of two-dimensional material to be impossible because of quantum fluctuation. However, a group led by A. K. Geim from the University of Manchester successfully isolated graphene in 2004[2]. Since then, the graphene has been extensively studied in a wide range of scientific communities and technological applications. Unlike normal semiconductor, the low-energy fermionic excitations of graphene revealed to behave as massless Dirac particle[3-4]. For a contribution to graphene science, the 2010 Nobel Prize in Physics was awarded to A. K Geim and K. Novoselove.

In this chapter, I will shortly review the band structure, typical electron transport, spin-orbit coupling, and weak localization of graphene from textbook and papers. I will also briefly summarize how band structure of graphene change in the presence of an ununiform strain.

1.1 Band structure and electrical properties.

As shown in figure 1(a,b), graphene is made up of carbon atoms arranged in honeycomb structure and contains a triangular lattice with a basis of two atoms (A, B) per unit cell. The lattice vectors can be written as

$$\mathrm{a}_1 = \frac{a}{2}\left(3, \sqrt{3}\right), \qquad \mathrm{a}_2 = \frac{a}{2}\left(3, -\sqrt{3}\right) \tag{1}$$

where a ~0.142 nm is the carbon-carbon distance, and graphene lattice constant is about 0.246 nm. The reciprocal-lattice vectors are given by

$$\mathrm{b}_1 = \frac{2\pi}{3a}\left(1, \sqrt{3}\right), \qquad \mathrm{b}_2 = \frac{2\pi}{3a}\left(1, -\sqrt{3}\right). \tag{2}$$

In the first Brillouin zone, there is the two points K and K' at the corners. Their position in momentum space are given by

$$K = \left(\frac{2\pi}{3a}, \frac{2\pi}{3\sqrt{3}a}\right) \qquad K' = \left(\frac{2\pi}{3a}, -\frac{2\pi}{3\sqrt{3}a}\right) \tag{3}$$

and the three nearest-neighbor vectors in real space are given by

$$\delta_1 = \frac{a}{2}\left(1, \sqrt{3}\right), \quad \delta_2 = \frac{a}{2}\left(1, -\sqrt{3}\right), \;\; \delta_3 = a(1,0) \tag{4}$$

The conduction and valence bands consisting of π states touch at the two points as shown in figure 1 (c), where the Fermi level is located, and electronic properties are determined by the state near the *K* and *K*' point. So, these points called Dirac points are important for physics of graphene.

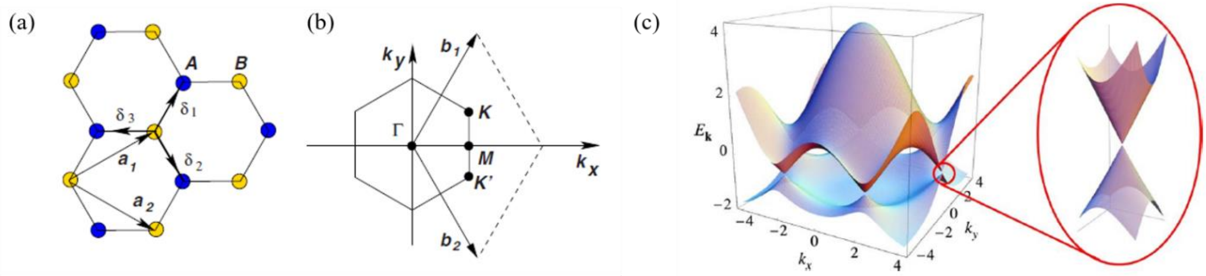

Figure 1. Graphene band structure. (a) the lattice structure of graphene. The lattice unit vectors are denoted by a_1 and a_2. The nearest-neighbor vectors are δi, i = 1, 2, 3. (b) the first Brillouin zone. The Dirac cones are located at the *K* and *K*' points. b_1 and b_2 are reciprocal lattice vectors. (c) electronic dispersion in the graphene honeycomb lattice. Since the π band is half-filled in graphene, Fermi energy goes through the band touching point, which is called Dirac point [3].

The tight-binding Hamiltonian for electrons in graphene considering that electrons can hop to both nearest- and next-nearest-neighbor atoms has the form

$$H = -t \sum_{<i,j>,\sigma} \left(a_{\sigma,i}^{+} b_{\sigma,j} + H.c \right) - t' \sum_{\ll i,j >>,\sigma} \left(a_{\sigma,i}^{+} a_{\sigma,j} + b_{\sigma,i}^{+} b_{\sigma,j} + H.c \right) \tag{5}$$

where $a_{\sigma,i}(a_{\sigma,i}^{+})$ annihilates (creates) an electron with spin σ on site R_i on sublattice, *t* and *t*' are the nearest- and next-nearest-neighbor hopping energy, respectively. The energy bands derived from this Hamiltonian have the form

$$E_{\pm}(\mathbf{k}) = \pm t \sqrt{3 + 2\cos\left(\sqrt{3}k_y a\right) + 4\cos\left(\frac{\sqrt{3}}{2}k_y a\right)\cos\left(\frac{3}{2}k_y a\right)} - t'2\cos\left(\sqrt{3}k_y a\right) + 4\cos\left(\frac{\sqrt{3}}{2}k_y a\right)\cos\left(\frac{3}{2}k_y a\right) \tag{6}$$

where the plus sign applies to the upper (π*) and the minus sign is the lower band (π). The full band structure of graphene is shown in figure 1 (c). For the electronic dispersion close to Dirac point, the two-component electron wave function $\psi(\mathbf{r})$ obeys the 2D Dirac equation [3-5],

$$-\mathrm{i}v_F \boldsymbol{\sigma} \cdot \nabla \psi(\mathbf{r}) = E\psi(\mathbf{r}) \tag{7}$$

ULSAN NATIONAL INSTITUTE OF SCIENCE AND TECHNOLOGY

where $v_F \sim 10^6$ m/s is Fermi velocity and given by $v_F = 3ta/2$.

The equation (7) means that the low-energy fermionic excitations of graphene behave as massless Dirac particle. The wave functions at K and K' are related by time-reversal symmetry. Because of its unique band structure, graphene exhibits unusual electronic behavior and novel transport effects, such as helicity (or chirality)[3], Klein paradox[6-8], FET (Field effect transistor)[2, 9-10], and QHE (quantum hall effect)[4, 11]. Now, I will briefly describe the properties.

Helicity is defined as the projection of the momentum operator along the pseudospin direction. The quantum-mechanical operator for the helicity can be written as $\hat{h} = (1/2) \cdot \boldsymbol{\sigma} \cdot \boldsymbol{p}/|\boldsymbol{p}|$. The wave functions of equation (7) are also eigenstates of $\hat{h}$. Namely, $\boldsymbol{\sigma}$ has its two eigenvalues either in the direction or against the momentum $\boldsymbol{p}$. This property says that the states of the system close to the Dirac point have well defined chirality or helicity and indicates the existence of pseudospin quantum number for the charge carriers. Therefore, the helicity values are good quantum number of graphene system.

The Klein paradox is the perfect tunneling of relativistic Dirac fermions through arbitrary high and wide barriers. In stark contrast to the conventional quantum tunneling where transmission probability exponentially decays with increasing barrier potential, transmission probability of Klein paradox increases with increasing barrier height when the particles are governed by Dirac equation. In the case of graphene, the chirality leads to a varying transmission probability depending on the angle of incidence to the barrier with simplified equation (8) as shown in figure 2.

$$T(\emptyset) \cong \frac{\cos^2\emptyset}{1-\cos^2(Dq_x)\sin^2\emptyset} \tag{8}$$

where D is wide barriers and q_x is refraction angle.

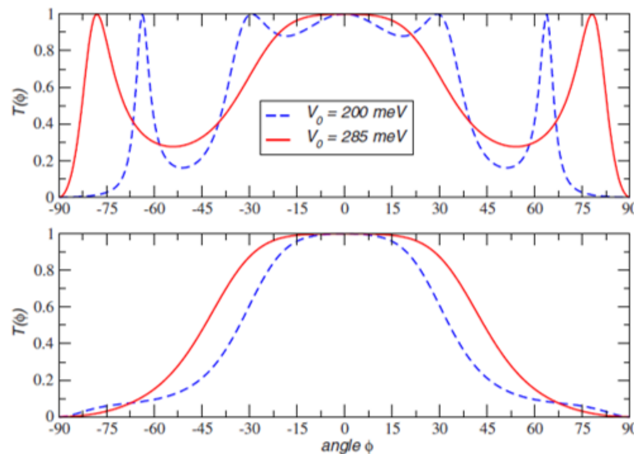

Figure 2. Transmission probability of Klein paradox in graphene. Angular behavior of $\boldsymbol{T}(\emptyset)$ for two different barrier potential values, the parameters are $D = 110$ nm (top), $D = 50$ nm (bottom) $E = 80$ meV, $k_f = 2\pi/\lambda$, and $\lambda = 50$ nm.[3]

ULSAN NATIONAL INSTITUTE OF SCIENCE AND TECHNOLOGY

Meanwhile, the symbolic characteristics of charge transport in graphene are ambipolar field effect and unusual quantum Hall effect (QHE). The transport properties of graphene are typically investigated through graphene Hall bar device as shown in figure 3 (a). For this device[12], graphene is commonly deposited on SiO_2 wafer. Other substrates are used for specific purposes, such as h-BN to obtain pristine graphene, magnetic insulator to induce proximity effect, etc. The figure 3 (b) shows that changing the electric potential of the Si as a back gate can control the carrier density and type. This carrier density shifts accordingly the Fermi level position in the graphene band structure. The charge-neutrality point (CNP) is located at the transition between the electron and hole regime, where the resistivity is maximized. In perfect graphene crystal, the Dirac points are coincident with overall CNP. Experimentally, resistivity (ρ) is measured using a standard 4-probe technique as shown in the figure 3(a), and is given by $\rho = (W/L)(V_{34}/I_{12})$ where W and L are the width and the length of graphene, respectively. V_{34} is the voltage across electrode 3 and 4. I_{12} is current between 1 and 2. Then, from the Drude model, the conductivity σ is given by $\sigma = ne\mu$, where n is the carrier density, e is the electron charge, and μ is the carrier mobility. The net carrier density n approaches the gate-induced (V_g) carrier density, $n = (c_g/e)(V_g - V_d)$, where c_g is gate capacitance and V_d is the gate voltage corresponding to CNP. Therefore, the field-effect mobility is given by

$$\mu_{FE} = \frac{1}{e}\frac{d\sigma}{dn} = \frac{1}{e}\frac{d\sigma}{d(\alpha|V_g - V_d|)} \tag{9}$$

In the case of Si substrate with 300 nm SiO_2 layer, α (c_g/e) is about 7.2×10^{14} /m^2V. Typically, mobility of graphene on SiO_2 ranges from 2000 to 10000 cm^2/Vs at room temperature.

The electron mean free path l can be derived from the conductivity as follows, the Einstein relation is

$$\sigma = e^2 D(\varepsilon_F) D_d \tag{10}$$

where $D(\varepsilon_F)$ is the density of states at the Fermi level ε_F and D_d is the diffusion constant for d-dimensional system. For two-dimensional system (d = 2)

$$D_2 = \frac{1}{2}v_F^2\tau = \frac{1}{2}v_F l \tag{11}$$

Here, $\tau = l/v_F$ is the mean scattering time. For monolayer graphene, the Fermi energy is

$$\varepsilon_F = \hbar v_F k_F \tag{12}$$

ULSAN NATIONAL INSTITUTE OF SCIENCE AND TECHNOLOGY

where k_F is the Fermi wavenumber. The carrier density n is given by

$$n = g_s g_v \frac{\pi k_F^2}{(2\pi)^2} = \frac{k_F^2}{\pi} = \frac{\varepsilon_F^2}{\pi(\hbar v_F)^2} \tag{13}$$

where $g_s = 2, g_v = 2$ are the spin and valley degeneracies, respectively. The graphene's density of states becomes

$$D(\varepsilon_F) = \frac{dn}{d\varepsilon} = \frac{2\varepsilon_F}{\pi(\hbar v_F)^2} = \frac{4\varepsilon_F}{h v_F} = \frac{2}{\hbar v_F}\sqrt{\frac{n}{\pi}} \tag{14}$$

Substitution of the expression for D_2 and $D(\varepsilon_F)$ into the Einstein relation gives

$$\sigma = \frac{2e^2}{h} k_F l \tag{15}$$

Thus, the mean free path is given by

$$l = \frac{h}{2e^2}\frac{\sigma}{\sqrt{n\pi}} \tag{16}$$

In gneral, the mean free path of graphene on SiO_2 substrate far from the CNP is around 100 nm.

When a strong perpendicular magnetic field is applied to conventional two-dimensional electron system, the Hall conductivity have quantized values. This property is caused by the cyclotron motion of electrons, which results in a Landau quantization of the energy levels.

In the case of graphene system, the equation (7) with magnetic field is given by

$$\pm v_F(\boldsymbol{P} + \boldsymbol{eA}) \cdot \boldsymbol{\sigma}\psi(\mathbf{r}) = E\psi(\mathbf{r}) \tag{17}$$

where $\boldsymbol{P} = -i\hbar\nabla$, **A** is the magnetic vector potential, and $\psi(\mathbf{r})$ is two-component vector. Here the Landau gauge **A**: $\mathbf{A} = -By\hat{x}$ is used for a constant magnetic field **B** perpendicular to the x-y plane. Then, taking only the + sign in (17), this equation relates two-component vector:

$$v_F(P_x - iP_y - eBy)\psi_2(\mathbf{r}) = E\psi_1(\mathbf{r}) \text{ and } v_F(P_x - iP_y - eBy)\psi_1(\mathbf{r}) = E\psi_2(\mathbf{r}) \tag{18}$$

Substituting the first to the second equations above, we obtain the equation for $\psi_2(\mathbf{r})$ only

$$v_F^2(P^2 - 2eByP_x + e^2B^2y^2 - \hbar eB)\psi_2(\mathbf{r}) = E^2\psi_2(\mathbf{r}) \tag{19}$$

ULSAN NATIONAL INSTITUTE OF
SCIENCE AND TECHNOLOGY

The eigenenergies of (19) can be found by comparing this equation with a massive carrier Landau system: $E_n^2 = 2n\hbar eBv_F^2$ where n = 1,2,3, … the constant $-\hbar eB$ shifts the Landau level's by half of the equal spacing between the adjacent Landau levels, and it also guarantees that there is a Landau level at E = 0, which has the same degeneracy as the other Landau levels. Putting these expressions together, the eigenenergy for a general Landau level can be written as [13-14]

$$E_n = \mathrm{sgn}(n)\sqrt{2|n|\hbar eBv_F^2} \tag{20}$$

where $n > 0$ corresponds to electron-like Landau levels and $n < 0$ corresponds to hole-like Landau levels. There is a single Landau levels sitting exactly at $E = 0$, corresponding to $n = 0$, because of the chiral symmetry and the particle-hole symmetry as shown in figure 4 (a)[15]. The square root dependence of the Landau level energy on n can be understood if we consider the density of state for the relativistic electron[15-16].

In the magnetic field, the Hall conductivity σ_{xy} of graphene can be determined by counting the number of occupied levels above the charge neutral point, and is given by

$$\sigma_{xy} = \frac{4e^2}{h}\left(n + \frac{1}{2}\right) \tag{21}$$

The factor 1/2 in equation (21) appears because the 0-th Landau level is half-filled when the system is charge neutral. And the constant 4 means for 2 by the spin degeneracy and 2 by valley degeneracy under a magnetic field[3-4, 17].

The figure 4 (b) shows that the observed QHE in graphene is distinctively different from the conventional QHEs due to the additional half-integer[4, 15]. This unusual quantization condition is a result of the topologically exceptional electronic structure of graphene. The sequence of half-integer multiples of quantum hall plateaus has been predicted by several theories which combine relativistic Landau levels with the particle-hole symmetry of graphene[3, 10, 15, 17].

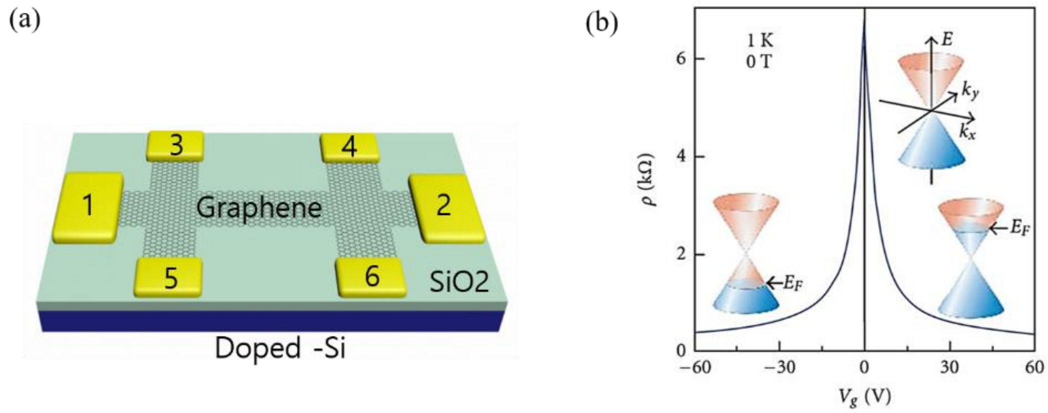

Figure 3. Ambipolar electric field effect in graphene. (a) Schematic representation of common graphene Hall bar device. (b) gate dependent field effect transistor property of graphene. The inserts of (b) show the changes in the position of Fermi level in response to the applied gate voltage.[10]

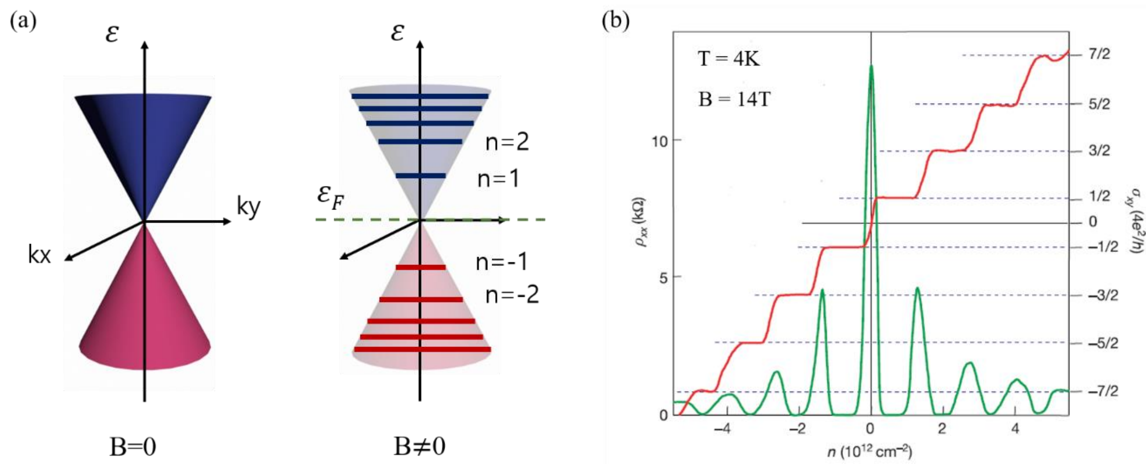

Figure 4. Integer quantum Hall effect in graphene. (a) schematic representation of the formation of Landau level in graphene with strong magnetic field.[15] (b) The hallmark of massless Dirac fermions is QHE plateau. Hall conductivity σ_{xy} and longitudinal resistivity ρ_{xx} of graphene as a function of their concentration at B = 14 T and T = 4 K.[4]

ULSAN NATIONAL INSTITUTE OF SCIENCE AND TECHNOLOGY

1.2 Spin-orbit coupling of graphene.

In orbital motion around nucleus, the electron in an atom feels the electric field because of positively charged nucleus. As a result, a magnetic field appears in the rest frame of the electron through a Lorentz transformation. According to Einstein's relativity theory, the magnetic flux density associated with this magnetic field is

$$\mathbf{B} = \frac{\boldsymbol{v}\times\boldsymbol{E}}{2c^2\sqrt{1-v^2/c^2}} \tag{22}$$

where $\boldsymbol{E}$ is the electric field seen by the electron, $\boldsymbol{v}$ is its orbital velocity and c is the speed of light in vacuum[18-19].

For a non-relativistic electron, we can consider that the electron is sitting at the center of a circulating charged nucleus as current loop. The current in this loop is given by $\boldsymbol{I} = -Ze\boldsymbol{v}$. Where the nucleus has charge Ze and is moving with velocity $\boldsymbol{v}$ relative to the electron. Coulomb's electrostatic law can be used to give the electric field felt by the electron due to the nucleus, $\boldsymbol{E} = (Ze/4\pi\varepsilon_0\boldsymbol{r}^3)\boldsymbol{r}$. From Biot-Savart law, the magnetic field due to this current is given by $\mathbf{B} = (\mu_0/4\pi\, r^3)(\boldsymbol{I}\times\boldsymbol{r})$. And then, the magnetic field that electron feels by circulating charged nucleus can be rewritten as

$$\mathbf{B} = -\mu_0\epsilon_0\boldsymbol{v}\times\boldsymbol{E} = -\frac{\mathbf{1}}{\mathbf{c^2}}\boldsymbol{v}\times\boldsymbol{E} \tag{23}$$

where we have used the relationship $\mu_0\varepsilon_0 = 1/c^2$.

Because the electron has a spin magnetic momentum, there will be a potential energy associated with this magnetic field. Then, we can introduce the Hamiltonian H in term of the spin angular momentum operator.

$$\widehat{H} = -\frac{e}{2m}\hat{\mathbf{S}}\cdot\mathbf{B} = -\frac{e}{2mc^2}\hat{\mathbf{S}}\cdot\boldsymbol{v}\times\boldsymbol{E} \tag{24}$$

The force felt by electron due to the electric field is $\mathbf{F} = -(\mathrm{d}V(\mathrm{r})/\mathrm{d}r)\hat{\mathbf{r}}$. Therefore, equation (24) can be rewritten as

$$\widehat{H} = -\frac{1}{2mc^2}\hat{\mathbf{S}}\cdot\boldsymbol{v}\times\mathbf{F} = -\frac{1}{2mc^2}\frac{1}{r}\frac{dV(r)}{dr}\hat{\mathbf{S}}\cdot\boldsymbol{v}\times\mathbf{r} \tag{25}$$

Now, we can substitute $L = \mathrm{m}v\times r$. and we replace the classical angular momentum vector with quantum mechanical angular momentum operator. Finally, we have

$$\hat{H} = -\frac{1}{2mc^2}\frac{1}{r}\frac{dV(r)}{dr}\hat{\mathbf{S}} \cdot \hat{\mathbf{L}}. \quad (26)$$

This is the well-known expression for spin-orbit coupling (SOC) in atomic scale[20].

In atomic scale, spin-orbit coupling enhances with increasing atomic number. So, spin-orbit coupling of graphene consisted of carbon atoms is predicted to be weak because carbon is light element with relatively weak spin-orbit coupling.

However, in graphene, the spin-orbit coupling depends strongly on the bands. At K point, earlier tight-binding studies based on *s* and *p* orbital predicted the spin-orbit-induced gap of graphene as small as 1 μeV[21]. All-electron first-principle calculation give the value of the gap in the range between 25 and 50 μeV[22-23]. This gap originates from the spin-orbit coupling of *d* and higher orbital. The energy spectrum of Dirac electrons in graphene in the presence of spin-orbit coupling was first introduced by McClure and Yafet[24]. The Hamiltonian in modern notation reads $H = \lambda_I \kappa \boldsymbol{\sigma}_z \mathbf{s}_z$, where λ_I is the intrinsic SOC parameter, κ is 1 and -1, $\boldsymbol{\sigma}_z$ is the Pauli matrix of sublattice space A and B, and $\mathbf{s}_z$ is the spin Pauli matrix. As shown in figure 5, this intrinsic spin-orbit coupling opens a gap in the Dirac spectrum with magnitude = 2 λ_I[24].

Meanwhile, Kane and Mele predicted[25-26] the quantum spin hall effect in graphene with intrinsic spin-orbit coupling. Unfortunately, the weak spin-orbit coupling makes its direct experimental observation hard.

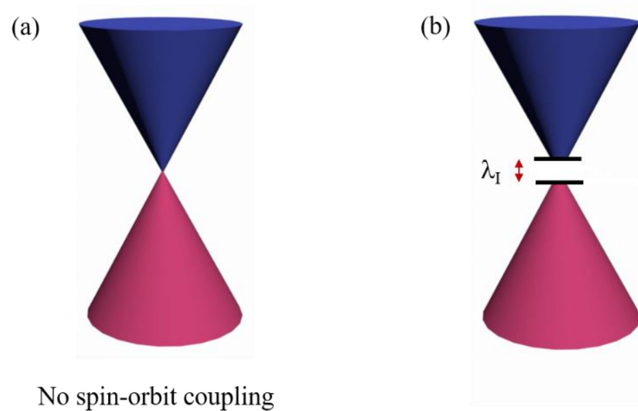

Figure 5. Simple band structure of graphene with SOC. (a) Touching Dirac cones exist only when SOC is negligible. (b) With the presence of SOC, the orbital degeneracy at the Dirac point is lifted and the gap appears[24].

1.3 Weak localization and weak anti-localization.

In diffusive regime, we can consider electron transport of two type as shown in figure 6. One is the semiclassical diffusion (figure 6 (a)) given by Drude conductivity. This diffusion occurs when the phase coherence length (l_θ) by inelastic scattering is less than mean free path (l). The other one is the quantum diffusive regime that appears as $l_\theta >> l$. In this regime, the quantum interference between time-reversed scattering loops give rise to a correction to the conductivity. If there is constructive interference of electron along time reversal path, weak localization appears. If there is destructive interference, weak anti-localization occurs[27-28].

Quantum interference in graphene is different from conventional two-dimensional system due to chirality of pseudospin having Berry phase of π. This Berry phase of π inverts the constructive interference to destructive interference. Then, the quantum interference of graphene can expect weak anti-localization and a positive magnetoresistance. However, the trigonal warping in valley suppresses antilocalization, and intervalley scattering of graphene tends to restore WL. When the intervalley time shorter than the decoherence time(τ_φ), the quantum correction to the conductivity has WL behavior. The corresponding magnetoresistance can be expressed as[29]

$$\Delta\rho(B) = -\frac{e^2\rho^2}{\pi h}\left[F\left(\frac{B}{B_\varphi}\right) - F\left(\frac{B}{B_\varphi+2B_i}\right) - 2F\left(\frac{B}{B_\varphi+B_t}\right)\right] \qquad (27)$$

$$F(\mathrm{z}) = \ln z + \psi\left(\frac{1}{2}+\frac{1}{z}\right) \qquad B_{\varphi,i,t} = \frac{\hbar c}{4De}\tau_{\varphi,i,t}^{-1} \qquad \tau_t^{-1} = \tau_i^{-1} + \tau_*^{-1} + \tau_w^{-1}$$

where ψ is digamma function, D is the diffusion coefficient, τ_i^{-1} is intervalley scattering rate, $\tau_*^{-1}$is intravalley scattering rate, and τ_w^{-1} is trigonal warping relaxation rate.

In graphene/SiO_2 device, it was experimentally demonstrated that both WL and WAL could be observed in graphene under the proper conditions as shown in figure 7 [30]. The increasing temperature reduce decoherence time of the electron because of thermal fluctuations, And the decreasing carrier density increases the intervalley and intravalley elastic scattering times. Thus, it is observed that the decoherence time is not the only parameter controlling WL behavior in graphene. Therefore, the ratios τ_φ/τ_i and τ_φ/τ_* should be considered for localization behavior as shown in figure 7 (b). According to this study[30], the favorable condition for the observation of WAL are small ratios.

In graphene, the quantum correction to the conductance survive at much higher temperature than for two-dimensional electron gas semiconductor structure because the electron-phonon scattering is expected to be weak in the system[3, 17, 30-31].

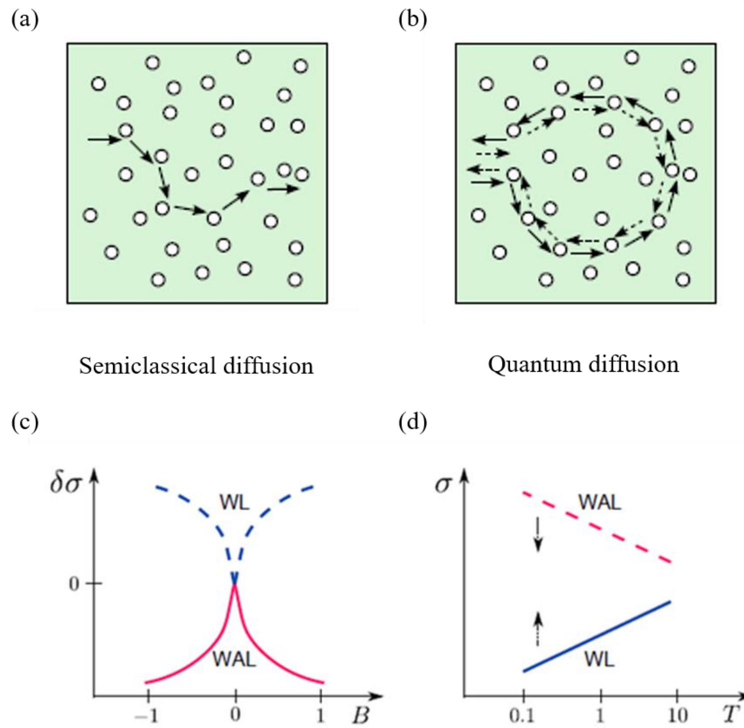

Figure 6. The signature of weak and weak-anti localization. (a), (b) schematic illustration of different electron transport in materials. (c) the magnetoconductivity for weak localization and weak-anti localization. (d) temperature dependent of the magnetoconductivity. B is magnetic field and T is temperature[27-28].

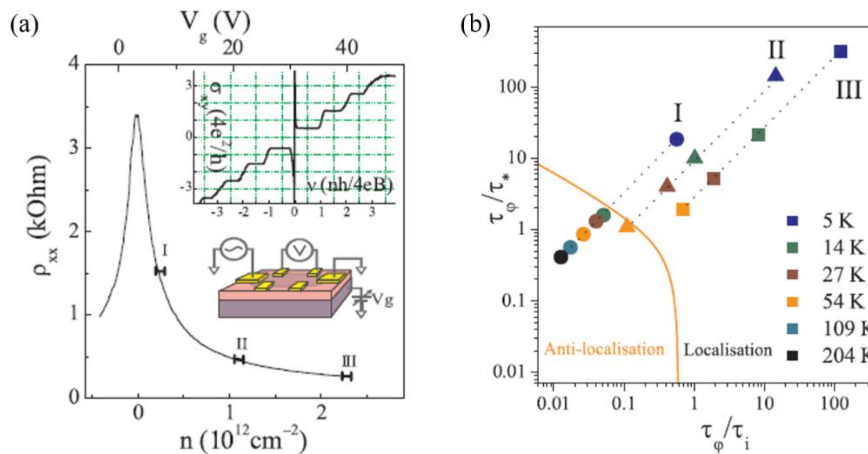

Figure 7. The localization of graphene. (a) Resistivity as a function of the carrier density in graphene hall bar device. The magnetoconductance is studied at three different regions. Inset: the results of quantum hall effect measurement. (b) A diagram of the scattering times related to quantum interference in graphene. The solid curve separates the regions of the anti-localization and localization. Points are experimental values found from the fitting of the magnetoconductivity using equation (27) at three different regions[30].

1.4 Strained graphene.

In nowadays nanotechnology, understanding the effect of strain, especially at reduced dimension is important to improve performance of device. The random strain in material lead to a modification of the hopping energy and can be modeled by a fictitious gauge field which can then act as an effective magnetic field[3, 17]. In graphene, it was predicted[32] that this effective magnetic field can have an intensity as high as 10T in some condition, and suggested to a pseudomagnetic quantum Hall effect. Experimentally, the presence of strain-induced pseudomagnetic field greater than 300T was observed using scanning tunneling microscopy[33]. Also, the coexistence of the pseudomagnetic fields and external magnetic field can split valley-polarized Landau level in the quantum Hall regime[34]. Therefore, the strain in graphene can give rise to a rich structure in the electronic and transport properties of the material[35].

Recently, it was theoretically reported[36] that the coexistence of pseudo and real magnetic field can induce a gap difference between two valley points (K and K') in honeycomb lattice of graphene system as shown figure 8. The gap difference between two valleys can be obtained within the perturbation theory. The figure 8 (b) shows that this valley gap difference depends on both magnetic field and applied strain in strained graphene. Valley gap difference defined as $\Delta E_{VGD} = E_K^{gap} - E_{K\prime}^{gap}$(figure 8 (b)) can be written as

$$\Delta E_{VGD} = \frac{ev_f BL^2}{2} \sum_\eta \left(\mathcal{M}_{+\eta} - \mathcal{M}_{-\eta}\right) \neq 0 \tag{28}$$

where $\mathcal{M}_{+\eta} = C_{+\eta} + C_{+\eta}^*$, $\mathcal{M}_{-\eta} = C_{-\eta} + C_{-\eta}^*$ and $C_\eta = \alpha_\eta \beta_\eta^*$. The B is external magnetic field and L stands for the size of the system. The α and β are the components of the unperturbed Dirac Hamiltonian eigenvector.

A valley Hall current can be generated by the population imbalance because of the valley gap difference and expressed in terms of Berry curvature.

$$\sigma_{xy} = \sum_\eta \frac{e^2}{2\pi h} \iint dk_x dk_y \Omega_{k_x k_y}^\eta \tag{29}$$

where η is valley index for $K(K')$. The Berry curvature $\Omega_{k_x k_y}^\eta$ of strained graphene in presence of magnetic field is,

$$\Omega_{k_x k_y}^\eta = \frac{\eta m v_f^2}{\left(v_f^2 \pi_x^2 + v_f^2 \pi_y^2 + m^2\right)^{\frac{3}{2}}} \tag{30}$$

ULSAN NATIONAL INSTITUTE OF
SCIENCE AND TECHNOLOGY

where $\pi_x = k_x + eA_{m_x} + \eta A_{s_x}$, $\pi_y = k_y + eA_{m_y} + \eta A_{s_y}$, A_m is the real magnetic field, and A_s is the gauge field from the strain. Berry curvature depends on magnetic and pseudomagnetic field as shown in figure 8(c-e). In the absence of the strain (figure 8 (c,d)), Berry curvature of different Dirac point are opposite. So, the total valley hall conductivity vanishes exactly. However, the presence of magnetic field in strained graphene induces a gap difference between two valley point (figure 8 (b)) and leads population imbalance in two inequivalent Dirac point[36].

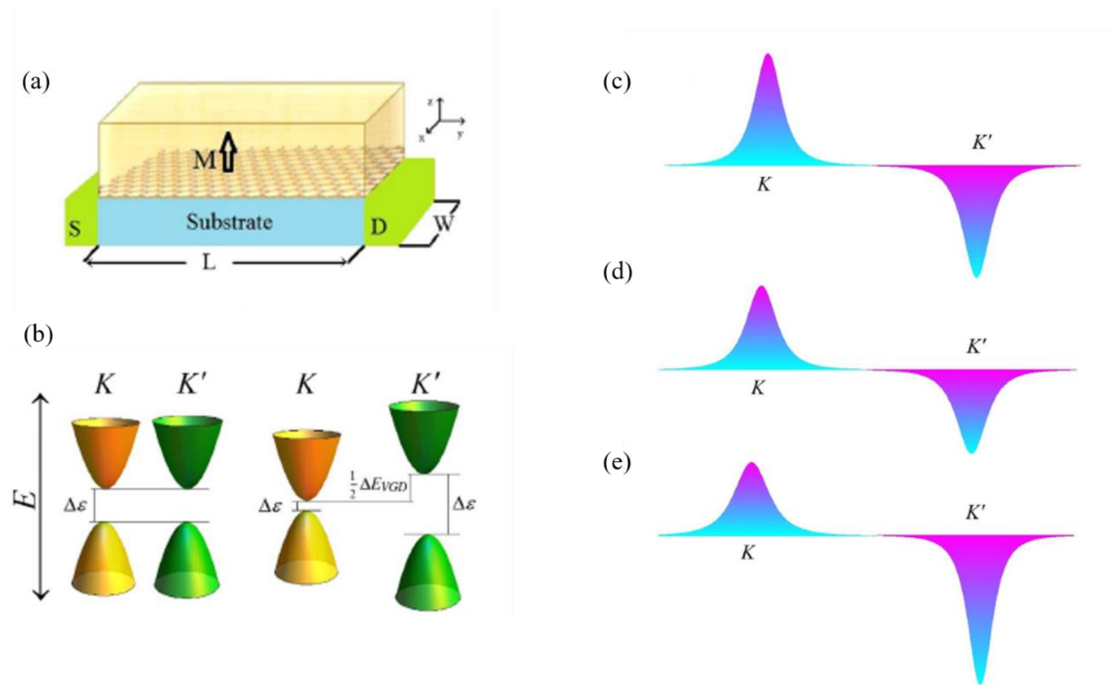

Figure 8. the band structure of graphene at k, k' in the presence of magnetic field and ununiform strain. (a) a schematic proposal for the valley Hall current and valley polarization in graphene. A ferromagnetic metal with z direction of magnetization has been placed on top. The S and D are the source and drain. W and L are the width and length of strained graphene, respectively. (b) in the absence of magnetic field, the strain alone could not generate any gap difference between k and k'. however, applying a magnetic field in strained graphene, a gap difference can be induced between the valleys. (c-e) It is indicated that Berry curvature (c) in the absence of stain and magnetic field, (d) in the presence of magnetic field, (e) in the presence of magnetic field and strain[36].

II Graphene spintronics

Spintronics aim to study the properties of the electron spin with a view to improve the efficiency of electronic devices and to enrich them with new functionalities of information storage and logic device[37]. In spin logic device, the major challenge is to develop suitable spin transport channel with long spin life time and relaxation length for high-speed, low power operation, and spin transistor[38-39].

Graphene is a very promising spin channel material due to the achievement of spin transport with long spin diffusion length of several micrometer at room temperature[40-43]. Moreover, graphene has many interesting properties that also make it very attractive for spintronics, including gate-tunable carrier concentration[44], high electronic mobility[45], and valley degree of freedom[46-47].

In this chapter, I will shortly introduce nonlocal spin valve device, spin-orbit scattering and spin relaxation mechanism for graphene. I will also briefly review the local magnetic moment and proximity effect of graphene based on a recent trend of research

2.1 Nonlocal spin valve device of graphene.

The nonlocal spin valve is widely used for the measurement of spin transport properties in nonmagnetic materials (NM), such as semiconductor, graphene and organic, with ferromagnetic material (FM). This measurement method was first proposed by Aronov [48] and experimentally demonstrated by Johnson and Silsbee[49] in metallic channel. As shown in figure 9[37, 41, 50], a current source is applied between electrode 1 and 2. At this time, electrode 2 acts as spin injector from spin-dependent chemical potential of FM metal. After spin injection, the spins in channel underneath 2 can diffuse in both ways. A spin current along with a charge current flows in the direction of 1, and spin current without a charge current diffuses in the direction of 3. Then, the spin density can be detected by measuring the voltage across 3 and 4. This method is called nonlocal measurement because the voltage probe lies outside the charge current loop. The measured voltage is positive or negative depending on whether the magnetization configurations of 2 and 3 are parallel or antiparallel to each other. To generate the parallel and antiparallel magnetization alignments of 2 and 3, an in-plane magnetic field is applied as shown figure 9. Here, the widths of electrode 2 and 3 are different each other to make difference for coercivity field. Then, the difference of nonlocal resistance between parallel and antiparallel state is nonlocal magnetoresistance(MR) and is a result of the spin diffusion from electrode 2 to 3.

Nonlocal MR in graphene at room temperature was first demonstrated in 2007 by the van Wees group[40]. As shown in figure 10, it is observed that nonlocal spin signals reflecting the magnetization direction of all four electrodes. They also showed that no significant changes in the spin signals occur between 4.2 K, 77K and room temperature. The estimated spin relaxation length in their study was in between

ULSAN NATIONAL INSTITUTE OF SCIENCE AND TECHNOLOGY

1.5 and 2 μm at room temperature. The spin polarization of the injected carrier, which corresponds to the spin injection efficiency, is calculated to be around 10%.

Recently, M. Venkata Kamalakar et al[43]. demonstrates the long-distance (16 μm) spin transport capability of CVD (chemical vapor deposition) graphene at room temperature. The nonlocal measurement with spin precession (Hanle effect) in such long channel give rise to a spin relaxation time of 1.2 ns and spin relaxation length of 6 μm at 300K (figure 11).

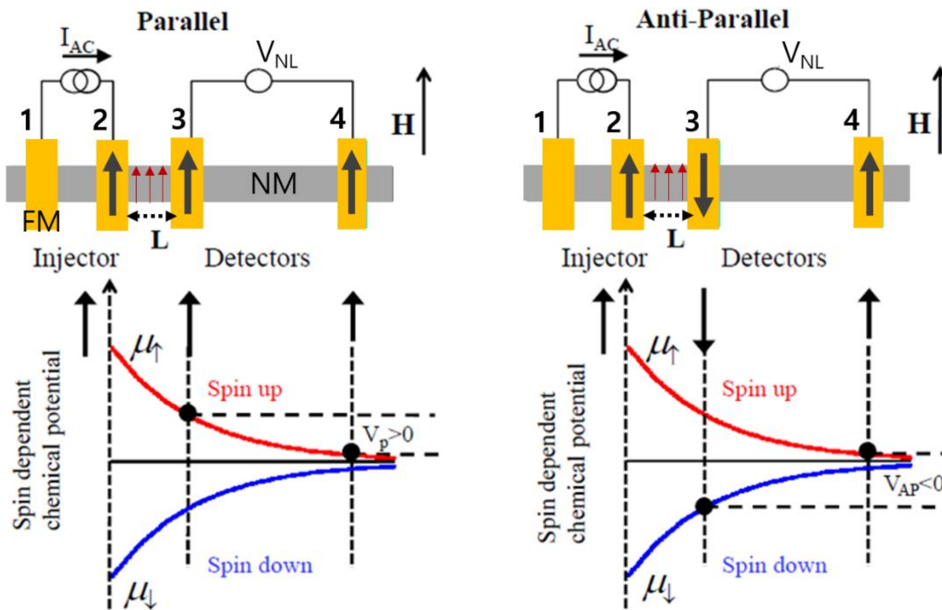

Figure 9. Schematic representation of the four terminal nonlocal spin valve devices with parallel and antiparallel magnetization of the spin injector and detector. With the spin injection at 2, the spins can diffuse in both direction of 1 and 3. This non-local spin diffusion is usually described by spin dependent chemical potential. When the spins diffuse toward 3, the spin density decays because of spin-flip scattering. The measured voltage between 3 and 4 is positive or negative depending on whether the magnetization configuration of 2 and 3 are parallel or antiparallel to each other. This nonlocal magnetoresistance is defined as $\Delta \boldsymbol{R}_{NL} = (\boldsymbol{V}_p - \boldsymbol{V}_{AP})/\boldsymbol{I}$.[41]

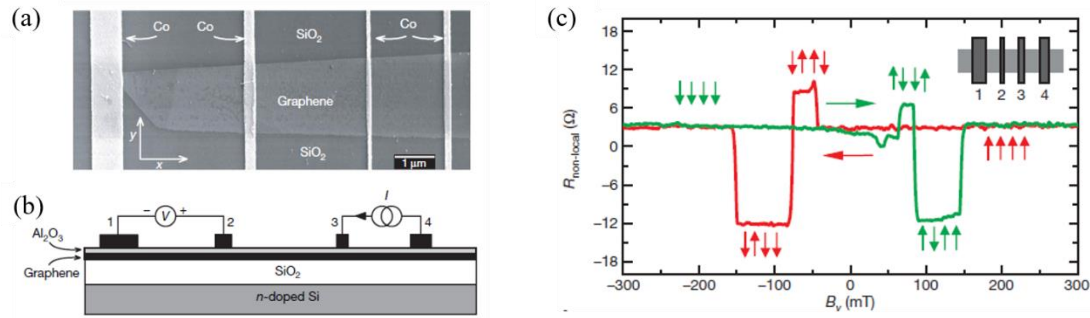

Figure 10. Spin transport of graphene in a four-terminal spin valve device. (a) Scanning electron microscopy image of a four-terminal single-layer graphene spin valve. (b) The non-local spin valve geometry. A current I is injected from electrode 3 through the Al_2O_3 barrier into graphene and is extracted at contact 4. The voltage difference is measured between contacts 2 and 1. (c) Nonlocal spin valve signal of graphene at 4.2K. The sweep directions of the magnetic field are indicated (red or green arrows).[40]

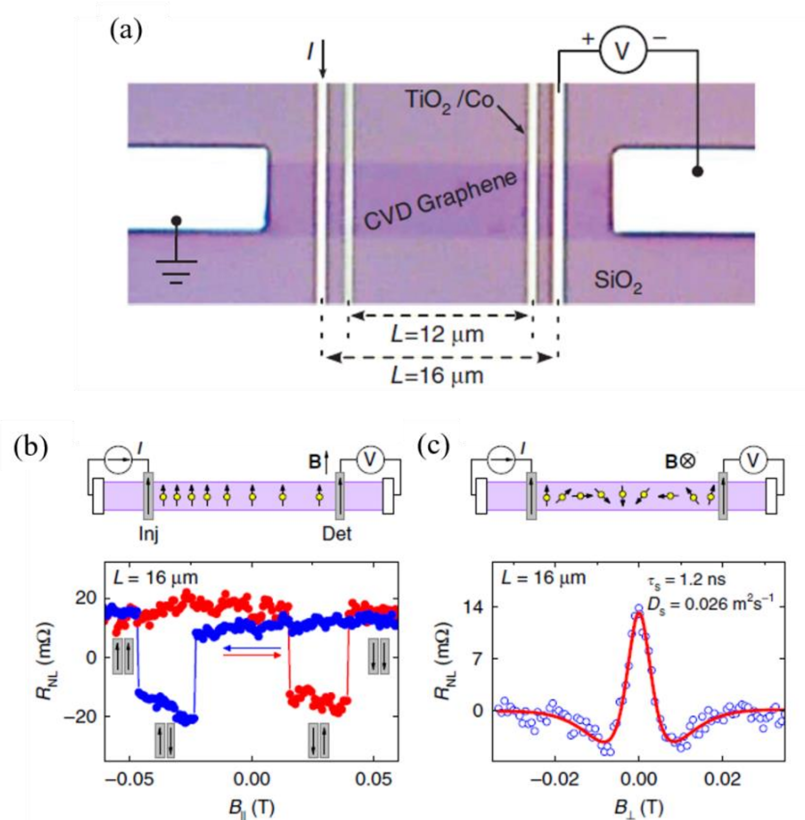

Figure 11. A CVD graphene spin valve device for pure spin transport. (a) Optical microscope image of a fabricated long channel CVD graphene device on SiO_2/Si substrate with multiple ferromagnetic tunnel contacts of Co/TiO_2 patterned by the e-beam lithography. The nonlocal measurement configuration is presented for 16 μm channel with current and voltage circuits. (b) Nonlocal spin valve signal with in-plane magnetic field sweep. The blue and red colors indicate the direction of magnetic field sweep. (c) Nonlocal Hanle spin precession signal obtained by a perpendicular magnetic sweep. τ_s and D_s are spin relaxation time and spin diffusion constant, respectively.[43]

2.2 Spin relaxation mechanism and spin-orbit scattering in graphene.

In graphene, two mechanisms of spin relaxation have been widely applied to explain experimental trends. The two mechanisms are Elliott-Yafet (EY)[51] and Dyakonov-Perel (DP)[52] mechanisms. Both have their roots in metal and semiconductor spintronics[18].

EY mechanism [51]is a result of the fact that Bloch states, which are solution of the Schrodinger equation in the periodic potential, are not spin eigenstates in the presence of spin-orbit coupling. The spin polarization depends slightly on the wavevector of electron. If two spin orientation of electron is slightly different in two wavevector states (k_1 and k_2) in arbitrary band structure, each wavevector has two possible spin orientation that can have arbitrary angle between them. Then, because the up-spin state at k_1 and the down-spin state at k_2 are not strictly orthogonal and anti-parallel, any collision with nonmagnetic scattering that changes the wavevector of an electron from an initial state k_1 to a state k_2 can couple the spins and flip an electron's spin. This spin relaxation is always accompanied by some degree of momentum relaxation because the wavevector must change to change the spin orientation. The approximate expression for EY spin relaxation with temperature T by thermal distribution is[18]

$$\frac{1}{\tau_{EY}} = A\left(\frac{k_b T}{E_g}\right)^2 R^2 \left(\frac{1-R/2}{1-R/3}\right)^2 \frac{1}{\tau_m} \tag{31}$$

where E_g is the band gap, $R = \Delta/(E_g+\Delta)$, Δ is the spin-orbit splitting of valence band, τ_m is the momentum relaxation time, and A is a constant depending on the dominant scattering mechanism for momentum relaxation. This relation shows that EY spin relaxation rate is directly proportional to the momentum relaxation rate. Therefore, EY mechanism is caused by momentum relaxation. Also, this expression shows that the spin and momentum relaxation rates have different temperature dependences. If the momentum relaxation rate is independent of temperature, the spin relaxation rate should increase quadratically with temperature.

DP spin relaxation mechanism[52] is a result of the Dresselhaus and/or Rashba spin-orbit interaction. In an inversion asymmetry solid system, an electron will experience strong spin-orbit interaction. If there is crystallographic inversion asymmetry known as bulk inversion asymmetry, Dresselhaus spin-orbit interaction is given. If there is the structure inversion asymmetry caused by an external or built-in electric field, Rashba spin-oribi interaction exist in there. These interactions lift the degeneracy between up-spin and down-spin states at any non-zero wavevector, so that these two spin states have different energies in the same wavevector state. Therefore, these two interactions truly behave like effective magnetic field because magnetic field also lifts the degeneracy between two spin states at any wavevector with Zeeman interaction. The effective magnetic field causes an electron's spin to undergo Larmor precession. In this effective magnetic field, if electron velocity changes randomly with time

because of scattering, each electron would have processed by different angles because they have different scattering histories. Then, after all electrons is injected with the same spin polarization, their spin polarizations gradually go out of phase with each other. This is the basis of DP spin relaxation. The approximate expression for spin relaxation rate due to DP mechanism is[18]

$$\frac{1}{\tau_{DP}} = Q\left(\frac{4R}{\sqrt{3-R}}\frac{m^*}{m_0}\right)^2 \frac{(k_BT)^3}{\hbar^2 E_g}\tau_m \tag{32}$$

where Q is a dimensionless quantity depending on the dominant momentum relaxation, m_0 is the free electron mass, m^* is the electron effective mass and R was defined in EY mechanism (31). DP mechanism shows that the spin relaxation rate is inversely proportional to the momentum relaxation rate and have a strong temperature dependence.

In graphene, experimental studies have been performed to investigate the spin relaxation mechanism through spin valve device. As shown in figure 12, W. Han and R. K. Kawakami [53] reported different spin relaxation mechanism in single and bi-layer graphene. For single-layer graphene, it was observed that the spin relaxation time increases with increasing momentum relaxation time (proportional relation with diffusion constant) when the carrier concentration is changed by back gate, which suggests that the EY relaxation mechanism is dominant. For bilayer graphene, it was found that spin relaxation time decreases with increasing momentum relaxation time, suggesting a DP spin relaxation mechanism.

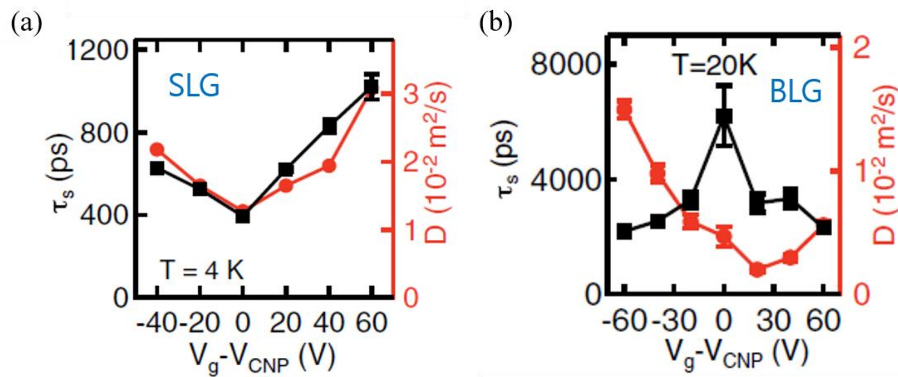

Figure 12. spin relaxation time τ_s and diffusion constant D from nonlocal magnetoresistance of (a) single-layer and (b) bi-layer graphene. In a single-layer graphene, both τ_s and D increases with increasing with carrier concentration. This correlation implies a linear relation between τ_s and τ_m because of $D \sim \tau_m$. This indicates the dominance of the EY spin relaxation mechanism. On the other hand, in bi-layer graphene, the opposite behaviors of τ_s and D is observed upon increasing gate voltage. This suggests that DP spin relaxation mechanism is dominant in bi-layer graphene[53].

Meanwhile, the two types of spin-orbit scattering related to spin relaxation mechanism are suggested in graphene system. The first is intrinsic spin-orbit scattering (SOS) described as Kane and Mele model[25-26]. The second is spin-orbit scattering of Bychkov-Rashba type [18, 54] when inversion symmetry is broken due to substrate or external electric field. These spin-orbit scattering have different spin relaxation mechanism. The spin-orbit scattering of KM type causes spin relaxation through the EY mechanism. However, Bychkov-Rashba spin-orbit scattering produce the DP spin relaxation[29]. E. McCann and V.I. Fal'ko[29] investigated the influence of these spin-orbit scattering on the weak localization effect for electron in graphene and found that a disordered graphene with asymmetric spin-orbit scattering should display a weak antilocalization behavior at low temperature, while symmetric spin-orbit scattering of KM type lead to weak localization effect. Namely, weak localization and weak antilocalization in the graphene can be determined by spin-orbit scattering as well as valley scattering. In the absence of an in-plane field, the derived equation for the corresponding low-field magnetoresistance (MR) is given by[29]

$$\Delta\rho(B) = -\frac{e^2\rho^2}{2\pi h}\left[F\left(\frac{B_z}{B_\varphi}\right) - F\left(\frac{B_z}{B_\varphi + B_{asy}}\right) - 2F\left(\frac{B_z}{B_\varphi + B_{SO}}\right)\right] \quad (33)$$

$$F(\mathrm{z}) = \ln z + \psi\left(\frac{1}{2} + \frac{1}{z}\right), \qquad B_{\varphi,SO} = \frac{\hbar c}{4De}\tau_{\varphi,SO}^{-1}, \qquad B_{asy} = \frac{\hbar c}{2De}\tau_{asy}^{-1}, \qquad \tau_{SO}^{-1} = \tau_{sym}^{-1} + \tau_{asy}^{-1}$$

where ψ is digamma function, D is the diffusion coefficient, τ_{SO}^{-1} is spin-orbit scattering rate, τ_{asy}^{-1} is asymmetry spin-orbit scattering rate, and τ_{sym}^{-1} is symmetry spin-orbit scattering rate.

As shown figure 13, low-field MR would describe negative MR corresponding to weak localization in the absence of the spin-orbit coupling. And in the presence of symmetric spin-orbit coupling only, the contribution of the third term in equation 33 is declined, leading weak localization. If symmetry is broken, the second and third terms in equation 33 become negligible, leaving the first term to determine weak antilocalization behavior with positive magnetoresistance.

Recently, it was experimentally reported [55] that low-field MR in iridium-clustered graphene exhibited a weak localization with EY spin relaxation mechanism and the spin-orbit coupling strength of KM type therein was over 5.5 meV (figure 14 (a)). In other hand, for graphene/transition metal dichalcogenides (TMDC) heterostructure[56], the weak antilocalization of Bychkov-Rashba spin-orbit coupling type appeared with spin-orbit coupling value ~15 meV (figure 14 (b)).

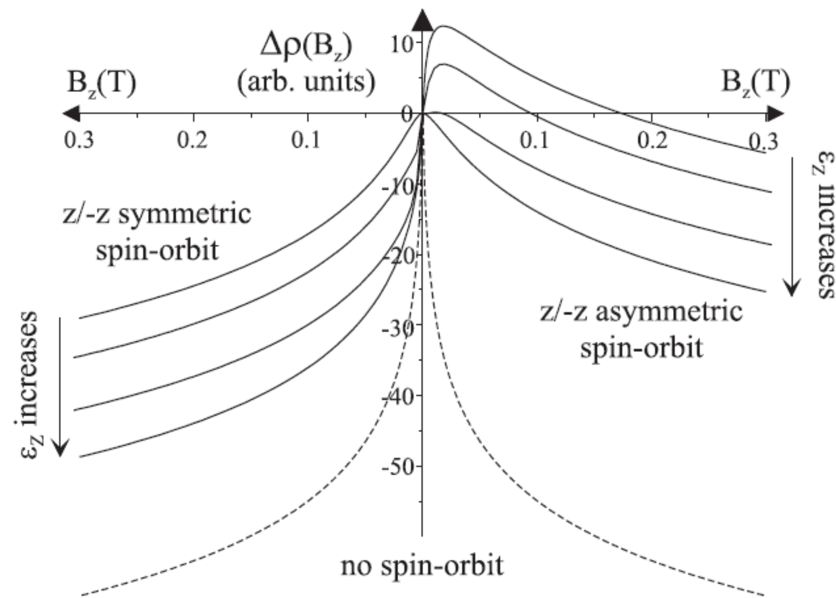

Figure 13. Weak localization in graphene due to spin-orbit scattering. The low-field magnetoresistivity in the presence of symmetric or asymmetric z direction (out of plane to graphene surface) spin-orbit scattering as compared to the absence of spin-orbit scattering. Solid curves show the influence of spin-orbit scattering with Zeeman energy[29].

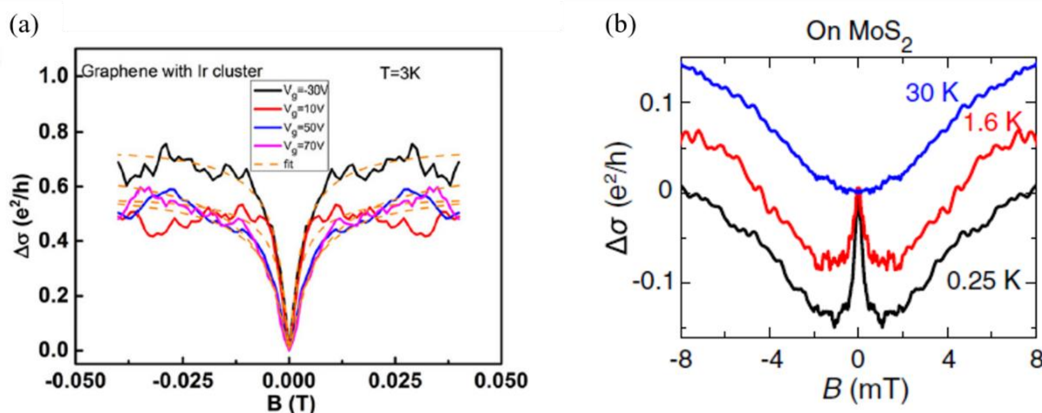

Figure 14. Weak localization and weak antilocalization of graphene heterostructure. (a) Weak localization of Ir-cluster-decorated graphene at various charge concentrations[55]. (b) Negative magnetoconductivity due to weak antilocalization in monolayer graphene on MoS_2 substrate at various temperature[56].

2.3 Local magnetic moment from point defect and adatoms on graphene.

The pristine graphene is relatively strong diamagnetic material because of Landau orbital diamagnetism. So, the possibility of making magnetic graphene has attracted much interest because the magnetic moment in graphene could meet the demands of ever increasing magnetic information storage density by engineering ultimately thin or two-dimensional magnetic material. For magnetic moments of graphene, there have been many theoretical[57-58]and experimental[59-62] studies by implanting vacancy defects and light adatoms. Theoretically, the existence of localized magnetic moments can be explained as a Lieb's theorem[63-64]. This theorem states that the ground state has magnetic moment with sublattice site on a bipartite lattice. Then, to substitute a site by an adatom or a vacancy should lead to a magnetic moment in the π band if the defect does not strongly couple with π and σ band[63].

R.R. Nair [61]et al showed that point defects, such as fluorine adatoms and vacancies induced by irradiation could accommodate moments with spin 1/2. Figure 15 shows the paramagnetism due to fluorine adatoms and vacancies in graphene. The magnetization of the fluorinated (figure 15 (a)) and vacancies defects (figure 15 (b)) graphene increases with increasing F/C ratio or defect density, respectively. The measured magnetization curves can be all described by the Brillouin function

$$M = \mathrm{N} gJ\mu_B \left[\frac{2J+1}{2J}\,\mathrm{ctnh}\left(\frac{(2J+1)z}{2J}\right) - \frac{1}{2J}\,\mathrm{ctnh}\left(\frac{z}{2J}\right)\right] \tag{34}$$

where $z=gJ\mu_B H/k_B T$, g is the g-factor, J is the angular momentum number and N is the number of spins. By fitting the experimental results with different values of J, it was found that only $J = S = 1/2$ (free electron spin) produced well matched Brillouin function fit.

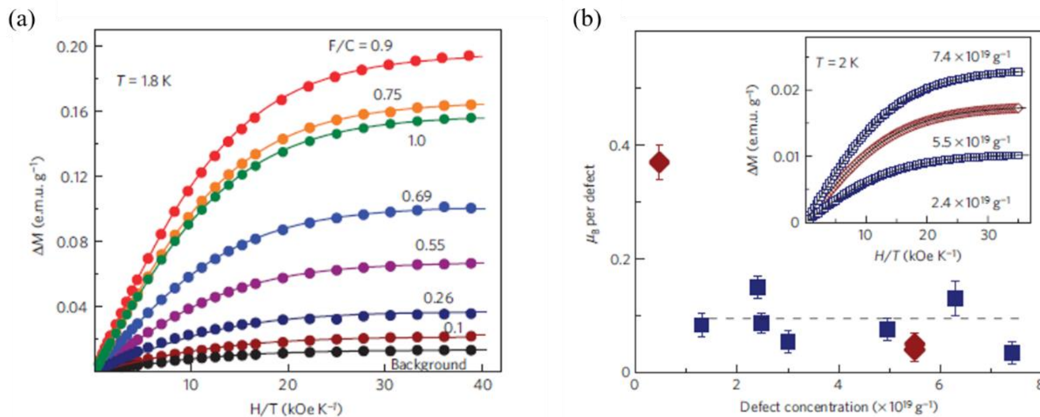

Figure 15. Paramagnetism due to (a) fluorine adatoms and (b) Vacancy. (a) Magnetic moment as a function of parallel field H for different F/C ratios. Solid curves are fits to equation (34) with S=1/2. (b) Magnetic moment normalized by the concentration of vacancies. Inset: magnetic moment as a function of parallel field H due to vacancy[61].

ULSAN NATIONAL INSTITUTE OF
SCIENCE AND TECHNOLOGY

In hydrogenated graphene, McCreary et al[60], showed that magnetic moment formation can be detected via spin transport with spin valve device. The hydrogen doping was achieved by exposing graphene spin valve samples to atomic hydrogen at 15 K in an ultrahigh-vacuum chamber and performing the spin transport measurement in situ. the non-local magnetoresistance curves exhibit a dip centered at zero magnetic field after hydrogen exposure as shown in figure 16. This is associated with magnetic moment formation in graphene. The underlying mechanism is spin scattering from exchange coupling with local magnetic moments. Also, the sharpening of the Hanle curve after hydrogen exposure indicates the formation of magnetic moments (figure 16 (b)) because the presence of exchange field can significantly enhance spin precession. They also observed a similar behavior with vacancy defects by argon sputtering,

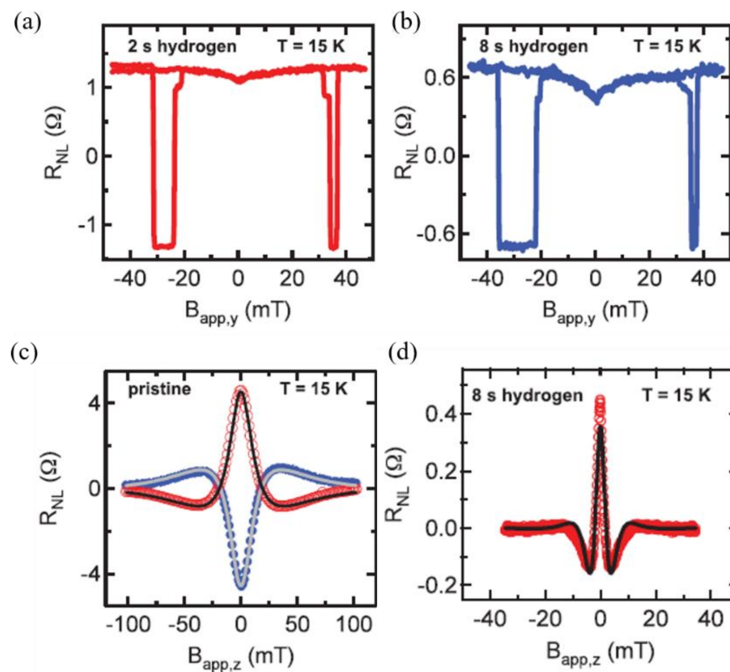

Figure 16. The effect of hydrogen exposure on spin transport in graphene from spin valve measurement. (a), (b) Nonlocal spin transport measurements after atomic hydrogen exposure for 2 and 8 s, respectively. Both curves exhibit a dip in nonlocal magnetoresistance at zero field. This means spin relaxation induced by localized magnetic moment. (c), (d) The dramatic narrowing of the Hanle precession peak is observed in 8 s hydrogenated graphene than pristine graphene. The sharpening of the Hanle curve results from the presence of an exchange field due to the atomic hydrogen in graphene[60].

2.4 Proximity effect on ferromagnetic substrate.

The magnetism in graphene can be induced by proximity effect with ferromagnetic insulator substrate as well as point defects of vacancies and adatoms. Because the hybridization between π orbital of graphene and the spin-polarized *d* orbital of magnetic insulator gives rise to the exchange interaction required for long-range ferromagnetic ordering, an electron in graphene/ferromagnetic insulator heterostructure is predicted to experience strong exchange field[65-70]. Therefore, the magnetic exchange field induced by an adjacent ferromagnetic insulator substrate enables to control local spin generation and spin modulation in graphene without the delicate material structure.

Recently, a large exchange field was observed in graphene/ferromagnetic insulator heterostructure[65]. As shown figure 17, the anomalous Hall effect(AHE) was emerged from the heterostructure with yttrium iron garnet (YIG). The AHE occurs with broken time-reversal symmetry as a consequence of SOC in a ferromagnetic phase. Also, Wei et al[68]. demonstrated that EuS/graphene system produced a substantial magnetic exchange field (~14T) which lead to orders-of-magnitude enhancement of spin signal originating from the Zeeman spin Hall effect as shown ib figure 18 (a). Furthermore, it was observed to the quantized spin-polarized edge transport expected because of the strong magnetic exchange field (figure 18(b)). Wu et al[67]. fabricated the $BiFeO_3$/graphene heterostructure and demonstrated the magnetic proximity effect of transport properties. With increasing external perpendicular magnetic field, the *N*=0 Landau level of graphene was converted from a ferromagnetic phase to a canted antiferromagnetic phase (figure 19), and the magnetic exchange field was estimated up to ~280T.

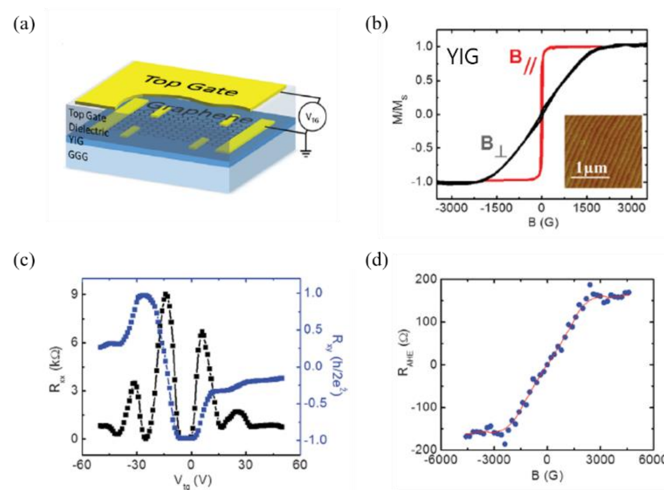

Figure 17. The anomalous Hall effect in graphene/YIG heterostructure. (a) Schematic drawing of the graphene/YIG device with top gate. (b) Magnetic hysteresis loops of YIG thin film in perpendicular and in-plane magnetic field. Inset: the AFM image of YIG film surface. (c) Quantum Hall effect of graphene/YIG device in an 8T perpendicular magnetic field at 2K. (d) the nonlinear Hall resistivity after the linear background is removed, indicating anomalous Hall effect[65].

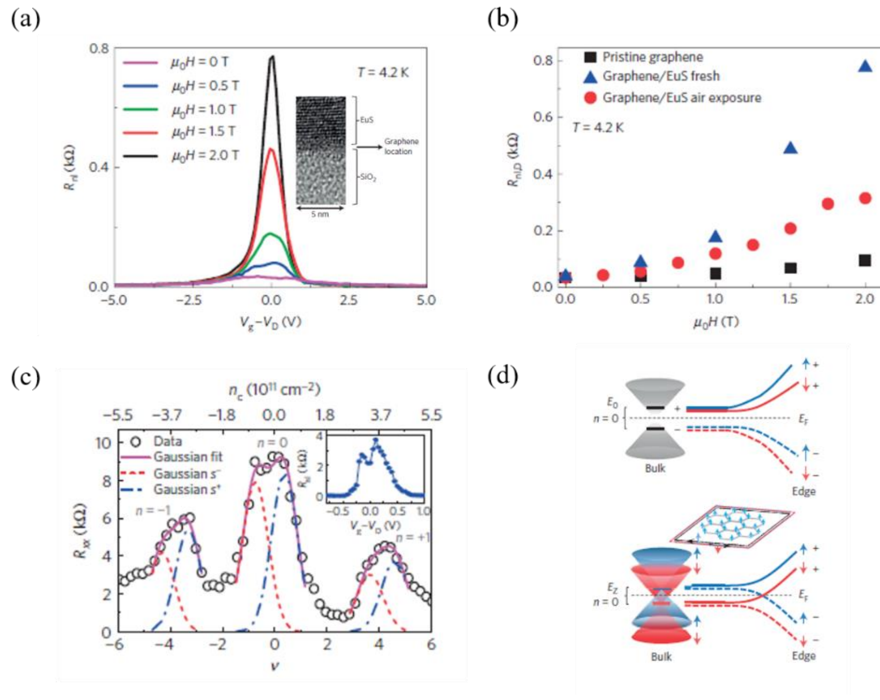

Figure 18. Zeeman spin Hall effect in graphene/EuS heterostructures. (a) Nonlocal resistance (this nonlocal signal will be discussed in next chapter "spin Hall effect" in detail) as a function of gate voltage under different magnetic field for CVD graphene/EuS heterostructure at 4.2K. The inset is a TEM cross-section image of the device. (b) Comparison of nonlocal resistance versus magnetic field at charger neutral point. (c), (d) the extra dip is observed at $\nu = 0$ and $\nu = +4$ and -4. The $\nu = 0$ state originates from the splitting of $n = 0$ Landau level and can either be a valley-polarized spin singlet or a spin-polarized valley singlet depending on the relative strength of valley versus spin splitting[68].

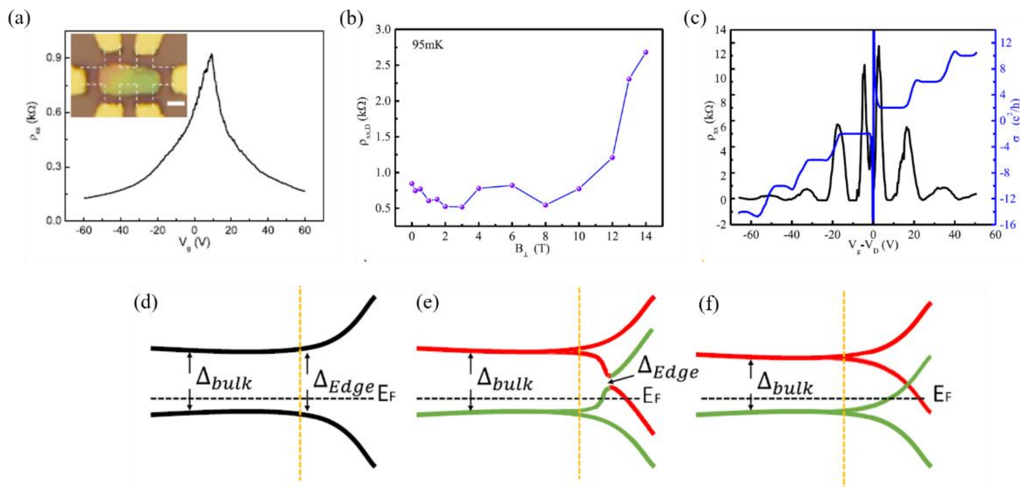

Figure 19. The proximity effect in graphene coupled to a $BiFeO_3$ nanoplate. (a) Back-gate voltage dependence of resistivity of the BFO/graphene heterostructure device. The inset is optical image of the device. The scale bar is 2μm. (d) the resistivity via magnetic field at charger neutral point. (c) transverse conductivity and longitudinal resistivity measured under 14T. (d)-(f) illustrations of the antiferromagnetic, canted antiferromagnetic, and ferromagnetic phase[67].

ULSAN NATIONAL INSTITUTE OF SCIENCE AND TECHNOLOGY

III Spin Hall effect

Spin Hall effect (SHE)[71-72] is a relativistic spin-orbit coupling phenomena. This effect converts charge currents into transverse spin current and vice versa in nonmagnetic conductor. In 1971, D'yakonov and Perel[73] predicted it based on the idea of asymmetric Mott scattering. Hirsch[74] rediscovered it and proposed an extrinsic SHE in 1999. Experimentally, the first measurement of SHE was performed on n-GaAs with magneto-optical Kerr microscope by Kato[75]*et* al in 2004. They demonstrated the presence of a spin accumulation close to the edge when electric field was applied along the channel. Valenzuela and Tinkham[76] showed an electrical detection of the spin hall effect in a diffusive metallic conductor using a nonlocal detection technique with lateral spin valve. The spin hall effect has become one of the promising ways to create pure spin currents in nonmagnetic materials without external magnetic field and ferromagnets.

In this chapter, I will briefly introduce what is the spin hall effect and review their origins based on both intrinsic and extrinsic mechanism. Lastly, I introduce the spin hall effect in graphene.

3.1 Spin Hall effect.

In 1879, the American physicist Edwin H. Hall observed a phenomenon that the electron receives the force, called the Lorentz force, against one side of the conductor when a current-carrying conductor is placed in perpendicular magnetic field[77]. The Lorentz force is given by $\mathbf{F} = q(\boldsymbol{E} + \boldsymbol{v} \times \boldsymbol{B})$, where v is the velocity of the particle and q the charge of the particle. The voltage difference between the two edges of the conductor is called Hall voltage V_H, and the ratio of the voltage to the electric current is Hall resistance $R_H = V_H / I$ which is linear in the magnetic field. This phenomenon is named as Hall effect. Later, Edwin H. Hall reported[78] that Hall resistance was ten times larger in ferromagnetic metal than in nonmagnetic conductor. This stronger Hall effect that Hall observed in ferromagnetic conductor became to be kwon as the anomalous Hall effect (AHE). An empirical behavior of anomalous Hall effect is given by

$$R_H = R_O B + R_A M \tag{35}$$

which has been applied to many materials over a broad range of external magnetic field. The second term represents the Hall effect (anomalous Hall effect) contribution from the spontaneous magnetization of ferromagnetic conductor. This means that Hall resistance can be detected in the absence of an external magnetic field in ferromagnetic conductor. This anomalous Hall effect cannot be simply understood as a result of the Lorentz force on charge current.

In 1954, Karplus and Luttinger (KL)[79] proposed a theory for the anomalous Hall effect and showed that electrons acquire an additional contribution to their group velocity when an external electric field is applied to a solid. KL's anomalous velocity was perpendicular to electric field and could contribution to the Hall resistance. The anomalous velocity can be expressed in terms of Berry phase and Berry curvature in moment space due to modified phase of Bloch state wave packets. Therefore, it has recently been referred to as the intrinsic contribution to the anomalous Hall effect because this contribution depends only on the band structure without impurity scattering. In the presence of disorder scattering in solid, the origin of anomalous Hall effect can have either skew scattering from impurities caused by spin-orbit coupling or side jump mechanism under influence of the electric field due to an impurity. These are extrinsic contribution to the anomalous Hall effect.

Here, upon applying electric field along the nonmagnetic conductor instead of ferromagnetic materials, generated transverse spin current only (no charge current) without external magnetic field is referred as the spin hall effect[71-72]. As shown in figure 20 (c), the separated spins induce either a pure spin current resulting in spun accumulation at the lateral sample edges. The reciprocal phenomenon of spin Hall effect is inverse spin Hall effect (ISHE) where pure spin current generates charge current or voltage. The mechanisms of the spin Hall effect have naturally emerged from the origins of anomalous Hall effect.

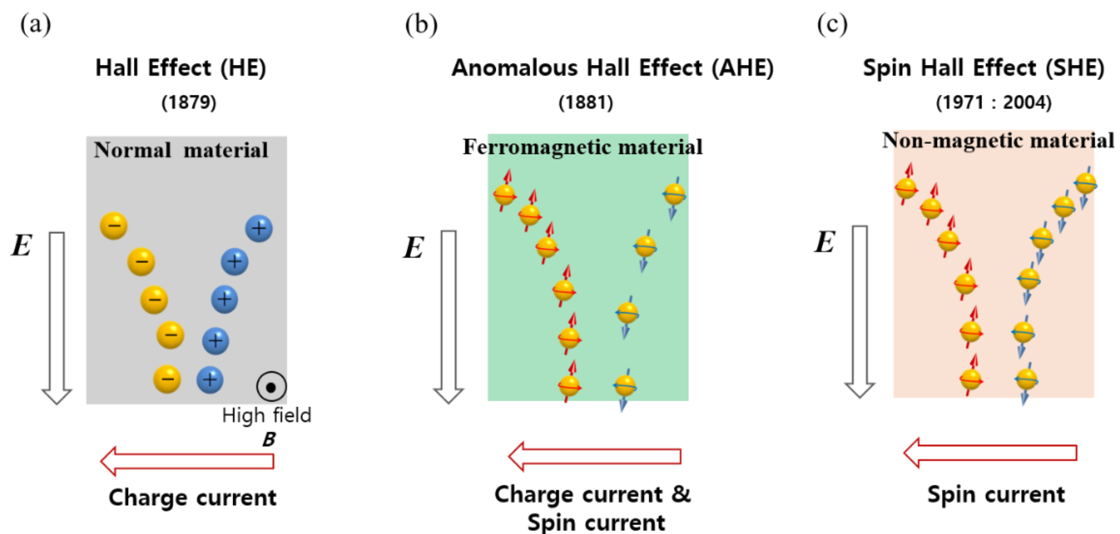

Figure 20. From the Hall effect to spin Hall effect. (a) Ordinary Hall effect due to Lorentz force. Only charge current is generated. (b) Anomalous Hall effect in ferromagnetic material. Both charge and spin current are generated. (c) Spin Hall effect in non-magnetic material. Only spin current is generated.

In 1971, the spin version of hall effect was first proposed by the Russian physicists Dyakonov and Perel[73] based on relativistic spin-orbit coupling. In their picture, spin-orbit coupling induces spin Hall effect via the Mott scattering of electrons on unpolarized impurities which results in spatial separation of electrons with opposite spins. Concepts for the experimental detection of spin Hall effect were introduced by Hirsch and Zhang in 1999[74] and 2000[80], respectively. Hirsch proposed a device in which a spin current is generated by spin Hall effect in one part and injected into another part where it is detected by inverse spin Hall effect. Zhang suggested that the edge spin accumulation produced by spin Hall effect could be detected electrically using a ferromagnetic probe.

The first measurement of spin Hall effect was observed with magneto-optical Kerr rotation microscope by Kato et al. as shown figure 21[75]. In this technique, the laser beam was linearly polarized, and the polarization axis of the reflected beam was determined. The rotation angle is proportional to the net magnetization along the beam direction. For this experiment, they used unstrained n-GaAs and strained n-InGaAs three-dimensional epilayers, which were patterned into $300 \times 77\ \mu m^2$ and $300 \times 33\ \mu m^2$ channels, respectively. The wafers were doped to low electron density of $n = 3 \times 10^{16} cm^{-3}$ to achieve long spin relaxation time of $\tau_s \sim 10$ ns. This corresponds to spin diffusion length of $L_s \sim 10$ μm. An electric field was applied along the channel while a magnetic field B could be applied perpendicular to it in the sample plane. As shown figure 21 (g), a two-dimensional scan of sample demonstrates the existence of spin accumulation close to the edges. The amplitude of the measured edge spin polarizations reached ~0.1%.

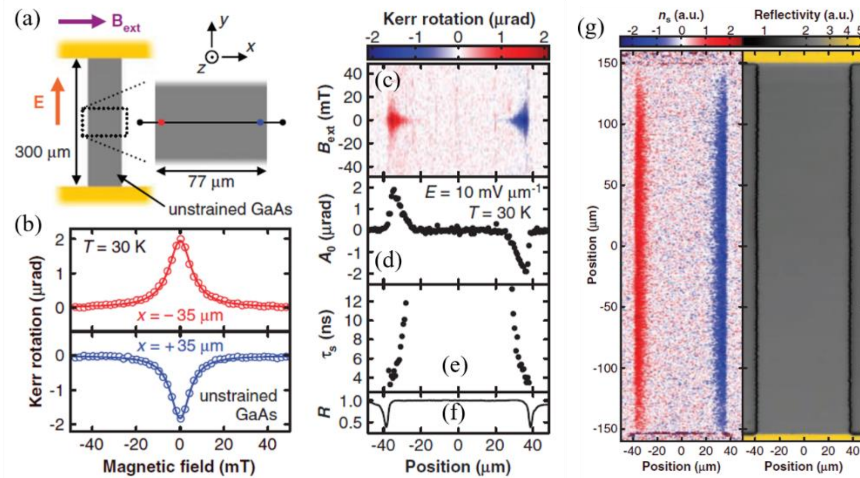

Figure 21. The spin Hall effect in unstrained GaAs. (a) schematic of the unstrained GaAs sample and the experimental geometry. (b) The measurement of Kerr rotation as a function of magnetic field. (c) Kerr rotation as a function of position. (d), (e) Spatial dependence of peak Kerr rotation A_0 and spin lifetime τ_s across the channel, respectively. (f) Reflectivity R as a function of position. (g) Two-dimensional image of spin density n_s and reflectivity R for the unstrained GaAs sample[75].

ULSAN NATIONAL INSTITUTE OF SCIENCE AND TECHNOLOGY

The electrical detection of spin hall effect was elusive because the transverse spin currents do not lead to different chemical potential. Therefore, the first experiment for electrical detection focused on the charge signal from inverse spin Hall effect. Valenzuela and Tinkham[76] performed experiments in which a spin current injected from a ferromagnetic electrode into a nonmagnetic metal strip was detected by ISHE and by the nonlocal spin valve using a ferromagnetic probe electrode as shown figure 22. A spin-polarized current from CoFe(80% Co) electrode is injected in a Al strip. The spin current propagates to both side away from the injection point and decays within the spin diffusion length. Then, a laterally voltage V_{ISHE} induced from inverse spin Hall effect is measured using a Hall-cross structure. In this case, the total change in nonlocal spin Hall resistance (R_{ISHE}) in given by

$$\Delta R_{SH} = \frac{p}{t_{\mathrm{Al}}} \frac{\sigma_{SH}}{\sigma_c^2} exp\left(-\frac{L_{SH}}{\lambda_{sf}}\right) \tag{36}$$

where P is the polarization of the electrically injected current, t is the thickness of Al, λ_{sf} is the spin diffusion length, σ_{SH} and σ_{c} are spin and charge conductivity, respectively. By fitting the measured Hall resistance R_{ISHE} with equation (36) for the injected pure spin current, spin Hall angle ($\sigma_{\mathrm{SH}}/\sigma_{\mathrm{c}}$) is estimated to be 0.01~0.03 %,

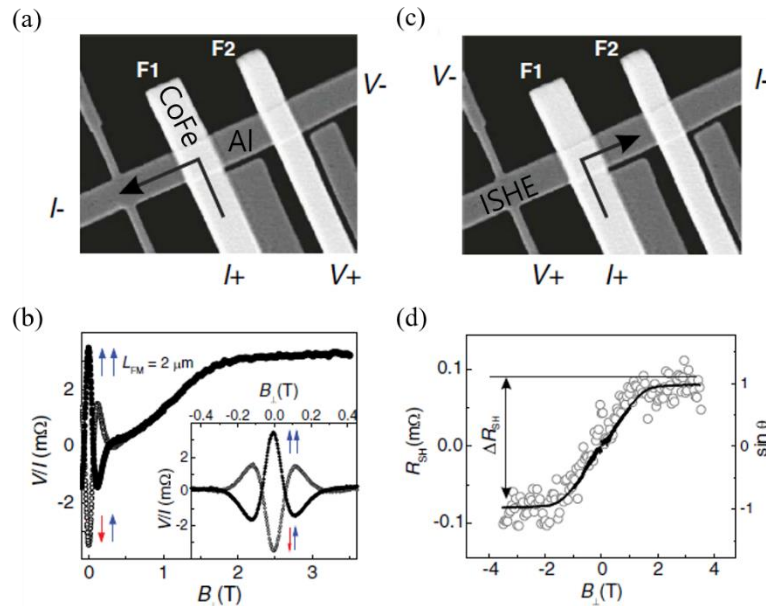

Figure 22. Electrical measurement of spin Hall effect in Al. (a) SEM image of device and the measurement scheme for non-local spin diffusion. (b) Hanle curve as a function of perpendicular magnetic field. The arrows indicate the relative orientation of the magnetization F1 and F2. (c) SEM image of device and the measurement scheme for inverse spin Hall effect. (d) Spin Hall resistance R_{SH} versus perpendicular magnetic field[76].

3.2 Intrinsic mechanism of spin Hall effect.

The spin-dependent Hall effect that are AHE, SHE, ISHE originate from the intrinsic, skew, and/or side jump mechanism, Intrinsic mechanism can be explained by an anomalous velocity arising from a Berry phase in momentum space. Berry phase is similar to the Aharonov-Bohm phase of a charged particle traversing a loop in the presence of a magnetic flux[81].

Consider a physical system described by Hamiltonian that depends on time through a set of parameters, denoted by $\boldsymbol{R} = (R_1, R_2, \ldots)$,

$$H = H(\mathbf{R}),\ \boldsymbol{R} = \boldsymbol{R}(\mathrm{t}) \tag{37}$$

If R(t) moves slowly along a path C in the parameter space (in the adiabatic evolution of the system), it is useful to introduce an instantaneous orthonormal basis from the eigenstates of H(R) at each value of the parameter R.

$$H(\boldsymbol{R})|n(\boldsymbol{R})\rangle = \varepsilon_n(R)|n(\boldsymbol{R})\rangle \tag{38}$$

However, this equation does not completely determine the basis function $|n(\boldsymbol{R})\rangle$ because of the phase uncertainty. It still allows an arbitrary R-dependent phase factor of $|n(\boldsymbol{R})\rangle$. One can make a phase choice to remove this arbitrariness. Here, we can require that the phase of the basis function is smooth and single valued along the path C in the parameter space. According to the quantum adiabatic theorem, a system initially in one of its eigenstates will stay as an instantaneous eigenstate of the Hamiltonian throughout the process. The eigenstate at time t can be written as

$$|\psi_n(t)\rangle = e^{i\gamma_n(t)} exp\left[-\frac{i}{\hbar}\int_0^t dt'\varepsilon_n(\boldsymbol{R}(t'))\right]|n(\boldsymbol{R}(t))\rangle \tag{39}$$

where the second exponential is known as the dynamical phase factor. Inserting equation (39) into the time-dependent Schrodinger equation

$$i\hbar\frac{\partial}{\partial t}|\psi_n(t)\rangle = H(\boldsymbol{R}(t))|\psi_n(t)\rangle \tag{40}$$

and

$$\langle n(\boldsymbol{R}(t))|i\hbar\frac{\partial}{\partial t}|\psi_n(t)\rangle = \langle n(\boldsymbol{R}(t))|H(\boldsymbol{R}(t))|\psi_n(t)\rangle$$

One finds that γ_n can be expressed as a path integral in the parameter space.

ULSAN NATIONAL INSTITUTE OF SCIENCE AND TECHNOLOGY

$$\gamma_n = \int_C dR \cdot A_n(\boldsymbol{R}), \qquad A_n(\boldsymbol{R}) = i\left\langle n(\boldsymbol{R}) \middle| \frac{\partial}{\partial \boldsymbol{R}} \middle| n(\boldsymbol{R}) \right\rangle \tag{41}$$

This vector $A_n(\boldsymbol{R})$ is called the Berry connection or the Berry vector potential, and gauge dependent.

In addition to the dynamical phase, equation (41) shows that the quantum state will acquire an additional phase γ_n during the adiabatic evolution.

If we make a gauge transformation

$$|n(\boldsymbol{R})\rangle \rightarrow e^{i\zeta_n(t)}|n(\boldsymbol{R}(t))\rangle \tag{42}$$

the phase γ_n will be changed by $\zeta_n((\boldsymbol{R}(0)) - \zeta_n((\boldsymbol{R}(T))$ for initial and final points of the path C after transformation. For a cyclic evolution of the system along a closed path C with $\boldsymbol{R}$(T) = $\boldsymbol{R}$(0), the single-valued condition of $e^{i\zeta_n(t)}$ on the basis function $|n(\boldsymbol{R})\rangle$ implies

$$\zeta_n((\boldsymbol{R}(0)) - \zeta_n((\boldsymbol{R}(T)) = 2\pi \times integer \tag{43}$$

This shows that γ_n can be only changed by an integer multiple of 2π under the gauge transformation and it cannot be removed. Therefore, for a closed path C, γ_n becomes a gauge-invariant physical quantity. Now, it is well known as the Berry phase or geometric phase[81-82]. In general, it is given as

$$\gamma_n = \oint dR \cdot A_n(\boldsymbol{R}) \tag{44}$$

By using the Stokes' theorem, γ_n can be expressed as an area integral

$$\gamma_n = \int_S dS \cdot (\boldsymbol{\nabla}_{\boldsymbol{R}} \times A_n(\boldsymbol{R})) \tag{45}$$

where we can define the Berry curvature from the Berry connection as

$$\boldsymbol{\Omega}_n(\boldsymbol{R}) = \boldsymbol{\nabla}_{\boldsymbol{R}} \times A_n(\boldsymbol{R}) \tag{46}$$

This Berry curvature is like the magnetic field in moment space, and the integral of the curvature over closed surfaces is known to be topological and as Chern number quantized as integer (quantum Hall effect)[81].

Now, consider a crystal under the perturbation of a weak electric field[81]. In the presence of electromagnetic fields, the Hamiltonian is given by

ULSAN NATIONAL INSTITUTE OF
SCIENCE AND TECHNOLOGY

$$H = \frac{[\boldsymbol{P}+e\boldsymbol{A}(\boldsymbol{r})]^2}{2m} + V(\boldsymbol{r}) - e\emptyset(\boldsymbol{r}) \tag{47}$$

where $V(\boldsymbol{r})$ is the periodic lattice potential, and A(r) and ϕ(r) are the electromagnetic potential. The approximate Hamiltonian that wave packet feels can be obtained by linearizing the perturbations about the wave-packet center $\boldsymbol{r}_c$ as $H \approx H_c + \Delta H$

$$H_c = \frac{[\boldsymbol{P}+e\boldsymbol{A}(\boldsymbol{r_c})]^2}{2m} + V(\boldsymbol{r_c}) - e\emptyset(\boldsymbol{r_c}), \qquad \Delta H = \frac{e}{2m}[\boldsymbol{A}(\boldsymbol{r}) - \boldsymbol{A}(\boldsymbol{r_c}), \boldsymbol{p}] - e\boldsymbol{E}\cdot(\boldsymbol{r}-\boldsymbol{r_c}) \tag{48}$$

where [,] is the anticommutator. The wave packet can be written as

$$|W(\boldsymbol{k}_c, \boldsymbol{r}_c)\rangle = e^{-(ie/\hbar)\boldsymbol{A}(r_c)\cdot\boldsymbol{r}}|W_0(\boldsymbol{k}_c, \boldsymbol{r}_c)\rangle \tag{49}$$

where $|W_0\rangle$ is the wave packet constructed using the unperturbed Bloch functions. The wave-packet dynamics can be obtained from the time-dependent variational principles. The Lagrangian is obtained with wave packet as

$$L = \left\langle W \middle| i\hbar\frac{\partial}{\partial t} - H \middle| W \right\rangle \tag{50}$$

And then, by the Euler-Lagrange equation

$$\frac{\partial}{\partial t}\frac{\partial L}{\partial \dot{\boldsymbol{k}}} - \frac{\partial L}{\partial \boldsymbol{k}} = 0 \quad and \quad \frac{\partial}{\partial t}\frac{\partial L}{\partial \dot{\boldsymbol{r}}} - \frac{\partial L}{\partial \boldsymbol{r}} = 0 \tag{51}$$

Equation of motion can be obtained as

$$\dot{\boldsymbol{r}} = \frac{\partial \varepsilon(\boldsymbol{k})}{\hbar\partial \boldsymbol{k}} - \dot{\boldsymbol{k}} \times \boldsymbol{\Omega}(\boldsymbol{k}) \tag{52}$$

and

$$\hbar\dot{\boldsymbol{k}} = -e\boldsymbol{E} - e\dot{\boldsymbol{r}} \times \boldsymbol{B} \tag{53}$$

In equation 52, the electron velocity gains an extra velocity term proportional to the Berry curvature[81]. This is called anomalous velocity. Equation 53 is well known as Lorentz force.

The anomalous velocity has physical significance. Berry curvature is often proportional to the spin $\boldsymbol{S}$. Then, in the presence of an electric field, the anomalous velocity is proportional to $\dot{\boldsymbol{k}} \times \boldsymbol{S}$, and the

ULSAN NATIONAL INSTITUTE OF SCIENCE AND TECHNOLOGY

trajectories of spin-up and spin down are separated toward opposite directions transverse to the electric field. If the populations of spin-up and down are different, a net transverse current can exist. Then, this leads to the anomalous Hall effect in a ferromagnet. If the populations of spins are equal, the net electric Hall current is zero. However, the spin Hall current can still be nonzero. This is the intrinsic mechanism of spin Hall effect (SHE)[71, 81].

3.3 Extrinsic mechanism of spin Hall effect.

In addition to the intrinsic mechanism from anomalous velocity, impurity scattering is another source for SHE in the presence of strong spin-orbit coupling[72, 74]. There are the skew scattering[83] and the side jump mechanism[84]. The skew scattering defined by Smit[83] to explain anomalous Hall conductivity is asymmetry scattering of spin up and down due to spin orbit coupling. it is also known as Mott skew scattering. As mentioned in section 1.2, the coupling between the orbital and spin of electrons is a relativistic effect described formally by the non-relativistic expansion. However, the spin-orbit coupling can be also extracted from the semi-classical analysis[85] that usually invokes the interaction of the electron magnetic dipole moment associated with spin. In the instantaneous rest frame of an electron, an effective magnetic field can be obtained by Lorentz transforming the electric field from the laboratory frame. Then, an electric dipole moment in laboratory frame is given by[85]

$$\boldsymbol{P}_{lab} = \boldsymbol{v} \times \frac{\boldsymbol{\mu}}{c^2} \quad (54)$$

where c is light velocity, $\boldsymbol{\mu}$ is magnetic dipole with velocity $\boldsymbol{v}$, and the right-hand side is evaluated in the electron rest frame. The potential energy of spin-orbit coupling from electric dipole and Thomas precession is given as

$$U_{SO} = U_{Dipole} + U_{Thomas} = \frac{-\mathbf{P}_{lab} \cdot \mathbf{E}_{lab}}{2} \quad (55)$$

where E_{lab} is external electric field in the lab frame.

Because the electric dipole feels the force $F = (\boldsymbol{P}_{lab} \cdot \nabla)\boldsymbol{E}_{lab}$ in the lab frame, the impurity scattering of electrons with spin-orbit coupling deflects the spin up and down particle in opposite direction. This classical picture can only explain aspect of the spin-orbit dependent interaction with impurity[85-86].

Now, consider spin-orbit coupling in quantum mechanics[87].

$$V_{eff} = V(r) + \frac{1}{2mc^2}\frac{1}{r}\frac{dV(r)}{dr}\hat{\boldsymbol{L}} \cdot \hat{\boldsymbol{S}} \quad (56)$$

This equation (56) indicates potential energy for electron scattering from impurity, where V(r) is potential energy without spin-orbit coupling, and the second term is spin-orbit coupling term introduced in section 1.2. As shown figure 23 (a), the $\hat{\boldsymbol{L}} \cdot \hat{\boldsymbol{S}}$ is added to non-spin orbit coupling potential energy

ULSAN NATIONAL INSTITUTE OF SCIENCE AND TECHNOLOGY

V(r) when spin-up is scattered upward by impurity because $\hat{L}\cdot\hat{S}$ term become positive value.

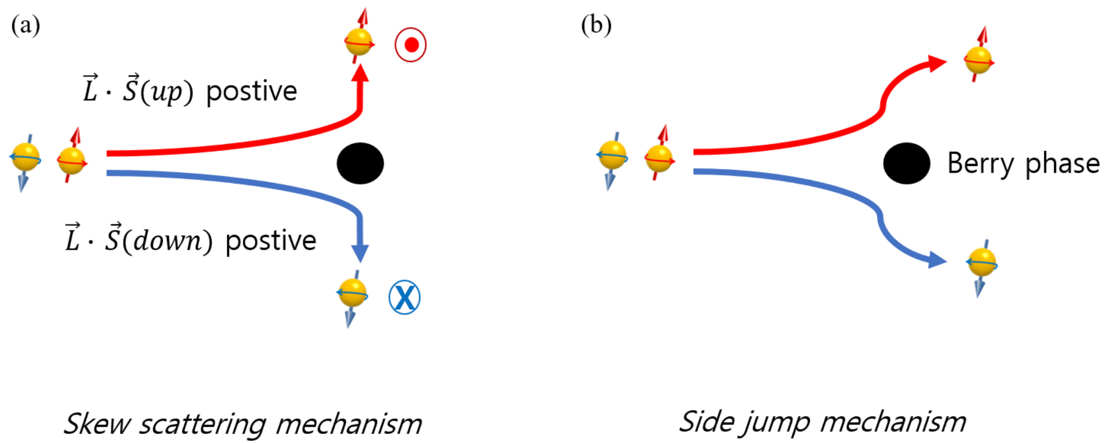

Figure 23. Extrinsic mechanism of spin Hall effect. (a) Skew scattering mechanism by spin dependent scattering at impurity center. (b) Side jump mechanism from change of Berry phase around impurity[87].

If spin-up is scattered downward by impurity, the $\hat{L}\cdot\hat{S}$ is subtracted from non-spin orbit coupling potential energy V(r). On the other hand, when spin-down is scattered downward by impurity, the $\hat{L}\cdot\hat{S}$ adds to non-spin orbit coupling potential energy V(r) because $\hat{L}\cdot\hat{S}$ term become positive value. Then, the spin-up scattered upward has the larger value of scattering angle then spin-up scattered downward, and the spin-down scattered downward has the larger value of scattering angle then spin-down scattered upward. Therefore, the spin-up(down) is more scattered upward(downward), and spin splitting occur. This mechanism (equation (55,56)) is referred to as skew scattering mechanism. The spin Hall resistivity from skew scattering is directly proportional to the longitudinal charge resistivity and dependent of impurity concentration.

Figure 23 (b) show the side-jump mechanism[87]. The basic semiclassical argument for this mechanism can be stated that a wave of electron with incident wave vector k will experience a displacement transverse to k when considering the scattering of a Gaussian wave packet from a spherical impurity with spin-orbit coupling (equation 26). This effect was first noticed by Smit in 1955[88] but discarded and reintroduced by Berger[89] in 1964 to explain anomalous Hall effect.

Also, this mechanism can be explained with the additional phase (Berry phase)[81-82] of the wave-packet due to gradient potential energy around the impurity as shown figure 23 (b). When the wave-packet is scattered by the impurity, the momentum of the wave-packet changes from initial k_i to final k_f. At this time, the Berry phase from impurity transforms the position of the wave-packet dependent on spin state and only generate displacement transverse between spin-up k_f and spin-down k_f without a change of the progress of wave-packet.

ULSAN NATIONAL INSTITUTE OF SCIENCE AND TECHNOLOGY

The common conception for side jump mechanism can be generally computed by considering the spin-orbit coupling of the disorder scattering potential. This can only be justified in a weak spin-orbit coupled system. However, when addressing materials with strong spin-orbit coupling, there are always two sources of side jump scattering[71].

One is extrinsic side jump that is the contribution arising from thee non-spin orbit coupled part of the wave-packet scattering off the spin orbit coupled disorder. The other is intrinsic side jump that is the contribution arising from the spin orbit coupled part of the wave-packet formed by Block electrons scattering off the scalar potential alone without spin orbit coupling. Both can be independent of each other and dependent on the crystalline and the type of scattering impurity[71].

3.4 Spin Hall effect in graphene.

Graphene has attracted great attention for two dimensional spintronics because of the achievement of spin transport with long spin diffusion length of several micrometer from weak intrinsic spin orbit coupling at room temperature as discussed in section 1.2. However, controlling spin orbit coupling in graphene allows us to realize the topological state, such as quantum spin hall effect and spin hall effect in addition to spin channel.

Castro Neto and Guinea[90] theoretically studied the effect of impurities, such as hydrogenation, in inducing spin-orbit coupling in graphene and argued that the impurities can lead to a strong enhancement of spin-orbit coupling due to the sp^3 distortion induced by an impurity as shown figure 24. They considered Hamiltonian with π band and σ band of flat graphene, and local change in the hopping energies due to the presence of sp^3 distortion induced by an impurity.

The local value of the spin orbit coupling can be estimated as[90]

$$\frac{\Delta_{SO}^{I}(A)}{\Delta_{SO}^{at}} \approx A\sqrt{3(1-A^2)} \tag{57}$$

where Δ_{SO}^{at} is atomic spin orbit coupling, Δ_{SO}^{I} is spin orbit coupling from impurity and A is a degree of distortion. For the sp^2 case(A=0), this term vanishes and atomic spin orbit coupling only contributes for ~10 μeV. However, the value of SOC can be as high as ~7meV for the sp^3 case(A=1/2).

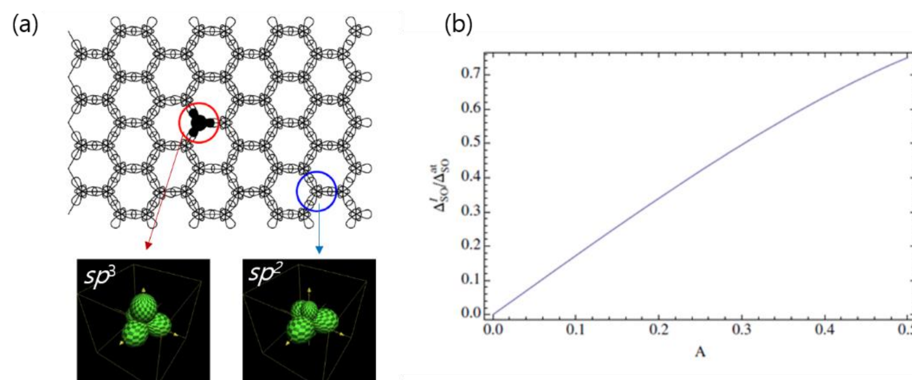

Figure 24. Induced spin-orbit coupling in graphene due to impurity. (a) the graphene lattice with its orbital. The sp^3 orbital at impurity position and the sp^2 orbital of the flat graphene lattice. (b) Relative value of the spin-orbit coupling at the impurity site and the atomic value in carbon as a function of A in equation 57 [90].

ULSAN NATIONAL INSTITUTE OF
SCIENCE AND TECHNOLOGY

Also, Weeks and coworker[91] proposed that the strength of the intrinsic spin-orbit coupling can be largely enhanced in single-layer graphene by heavy adatom such as indium (In) and thallium (Tl). The enhancement is due to second-neighbor hopping that is mediated by the p orbitals of the adatoms, which strongly hybridize with the unoccupied π level of graphene. The enhancement of the intrinsic spin-orbit coupling can lead to a band gap of the ~20 meV, and they demonstrated that dilute heavy adatoms can stabilize a robust quantum spin Hall state in graphene, theoretically[91].

In 2013, the spin Hall effect in hydrogenated graphene[92], which has been used as a model system to enhance spin orbit coupling in graphene, was observed with non-local measurement. Here, the non-local measurement is method to find spin Hall effect with inverse spin hall effect in an H-bar device proposed by Hankiewicz et al. similarly to the Mott double-scattering experiment. As shown in figure 25 (a), the charge current generates a transverse spin current due to spin Hall effect, and the spin current injected into channel generates an electrical voltage across the second leg from inverse spin Hall effect. Balakrishnan and co-worker introduced small amounts of covalently bonded hydrogen atoms to the graphene lattice by the dissociation of hydrogen silsesquioxane resist, and the extent of hydrogenation was ~0.05%. With increasing hydrogenation, non-local resistance (R_{NL}) at charge neutral point (carrier density(n) = 0) showed increase as shown figure 25 (c). Whether the non-local resistance is spin signal or not was confirmed by the non-monotonic oscillatory behavior of the non-local signal in an applied in-plane magnetic field. Figure 25 (d) shows the in-plane field dependence of non-local resistance for the device with 0.01% hydrogenation at T=4K, and a fitting oscillating non-local signal using[93]

$$R_{NL} = \frac{1}{2}\gamma^2 \rho W Re\left[\left(\sqrt{1+i\omega_B\tau_s}/\lambda_s\right)e^{-\left(\sqrt{1+i\omega_B\tau_s}/\lambda_s\right)|L|}\right] \tag{58}$$

where γ is the spin Hall angle, L is length of spin channel, W is width of channel and ω_B is Larmor frequency. The spin Hall angle of the graphene device with 0.01% hydrogenation was 0.18. this oscillatory behavior of non-local resistance can be a direct signature of spin Hall effect arising from the enhancement of spin orbit coupling due to hydrogenation.

Besides, in same group[94], they showed that the CVD (chemical vapour deposition) graphene from Cu foil can have a spin orbit coupling larger than that of pristine graphene because of the presence of residual Cu adatoms introduced during the growth and transfer process as shown figure 26. From a non-monotonic oscillatory dependence of the non-local signal with equation 58, the spin Hall angle of the CVD graphene was γ ~ 0.2 at room temperature. Also, they reported that Au and Ag can be used to induce the strong spin orbit coupling in pristine graphene.

However, these experiments for spin hall effect in graphene with H type device cause controversy whether non-local resistance is signal from spin hall effect or any other mechanism.

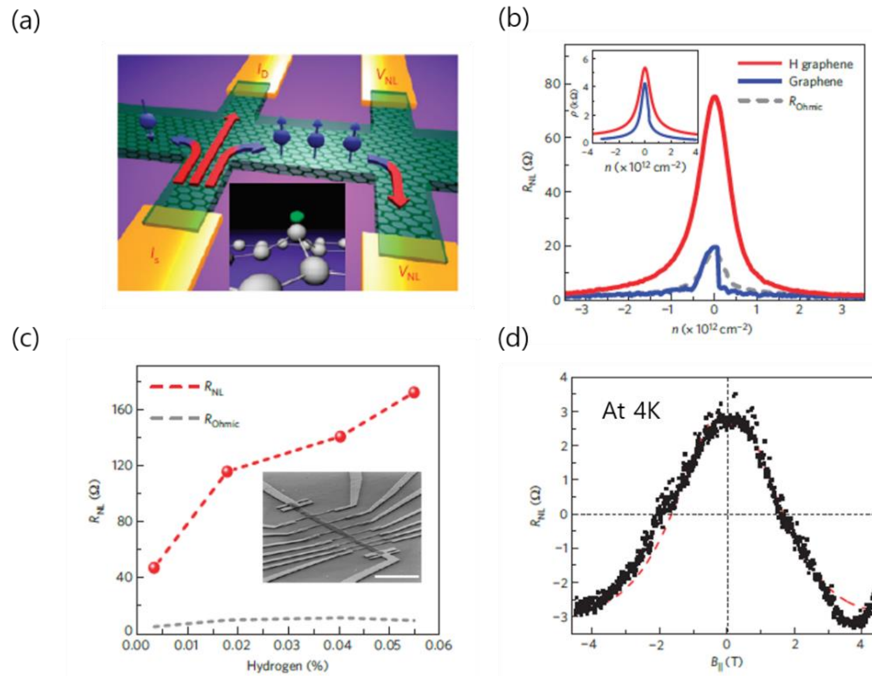

Figure 25. The spin Hall effect in hydrogenated graphene. (a) Measurement schematics for the non-local spin Hall resistance. Insert is schematics showing the deformation of the graphene hexagonal lattice due to hydrogenation. (b). Nonlocal resistance versus carrier density for pristine graphene and hydrogenated graphene. Ohmic contribution is considered in both samples. (c) Dependence of the nonlocal resistance on the percentage on hydrogenation. The dark grey dashed lines are the Ohmic contribution for this sample. The inset is SEM image of hydrogenated graphene Hall bar device. Scale bar is 5 μm. (d) Magnetic field dependence of nonlocal resistance for the device with 0.01% hydrogenation at 4K[92].

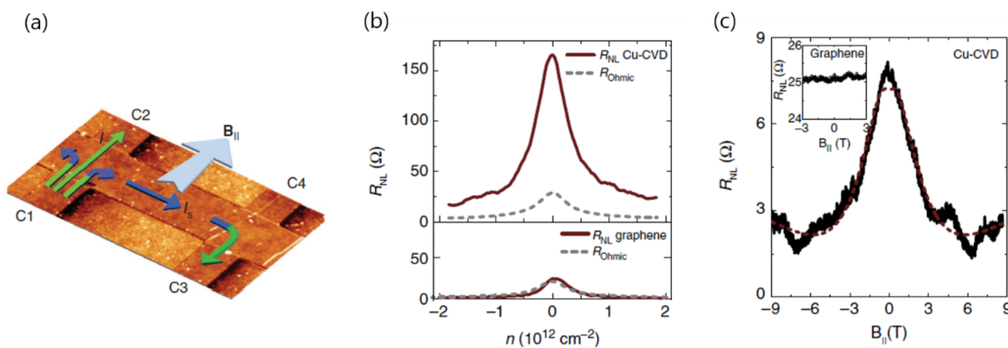

Figure 26. The spin Hall effect in CVD graphene. (a) AFM three-dimensional surface topography of a spin Hall device with details of actual measurement configurations. (b) Nonlocal resistance versus carrier density for pristine graphene and CVD graphene. Ohmic contribution is considered in both samples. (c) the in-plane magnetic field dependence of the non-local signal for CVD graphene. The inset is magnetic field dependence of pristine exfoliated graphene[94].

In 2015, Kaverzin and van Wees[95] modified Hall bar-shaped graphene samples by covering them with a hydrogen silsesquioxane film to hydrogenate into graphene and measured non-local resistance as shown figure 27 (a-c). They also observed reproducibly and consistently a presence of non-local resistance at charge neutral point in a number of different devises. However, the spin hall angle of $\gamma \sim 1.5$ was obtained from channel length dependence. This high value is unrealistic because the 100% conversion between the charge and spin currents means $\gamma \sim 1$. Moreover, spin precession was not observed with the applied in-plane magnetic field up to 7T. Therefore, they argued that the non-local resistance at charge neutral point in hydrogenated graphene is an effect of unknown origin and an alternative interpretation is required.

Wang and coworker[96] reported that the non-local resistance in the Au or Ir-decorated graphene was observed reproducibly but the evidence of spin signal induced spin hall effect cannot be found in the in-plane magnetic field up to 6T as shown figure 27 (f). They suggested the possibility of neutral Hall effect from disorder induced valley Hall effect in that system, not spin Hall effect.

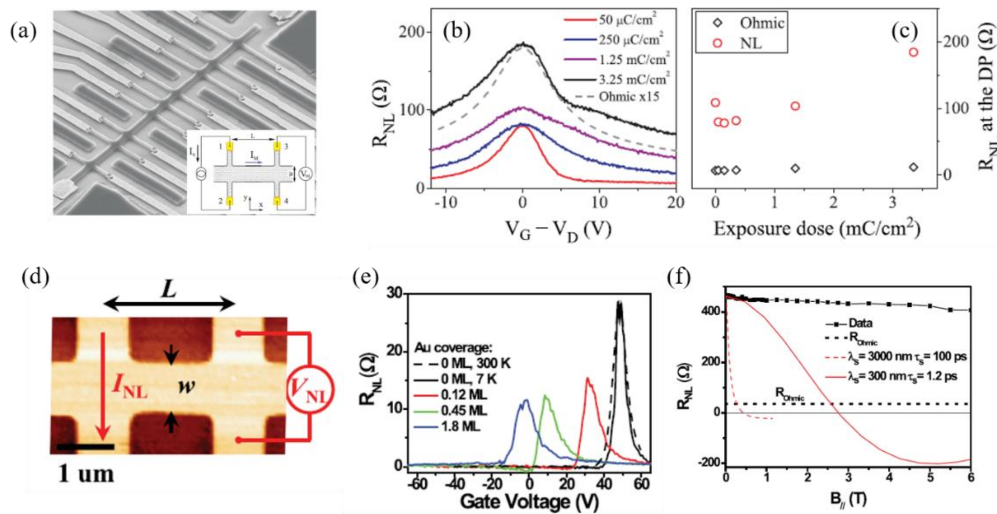

Figure 27. No spin Hall effect in hydrogenated (a-c)[95] and adatom-decorated graphene(d-f) [96]. (a) SEM image of hydrogenated graphene. The inset is schematic of the measuring circuit and the measured region of the sample. (b) The nonlocal resistance as a function of gate voltage for different exposures. (c) The nonlocal resistance at charge neutral point along with the corresponding values of Ohmic contribution. (d) AFM image of adatom-decorated graphene. (e) Nonlocal resistance versus gate voltage curves for pristine graphene and Au-decorated graphene. (f) Nonlocal resistance as a function of parallel magnetic field. The red lines are calculated Hanle precession.

ULSAN NATIONAL INSTITUTE OF SCIENCE AND TECHNOLOGY

IV. Experimental method

In this chapter, I will describe my experimental method and process for the experiment of spin Hall effect in graphene. Briefly, a monolayer graphene was prepared by a chemical vapor deposition (CVD) and transferred onto a SiO_2 substrate using wet transfer technique[97]. The graphene Hall bar device was made with photo and E-beam lithography, and spin and charge transport properties were measured from DC measurement in the chamber of PPMS (physical properties measurement system).

4.1 Material preparation and device fabrication.

Synthesis and transfer of graphene.

A monolayer graphene was grown on a polycrystalline Cu foil using a chemical vapor deposition method demonstrated elsewhere. Shortly, 25 μm copper foil (Alfa Aesar, 99.8% purity) was electropolished in phosphoric acid for 15 min and rinsed with distilled water followed by isopropyl alcohol (IPA). The copper foil was loaded into a quartz tube 3-zone furnace and the temperature was increased to 1050 °C in the H_2 environment for removal of native oxides in the copper with surface reconstruction. The graphene was synthesized by introducing CH_4 gas under H_2 gas insertion with a ratio of 10:5 (sccm) for 15 min, and transferred onto the Si/SiO_2 (300 nm) subatrate using a polymethyl methacrylate (PMMA) wet transfer process as shown in figure 28. To remove possible resist residues, samples were annealed in low vacuum at 300 °C[97].

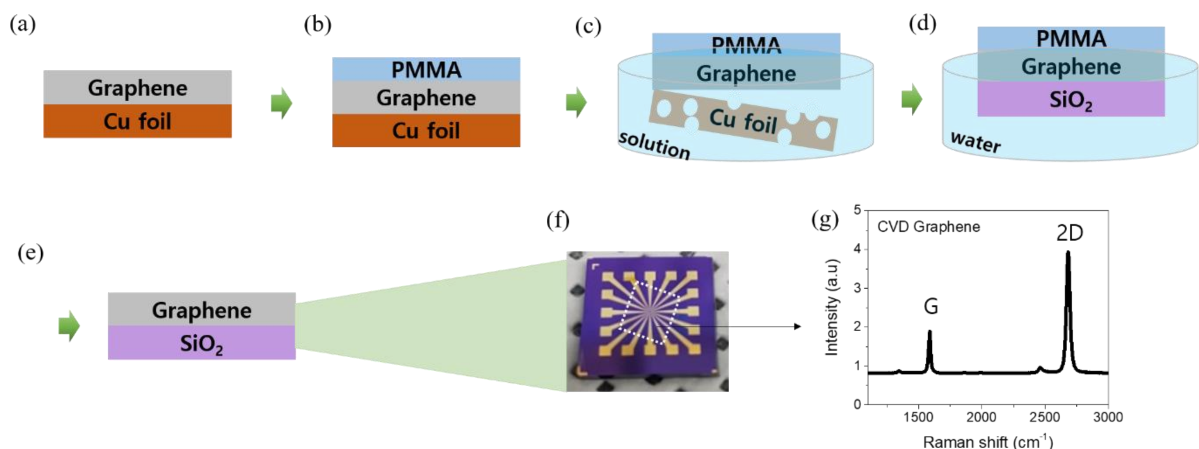

Figure 28. The process of graphene wet transfer. (a) the graphene on Cu foil from CVD. (b) Coating PMMA on a graphene with spin coating. (c) to remove the Cu foil, the sample is etched in solution. (d) a transference of graphene on SiO_2 substrate in water. (e), (f) Finally, the PMMA on graphene is removed by acetone. (g) A Raman spectroscopy of graphene for single layer and the quality of CVD graphene.

ULSAN NATIONAL INSTITUTE OF SCIENCE AND TECHNOLOGY

The fabrication of graphene Hall bar device.

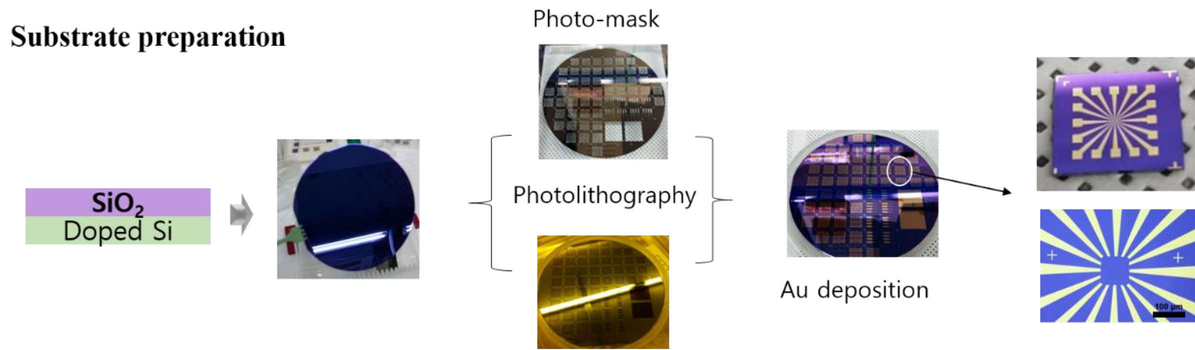

Figure 29. The preparation of the substrate with large electrode before graphene transfer. To facilitate the making graphene Hall bar device with E-beam lithography. The substrate is prepared with large electrode (Au) from photolithography. The AZ 5214 photoresist was used for electrode pattern.

Before the monolayer graphene grown from CVD method is transferred onto this substrate using wet transfer technique, the base substrate with a large electrode is prepared by photolithography for the short process of e-beam lithography. The figure 29 shows a process of manufacture for the substrate with large electrode. Next, the graphene on the substrate is covered with Au of small electrode by employing electron beam lithography and using auto-CAD software as shown figure 30. The Au (60 nm)/ Cr (3nm) was thermally deposited for electrodes. The thin layer of Cr is used as a buffer layer for Au electrodes on graphene because Au does not adhere to the surface of graphene alone without Cr. And then, Hall bar geometry of graphene was defined via oxygen plasma etching (figure 30 (c.d)).

Finally, Au nanoparticle (~ 1nm) is deposited by thermal evaporation for enhancement of spin-orbit coupling in graphene. The details for Au coverage will be discussed in next chapter.

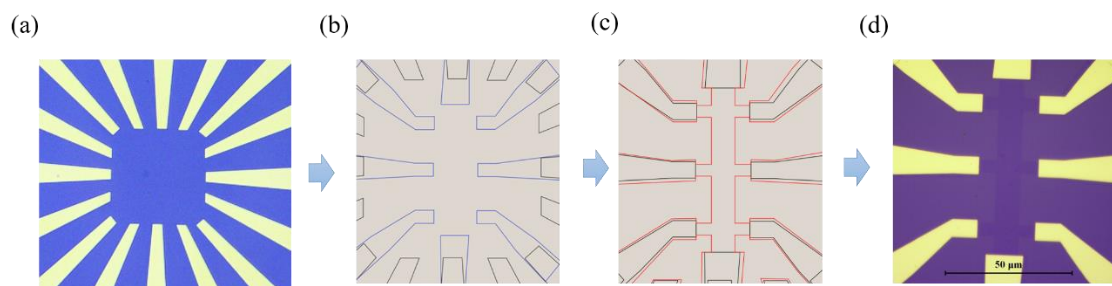

Figure 30. the optical microscopy image of fabrication process and a device design with CAD software. (a) the base substrate in figure 29. (b) the small electrode design by CAD. Au/Cr is deposited between (b) and (c) process. (d) the final device after oxygen plasma etching. In this graphene Hall type device, I measure the field effect transistor properties and nonlocal spin resistance.

4.2 Measurement.

Electrical measurements are performed in a Quantum Design Physical Property Measurement System (PPMS) with the Keithley series. Figure 31 shows the schematic for charge transport and nonlocal spin resistance. First, the graphene devices are characterized for electrical transport. The electrical measurement is performed employing a four-terminal configuration to ignore the contact resistance of electrode. As shown figure 31, the voltage ($V_{xx} = R_{xx}/I$) between additional two leads is detected when charge current (black $\pm$I) is applied widthwise. To measure the Hall effect and magnetoresistance in graphene, magnetic field is applied perpendicular to graphene plane. For nonlocal spin resistance, a charge current through the first leg (red $\pm$I) of the H-bar generate transverse spin current if there is strong spin-orbit coupling, and then the nonlocal voltage ($V_{NL} = R_{NL}/I$) on second leg is detected from the inverse spin Hall effect. The precession of spin current generated from spin Hall effect is confirmed in an applied in-plane magnetic field.

The figure 32 shows the measurement set-up for transport measurement. The indium(In) with copper wire was used for the electrical contacts to Au pads of the device as shown figure 32 (a,b). The samples are loaded to a vacuum chamber of PPMS which can control a variable temperature (2K ~ 400K) and magnetic field (-9T~+9T). The 4-terminal non-local measurements for spin and charge transport are performed by using a Keithley source meter (K2636) and a nano-voltmeter (K2182) as shown in figure 32 (c). The electrical transport properties of the CVD graphene H-bar device is shown in figure 33. The figure 33 (a) indicates the typical field effect property, and figure 33 (b), (c) show quantum Hall effect in graphene.

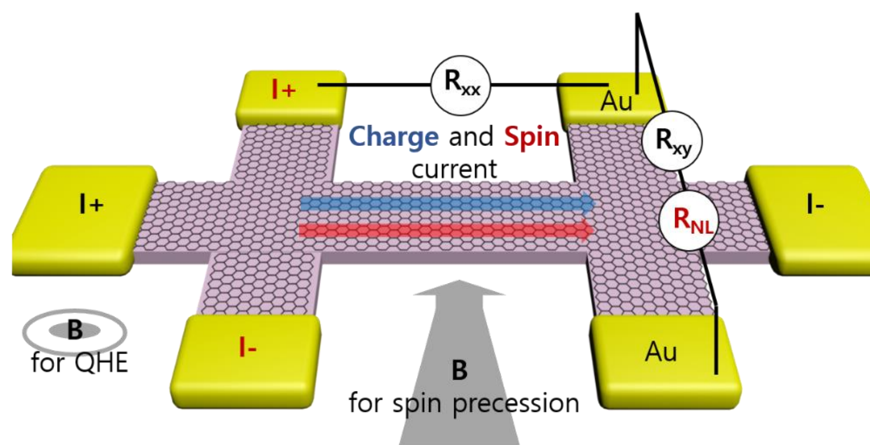

Figure 31. Schematic of the graphene H-bar geometry with 6-terminals for spin and charge transport. In this type, it is possible to measure both graphene field effect properties and spin Hall induced nonlocal resistance. As shown in figure, for quantum Hall effect and quantum interference of graphene, the out of plane magnetic field is applied. For spin precession with spin Hall effect, the in-plane field is applied.

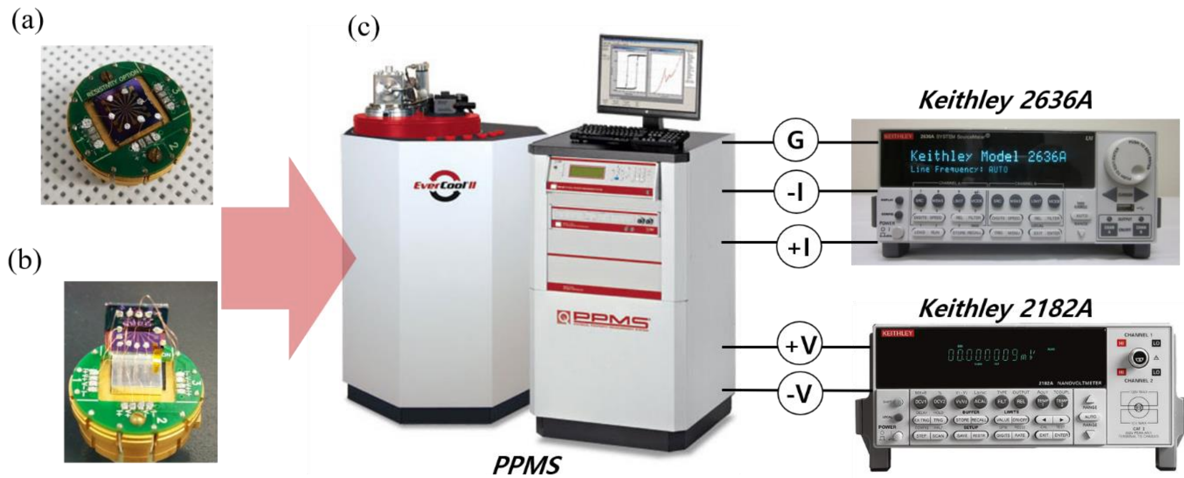

Figure 32. The measurement setup for charge and spin transport. (a) The wiring of graphene H-bar device on sample puck for quantum Hall effect and magnetoresistance. (b) The wiring of graphene H-bar device on sample puck for spin precession from spin Hall effect. (c) The wiring sample is loaded in sample chamber of PPMS. The Ever-Cool system of PPMS serve low temperature (2K~400K) and high magnetic field (-9T~9T). The transport measurements are performed with standard 4-terminal DC techniques by using Keithley series. The Keithley 2636A is the equipment for field effect transistor as source meter. And, the Keithley 2182 is the nano-volt meter for spin current. This nano-volt meter can detect electrical potential up to 10^{-8} V.

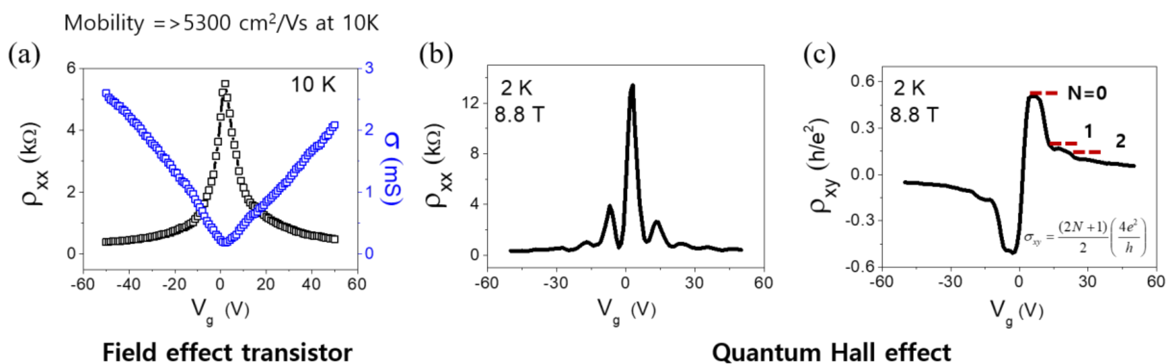

Figure 33. Field effect property and quantum Hall effect in graphene H-bar device. (a) The resistivity as a function of gate voltage at 10K. the mobility is 5300 cm^2/Vs from equation (9). The charge neutral point is around 2V. (b), (c) The resistivity and Hall resistivity as a function of gate voltage with 8.8T at 2K. The quantum Hall effect in CVD graphene is shown by quantized plateau in Hall resistivity with vanishing resistivity in the corresponding gate voltage.

V. Spin Hall induced nonlocal resistance in Au-clustered graphene

Engineering the electron dispersion of graphene to be spin-dependent is crucial for the realization of spin-based logic devices. Enhancing spin-orbit coupling in graphene can induce spin Hall effect, which can be adapted to generate or detect a spin current without a ferromagnet. Recently, both chemically and physically decorated graphenes have shown to exhibit large nonlocal resistance via the spin Hall and its inverse effects. However, these nonlocal transport results have raised critical debates due to the absence of field dependent Hanle curve in subsequent studies. Here, I introduce Au-clusters on graphene to enhance spin-orbit coupling and employ a nonlocal geometry to study the spin Hall induced nonlocal resistance. My results show that the nonlocal resistance highly depends on the applied gate voltage due to various current channels. However, the spin Hall induced nonlocal resistance becomes dominant at a particular carrier concentration, which is further confirmed through Hanle curves. The obtained spin Hall angle is as high as ~ 0.09 at 2 K. Temperature dependence of spin relaxation time is governed by the symmetry of spin-orbit coupling, which also depends on the gate voltage: asymmetric near the charge neutral point and symmetric at high carrier concentration. These results inspire an effective method for generating spin currents in graphene and provide important insights for the spin Hall effect as well as the symmetry of spin scattering in physically decorated graphene.

This chapter is organized as follows: In section 5.1, I introduce a research trend of graphene spin Hall effect. In section 5.2, I describe the details of experimental methods including device fabrication and characterization. In section5.3, I discuss our results starting from the behavior of nonlocal resistance in our Au-clustered graphene and then show how we determined gate-dependent SHE induced nonlocal resistance. I then discuss behavior of magneto-conductivity in Au-clustered graphene, which displays gate dependent variation on the symmetry of spin orbit coupling. Finally, Section 5.6 is for the conclusion and discussion.

5.1 Introduction

Graphene is a two-dimensional honeycomb crystal with an atomic AB site symmetry, which yields a linear dispersion around the K- and K'-points with a chirality for the quasiparticle's "isopin"[3, 10]. The sublattice asymmetry when patching graphene with a hexagonal boron nitride can cause a Berry curvature leading to the separation of isospins via the valley Hall effect[46]. While the isospin quantum number adds another dimension, the manipulation of the real "spin" of an electron in graphene remains as a frontier of spintronics[40, 50, 53]. A mandatory requirement for exploiting electron spins in graphene is the facile control of spin-orbit coupling (SOC). Instilling spin-orbit coupling into graphene allows splitting and detecting electron spins *via* the spin Hall effect (SHE) and its inverse effect[71, 92]. In addition,

ULSAN NATIONAL INSTITUTE OF SCIENCE AND TECHNOLOGY

spin-orbit coupling arisen from broken inversion symmetry, *i.e.,* Rashba spin-orbit coupling allows a gate controllable spin precession[54, 98]. The original Datta-Das concept of the spin-field-effect transistor (spin-FET) can be achieved only through a channel with an exceptionally long mean free path[99-101]. Developing practical methods for enhancing spin-orbit coupling in graphene will make it to be an ideal material at the forefront of spintronics. Thus far, several methods have been explored to enhance spin-orbit coupling in graphene. For example, chemisorbed hydrogen and fluorine atoms in graphene have been predicted to induce strong spin-orbit coupling (~ 10 meV) through the distortion of its planar structure via sp^3 hybridization[102-103]. Further, theoretical calculations determined that physically decorated adatoms in graphene could also induce strong spin-orbit coupling without breaking sp^2 hybridization and the sublattice symmetry[104-105]. In particular, Au intercalation at the graphene/Ni interface can cause a giant spin-orbit splitting as large as ~ 100 meV near the Dirac point[106]. Recently, Balakrishnan *et al.* reported SHE induced nonlocal resistances ($R_{NL}^{SHE}s$) in hydrogenated, CVD, and physically decorated graphene in sequence[92, 94]. They showed a large symmetric $R_{NL}^{SHE}s$ peak near the charge neutral peak, which displayed field dependent precession signature (*i.e.,* a Hanle curve). The appearance of large R_{NL} peak itself often was attributed to the presence of spin Hall effect in graphene[107]. However, these nonlocal transport results have raised critical debates[95-96, 108]. Wang *et al.* reported that large nonlocal resistances (R_{NL}s) were observed in Au- or Ir-decorated graphenes, but no evidence of Hanle signature was detected[96]. Kaverzin *et al.* also reported the absence of the field-induced effect in R_{NL} for hydrogenated graphene and questioned the origin of previously reported $R_{NL}^{SHE}s$[95]. Further, a recent theoretical study showed the presence of a large R_{NL} in Au-decorated graphene even in the absence of spin-orbit coupling[109]. They also reported that the spin Hall angle (θ_{SH}) in Au-clustered graphene can significantly fluctuate according to the applied gate voltage[109].

Here, I report gate dependent $R_{NL}^{SHE}s$ in Au-clustered graphene. A Hall-bar like (H-bar) geometry is employed to generate a transverse spin-polarized current via the SHE, which in turn can be detected owing to the inverse spin Hall effect. A significant gate-dependent fluctuation in R_{NL} is observed at low temperature. However, R_{NL}^{SHE} become dominant at a particular carrier concentration, where the Hanle curves are consistently observed at various temperatures. The temperature dependence of the spin relaxation time (τ_s) suggests that the Elliot-Yafet (EY) mechanism prevails at that specific carrier concentration. Further study on magneto-conductance (MC) reveals that asymmetric spin-orbit scattering (SOS) prevails near the charge neutral point, while symmetric spin-orbit scattering dominates at a higher carrier concentration. These results provide an alternative approach for effective spin-charge conversion in graphene and important insights for R_{NL}^{SHE} as well as the symmetry of spin-orbit scattering therein.

5.2 Experimental methods

Graphene used for our device was grown on a polycrystalline Cu foil using a chemical vapor deposition method demonstrated elsewhere[97]. A 25 μm copper foil (Alfa Aesar, 99.8% purity) was electropolished in phosphoric acid for 15 min and rinsed with distilled water and isopropyl alcohol (IPA). The copper foil was loaded into a quartz tube 3-zone furnace and the temperature was increased to 1050 °C in the H_2 environment for the removal of native oxides in the copper with the surface reconstruction. Graphene was synthesized by introducing CH_4 gas and H_2 gas with a ratio of 10:5 (sccm) for 15 min, and transferred onto the SiO_2 (300 nm)/*p*-Si subatrate using a polymethyl methacrylate (PMMA) wet transfer process. Then, the sample was annealed in high vacuum at 300 °C in order to remove possible resist residues. The devices were fabricated by employing the electron beam lithography. Thermally deposited Au (60 nm)/Cr (3 nm) layers were used for electrodes. A Hall bar geometry of the nonlocal graphene device was defined by using the oxygen plasma etching. For enhancement of spin-orbit coupling (see figure 34), an ultrathin Au layer (~ 1 nm) was deposited by the thermal evaporation. Prior to the measurements, the fabricated devices were annealed in N_2/H_2 gas at 300 °C to remove residual resists. Electrical measurements were performed in a Quantum Design Physical Property Measurement System (PPMS). Indium with a copper wire was used for the electrical contacts to Au pads of the device. The 4-terminal nonlocal measurements were performed by using a Keithley source meter (K2636) and a Nano-voltmeter (K2182). Gate voltage was applied through the contact to the bottom of SiO_2 (300 nm)/*p*-Si substrate. XPS was performed by employing a Thermo Scientific spectrometer (K-Alpha) with a monochromatic Al Kα X-ray source (1486.6 eV). The spot size of the incident x-ray was 400 μm diameter. Alpha 300R spectrometer (WITec) with a 532 nm laser source was used for the Raman spectroscopy.

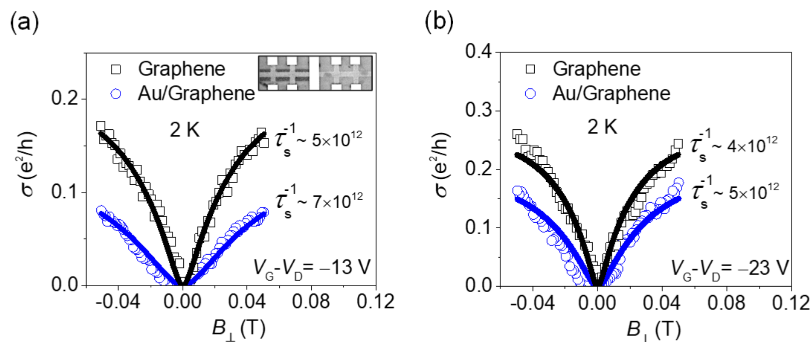

Figure 34. The enhancement of SOC in Au-clustered graphene. (a) Magneto-conductance measured for both CVD graphene and Au-clustered CVD graphene at n = 0.93×10^{12} cm^{-2} (V_G -V_D = –13 V). Solid lines are fits of equation (33) to the measured data displaying the increased spin-orbit scattering rate (τ_s^{-1}) by the Au patch. The inset shows SEM image of fabricated device with 1 μm width of the Hall bar line. (b) Magneto-conductance measured for both CVD graphene and Au-clustered CVD graphene at 1.65x10^{12} cm^{-2} (V_G -V_D = –23 V).

ULSAN NATIONAL INSTITUTE OF
SCIENCE AND TECHNOLOGY

5.3 Local and non-local electric transport

Figure 35 (a) shows a schematic of the nonlocal graphene device in order to study R_{NL}^{SHE}. In the presence of spin orbit coupling, a charge current flowing across the vertical line of the H bar generates a transverse spin current through the central channel line via the direct SHE. If the spin current persists through the channel, it can produce the nonlocal voltage via the inverse spin Hall effect. In fact, I have studied this non-local geometry device for a series of CVD, Au-decorated (0.05-0.2 nm deposition of Au), and Au-clustered graphene (1 nm deposition of Au) in order to investigate R_{NL}^{SHE} as shown in figure 37. All devices displayed large R_{NL} signal. However, other than Au-clustered graphene, I was not able to detect field-dependent Hanle curve, similar to the reports in reference [95-96, 108]. Thus, I discuss results only from the Au-clustered graphene device in this report. Figure 35(b) displays a scanning electron microscopy (SEM) image of the fabricated Au-clustered graphene device A with a channel width (w) of 1 μm and lengths (Ls) of 2, 3, and 4 μm. The thermally deposited ultrathin Au layer (~ 1 nm) formed randomly distributed Au clusters with typical size of the order of 10 nm as shown in enlarged figure of 35(b). The determined Au coverage based on SEM image is ~ 41.92% as shown in figure 37 (a). CVD graphene used in our device was a monolayer as confirmed by its Raman spectrum. XPS result showed that Au atoms did not form chemical bonds with the carbon atoms of graphene as shown in figure 36. Figure 35(c) displays ambipolar field-effect behavior at 300 K using back-gate. The upper x-axis displays the estimated carrier concentration. This FET characteristic is nearly similar to that observed in a typical graphene FET indicating that charge carriers mainly transport through the graphene layer. The gate voltage of the maximum resistivity, a charge neutral point, is located at around 5 V. The estimated mobility at the neutral point is 1000 cm^2 / V·s at 300 K. The rounding of a maximum resistivity region and the decrease in mobility of the Au-clustered graphene compared to that of the as-grown CVD graphene imply that the Au clusters introduces considerable charged impurity scatterings[110]. Typical resistivities of Au-clustered graphene devices near the charge neutral point were ~ 5 kΩ with slight sample to sample variation. These resistivity values were nearly similar to that of our as-grown CVD graphene. Both ambipolar field-effect behavior and the estimated resistivity suggest the charge carriers in our Au-clustered graphene devices mainly transport through the graphene.

Figure 35(d) displays a gate-dependent R_{NL} measured at 300 K for L/w = 2, 3, and 4 channels of the device A. Similar to the local FET curve, R_{NL} for all channels of the device A displayed maximum value near the charge neutral point. The dashed line in Figure 35(c) is the simulated nonlocal Ohmic resistance (R_{NL}^{Ohm}), which is given as $R_{NL}^{Ohm} = \rho \exp(-\pi L/w)$, where ρ is the resistivity of the material[111]. The observed R_{NL} for all channels (L/w =2, 3, and 4) were much higher than the R_{NL}^{Ohm}. Similar to previous reports[95-96], this unidentified large R_{NL} does not display an in-plane field-dependent spin precession signature.

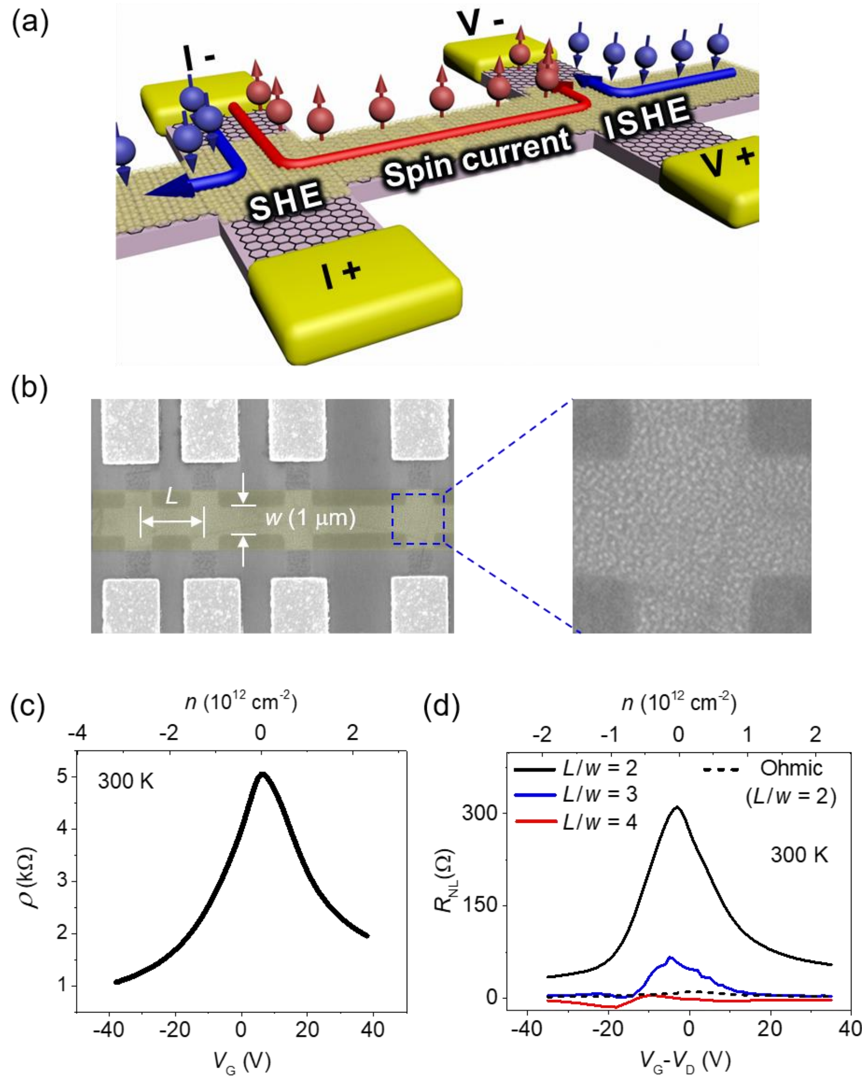

Figure 35. Nonlocal device geometry and R_{NL} measured for the device A. (a) Schematic of the H-bar geometry of the graphene device. (b) A SEM image of a graphene H-bar device. Randomly distributed Au clusters can be observed on enlarged figure at the right panel. The determined Au coverage based on SEM image is ~ 41.92%. (c) Gate-dependent local resistance of the Au-clustered device A displaying ambipolar field effect behavior. (d) R_{NL} as a function of applied gate voltage for different L/w ratios of the device A at 300 K.

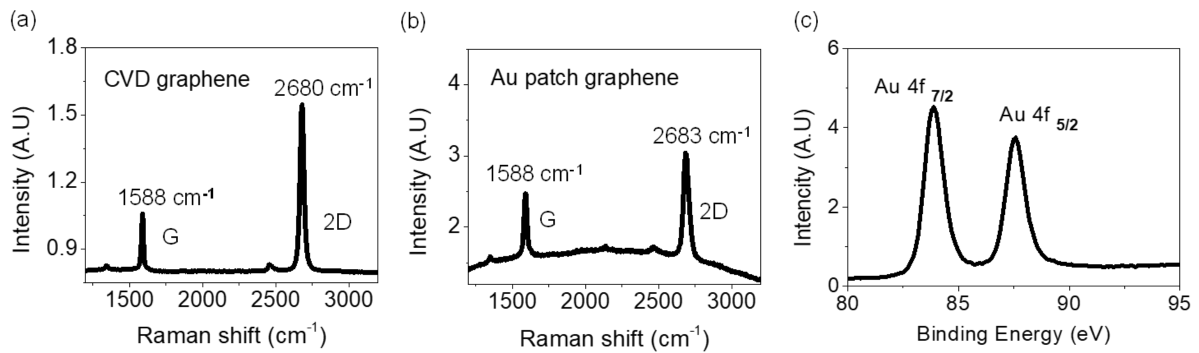

Figure 36. (a) Raman spectra of CVD graphene. Dominance of the 2D peak over the G peak was observed, suggesting the studied CVD graphene was mainly a single layer. (b) Raman spectra of Au-patched CVD graphene. The G peak of Au-patched graphene did not shift, but the 2D peak was shifted by 3 cm^{-1} (blue shift). Results show that Au patch does not form chemical bonding (*e.g, sp*^{3}-type) with the carbon atoms of graphene. A slight shift of the 2D peak suggests a partial strain is applied on the graphene layer due to the top Au patch. (c) XPS result of Au-clustered graphene. The observed spectrum exhibited unoxidized Au atoms.

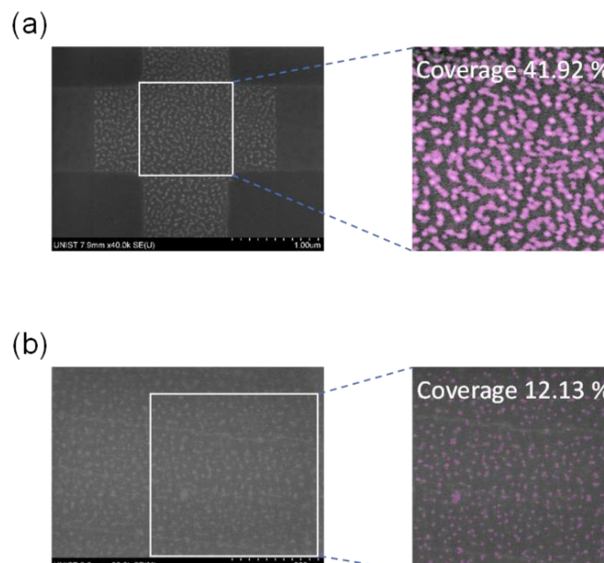

Figure 37. (a) SEM image of Au-clustered graphene (1 nm deposition). Right panel shows Au coverage of 41.92%. (b) SEM image of Au-clustered graphene (0.2 nm deposition). Right panel shows Au coverage of 12.13%.

In general, R_{NL} in the H-bar geometry of a graphene device can arise from various mechanisms. The total R_{NL} can be expressed as $R_{NL} = R_{NL}^{SHE} + R_{NL}^{Ohm} + R_{NL}^{Zeeman} + R_{NL}^{Valley} + R_{NL}^{Thermal} + R_{NL}^{Ballistic} + \cdots$

Here, R_{NL}^{Ohm} can be significantly reduced as long as $L/w \geq 3$. In the presence of a perpendicular magnetic field, Zeeman splitting separates electron and hole with opposite spins near the Dirac point leading to giant R_{NL}^{Zeeman} [112]. The valley Hall effect due to global AB asymmetry can produce R_{NL}^{Valley} [46]. $R_{NL}^{Ballistic}$ can produce negative resistance in the ballistic limit, *i.e.,* $\lambda_e >> w$ (where λ_e is the electron mean free path)[111]. The estimated λ_e values of our devices were typically less than 100 nm. Nonetheless, theoretical and experimental studies suggested that the nonlocal resistance could produce negative signal even in the quasi-ballistic limit of $\lambda_e < w$[109, 111]. Thus, the relevant contributions in our experiment are R_{NL}^{SHE}, $R_{NL}^{Ballistic}$, $R_{NL}^{Thermal}$, and other non-intuitive channels. Especially, the observed large positive R_{NL} in L/w = 2 and 3 might be associated with unidentified channels, as suggested in previous experimental reports[95]. Suppression of this non-intuitive R_{NL} as well as $R_{NL}^{Ballistic}$ could be achieved by increasing L/w.

To strongly suppress the unidentified nonlocal signal, we further increased L/w. Figure 39 (a) displays the local FET characteristics measured for the Au-clustered device B, which has L/w = 5.6. The inset in Figure 39 (a) displays a SEM image of the device B. The charge neutral point for the device B is located at around 33 V. The estimated mobility near the neutral point is ~ 1000 cm^2 / V·s at 300 K. Figure 39 (b) displays the gate-dependent R_{NL} measured at 300 K. The maximum positive R_{NL} is located near the Dirac region. The blue line in Figure 39 (b) indicates the simulated R_{NL}^{Ohmic}. Note that the previously reported R_{NL}^{SHE} exhibited a large symmetry peak around the Dirac point[92, 94]. However, the observed R_{NL} in our device displays something similar to the derivative of the FET peak near the Dirac point. The current in local probes introduces joule heating and temperature gradient along the central channel line. Then, the thermoelectric voltage given by Seebeck coefficient can induce offset voltage in nonlocal probes as shown in figure 38. Because the Seebeck coefficient has opposite sign for electron and hole majority carriers, it changes sign near the charge neutral point, so does the subsequent offset voltage in nonlocal probes[113]. This thermoelectric offset voltage is proportional to I^2. Thus, the nonlocal *I-V* curves originated from such a thermal effect should display quadratic behavior. R_{NL}s of the device B as lowering temperature are displayed in Figure 39 (c). A significant fluctuation in R_{NL} can be observed. And this fluctuation become stronger with lowering temperature. We note that recent theoretical simulation of θ_{SH} in graphene with Au adatoms and/or clusters also showed a gate dependent fluctuation[109]. In general, conductance fluctuations in graphene can also occur at low temperature due to the quantum interference of carriers, which is largest near the Dirac point due to the presence of random electron and hole puddles[114-115]. The quantum interference of spins in graphene can also induce a large gate-dependent fluctuation[116]. Because conductance fluctuations are dependent on variations in Fermi energy, gate-dependent R_{NL}s, especially at 2 K and 5 K (Figure 39 (b)) display

similar fluctuation pattern. Thus, the observed gate dependent fluctuation in R_{NL} is likely associated with the fluctuation in both θ_{SH} and conductance fluctuation. In short, the observed gate-dependent R_{NL} could be a consequence of entangled $R_{NL}^{Thermal}$, R_{NL}^{SHE}, and conductance fluctuations.

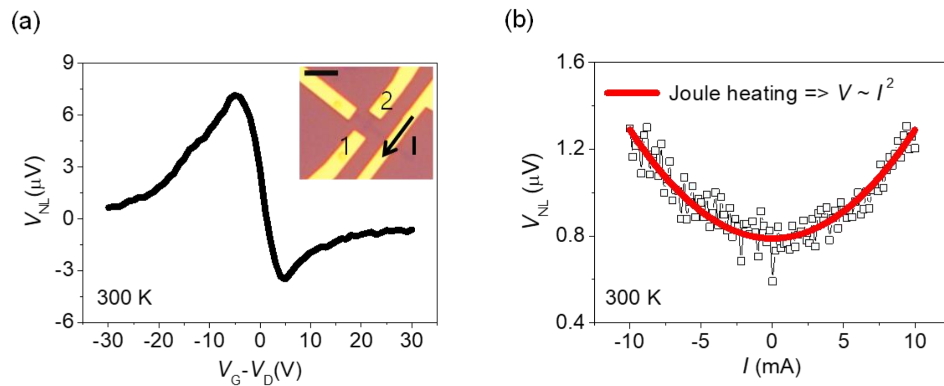

Figure 38. Characteristic nonlocal voltage induced by the thermoelectric effect. (a) The nonlocal voltage induced by a heat gradient due to a joule heating. The inset is an optical microscopy image (scale bar, 5 μm) of the graphene device. The charge current through the Au electrode functions as a heat source. The generated heat gradient along the graphene channel produced a thermoelectric voltage due to the Seebeck effect. The offset of a thermoelectric voltage can be loaded on the nonlocal probes, which changes its sign depending on the charge of majority carriers. (b) Nonlocal voltage as a function of applied current. The plot displays that the measured nonlocal voltage was proportional to the joule heating power ($\sim I^2$).

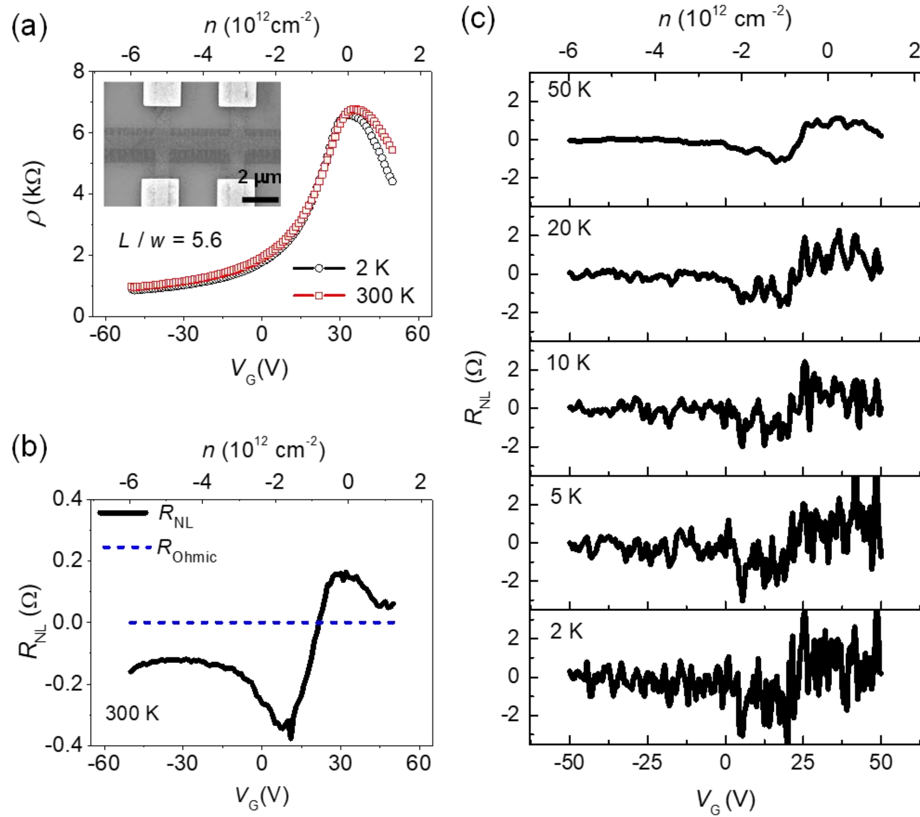

Figure 39. The local and nonlocal resistance of the Au-clustered graphene device B at various temperatures. (a) Local resistance as a function of applied gate voltage for the Au-clustered device B at T = 2 and 300 K. The Dirac point is located at around 33 V. The inset displays a SEM image of the device B, which has L/w = 5.6. (b) R_{NL} *vs*. V_G of the device B at 300 K. The blue dashed line indicates the calculated R_{NL}^{Ohmic}. (c) R_{NL} *vs*. V_G of the device B at 2, 5, 10, 20, and 50 K.

ULSAN NATIONAL INSTITUTE OF SCIENCE AND TECHNOLOGY

5.4 Gate-dependent spin Hall effect.

An effective method to determine R_{NL}^{SHE} is to examine the spin precession signature. Here, the SHE induces a spin current along the bridging channel with a polarization perpendicular to the plane. Thus, the in-plane magnetic field causes the Larmor precession of carriers' spins[40, 92]. This nonmonotonic oscillatory signal can be fitted with[93]

$$R_{NL} = \frac{1}{2}\gamma^2 \rho W Re\left[\left(\sqrt{1+i\omega_B\tau_s}/\lambda_s\right)e^{-\left(\sqrt{1+i\omega_B\tau_s}/\lambda_s\right)|L|}\right] \tag{58}$$

where θ_{SH} is the spin hall angle, τ_s is the spin relaxation time, λ_s is the spin relaxation length. $\omega_B = \Gamma B_{//}$ is the Larmor frequency, Γ is the gyromagnetic ratio and $B_{//}$ is the applied in-plane magnetic field. The in-plane field-dependent R_{NL} for various gate voltages at 2 K is displayed in Figure 40 (a)-(d). The insets in Figure 40 (a)-(d) show the nonlocal *I-V* curve for each applied gate voltage. Among the various gate voltages, only at $V_G-V_D = -33$ V, $R_{NL}(B_{//})$ exhibits a precession signature similar to that given by equation (58). In addition, the nonlocal *I-V* curve only at $V_G-V_D = -33$ V exhibits monotonic linear behavior as predicted in R_{NL}^{SHE}. The behaviors of the nonlocal *I-V* curves at different gate voltages can be interpreted as a combination of the nonlocal signal from various fluctuations and from the thermal effect (~ I^2). Thus, it can be inferred that R_{NL}^{SHE} is dominant at a particular bias of $V_G-V_D = -33$ V. And the field dependent R_{NL} at $V_G-V_D = -33$ V can be fitted well with equation (58). The observed gate voltage dependent fluctuation of nonlocal resistance (R_{NL}) and dominance of spin Hall effect driven R_{NL} (R_{NL}^{SHE}) at a particular gate voltage (Fermi level) should be further confirmed with many samples. we show the reproducibility of the gate voltage dependent dominance of R_{NL}^{SHE} in other devices. As discussed in the manuscript, the behavior of $R_{NL}(B_{//})$ curve strongly depends on the doping level for the studied Au-patched graphene devices. Figure 41 (a)-(d) displays $R_{NL}(B_{//})$ at 3 K measured at various gate voltages for the channel of $L/w = 4$ in the device A (introduced in main text). Figure 41 (e)-(h) displays $R_{NL}(B_{//})$ at 3 K measured at various gate voltages for the channel of $L/w = 4$ in the device C, which has the same geometry as the device A. Both devices display spin precession signature at a particular gate voltage ($V_G-V_D = -17$ V for the device A and $V_G-V_D = -21$ V for the device C). In particular, slight variations in the gate voltage (~ 1 V) are enough to suppress the Hanle signature. The absence of Hanle curve near the charge neutral point and it appearance at a particular gate voltage could be attributed to following reasons. First, the fluctuation of nonlocal resistance could overcast R_{NL}^{SHE} and Hanle signal. Second, the θ_{SH} and thus R_{NL}^{SHE} could themselves have significant gate-dependent fluctuation. I note that the Fermi level dependence of the SHE was also found in

other Dirac fermionic systems[117]. In order to confirm whether R_{NL} at a particular gate bias ($V_G{-}V_D$ = −33 V) originates from R_{NL}^{SHE}, we further examined field-dependent R_{NL} at various temperature.

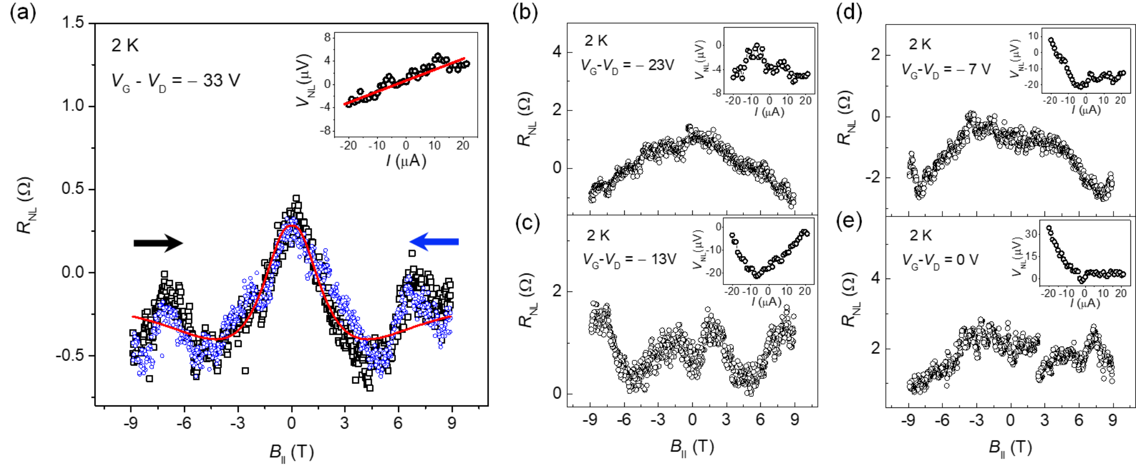

Figure 40. Gate voltage dependence of R_{NL} *vs.* $B_{//}$ curves measured for the device B. (a) R_{NL} *vs.* $B_{//}$ of the device B at T = 2K measured at $V_G{-}V_D$ = −33 V. The red line is a fitting curve with Eq. (1). Black and blue symbols are data measured during negative-to-positive and positive-to-negative field scan, respectively. The inset displays nonlocal *I-V* curves. The red line in the inset is a linear fit. (b-e) R_{NL} *vs.* $B_{//}$ of the device B at T = 2K measured at various $V_G{-}V_D$ = −23, −13, −7, and 0 V. The insets display nonlocal *I-V* curves measured at various applied gate voltages.

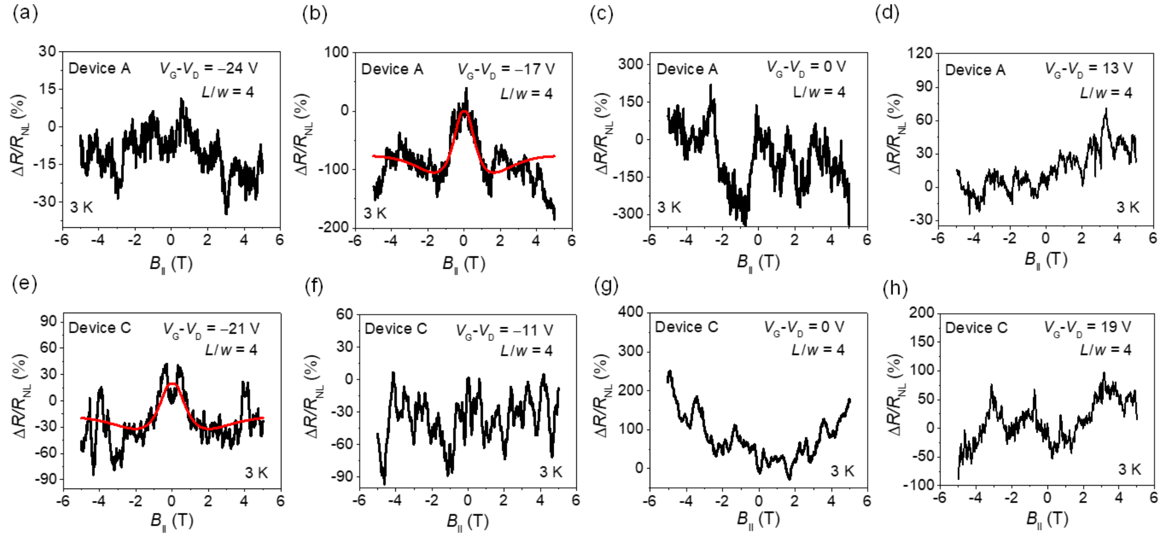

Figure 41. R_{NL} as a function of in-plane magnetic field measured at various gate voltage and at T = 3K. (a)-(d) R_{NL} measured for the channel of L/w = 4 in the device A. (e)-(f) R_{NL} measured for the channel of L/w = 4 in the device C.

ULSAN NATIONAL INSTITUTE OF SCIENCE AND TECHNOLOGY

Figure 42 (a) shows $R_{NL}(B_{//})$ measured at temperatures T = 2, 5, 10, 20, and 50 K. All curves exhibit oscillatory signatures with increasing width as the temperature is increased. For the conventional Hanle curve, the width of the curve approximately corresponds to the spin scattering rate (τ_s^{-1}). The broadening of the width with increasing temperature is likely associated with reduced τ_s at higher temperatures. Thus, the observed $R_{NL}(B_{//})$ at various temperatures is consistent with the behavior of R_{NL}^{SHE}. The red lines in Figure 42 (a) are fits of equation (58) to the measured data. At 2 K, the estimated parameters are θ_{SH} ~ 8.8%, τ_s ~ 10 ps, and λ_s ~ 2.2 μm. Figure 42 (b) displays the temperature dependence of the extracted parameters ΔR_{NL}, θ_{SH}, and λ_s obtained by fitting with equation (58). All parameters exhibit general trend of reduction with increasing temperature. One might suspect that the observed R_{NL}^{SHE} and its field dependence is originated from the Au bypass. However, the spin in Au could not transport over 5.6 μm and the observed FET characteristics clearly support that the charge carriers mainly transport through the graphene. I note that this temperature-dependent broadening of the precession signature at a particular gate voltage is consistently observed in our Au-clustered graphene devices as shown in figure 43. The appearances of Hanle curve in other devices also accompany with the linear *I-V* curve at the same gate bias. Figure 42 (c) displays the temperature dependence of τ_s^{-1}, which exhibits a nonlinear increase with temperature. Conversely, τ_p obtained from the FET results is nearly independent of temperature, as shown in Figure 42 (c). This implies that the charged impurities in our studied sample introduce considerable Coulomb scattering, which prevails over phonon scattering even at relatively high temperature[118]. In contrast to τ_p, τ_s in graphene is expected to have a strong temperature dependence. The two main processes attributed to the spin relaxation in graphene are D'yakonov-Perel' (DP)[52] and EY[51] mechanisms. Within the DP mechanism originated from a broken inversion symmetry, τ_s^{-1} is inversely proportional to τ_p^{-1} and proportional to T^3, leading to the relation[18]

$$\frac{1}{\tau_{DP}} = Q\left(\frac{4R}{\sqrt{3-R}}\frac{m^*}{m_0}\right)^2 \frac{(k_B T)^3}{\hbar^2 E_g}\tau_m \tag{32}$$

For the EY mechanism, τ_s^{-1} is directly proportional to τ_p^{-1} and T^2, as given by[18]

$$\frac{1}{\tau_{EY}} = A\left(\frac{k_b T}{E_g}\right)^2 R^2 \left(\frac{1-R/2}{1-R/3}\right)^2 \frac{1}{\tau_m} \tag{31}$$

If τ_p is independent of temperature, then τ_s^{-1} of either the DP or EY mechanism should be proportional to T^3 or T^2, respectively. My results show that τ_s^{-1} is proportional to T^2, indicating that EY spin relaxation prevails over DP spin relaxation. This results thus suggest that the observed R_{NL}^{SHE} in our device is likely

ULSAN NATIONAL INSTITUTE OF SCIENCE AND TECHNOLOGY

induced by the spin charge conversion from the extrinsic spin Hall effect. When EY spin relaxation is dominant, the strength of spin-orbit coupling can be inferred from [119-120]

$$\Delta_{SOC} = \varepsilon_F \sqrt{\tau_p/\tau_s} \qquad (59)$$

where ε_F is the Fermi energy given by $\varepsilon_F = \hbar v_F k_F = \hbar v_F \sqrt{\pi n}$.

At $V_G - V_D = -33$ V ($n = 2.37\times10^{12}$ cm^{-2}), $\Delta_{SOC} \approx 9.0$ meV. The spin diffusion coefficient $D_s = \lambda_s^2/\tau_s$ is estimated to be ~ 0.5 m^2·s^{-1} at 2 K and this value is about 10 times larger than $D_c = v_F^2 \tau_p$. We note that this inequality of $D_s \neq D_c$ is often found in low-dimensional systems[121].

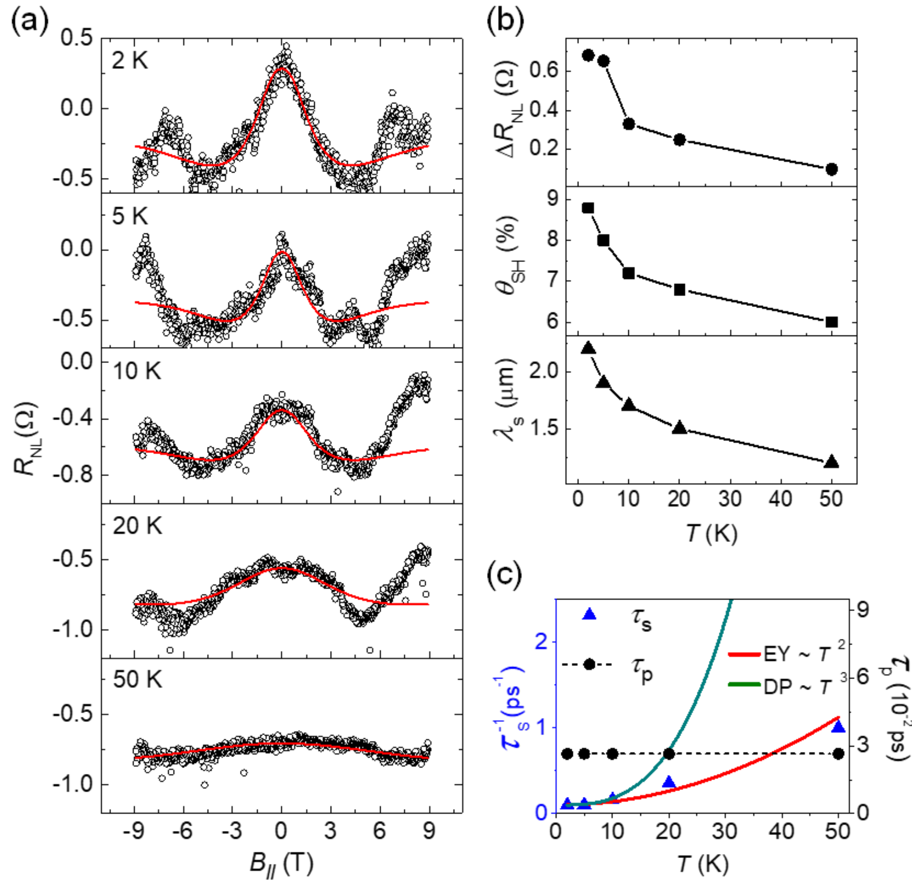

Figure 42. Temperature dependence of $R_{NL}(B_{//})$ and τ_s measured for the device B. (a) R_{NL} *vs.* $B_{//}$ of the device B measured at $V_g - V_D = -33$ V for various temperatures (2, 5, 10, 20, and 50 K). The red lines are fits of Eq. (1) to the measured R_{NL}s. (b) Temperature dependence of the parameters extracted from fitting with Eq. (1). ΔR_{NL}, θ_{SH}, and λ_s are displayed from top to bottom. (c) Temperature dependence of τ_s^{-1} (▲) and τ_p (●). The green and the red line are the predicted temperature dependences for DP and EY spin relaxation mechanisms, respectively.

ULSAN NATIONAL INSTITUTE OF
SCIENCE AND TECHNOLOGY

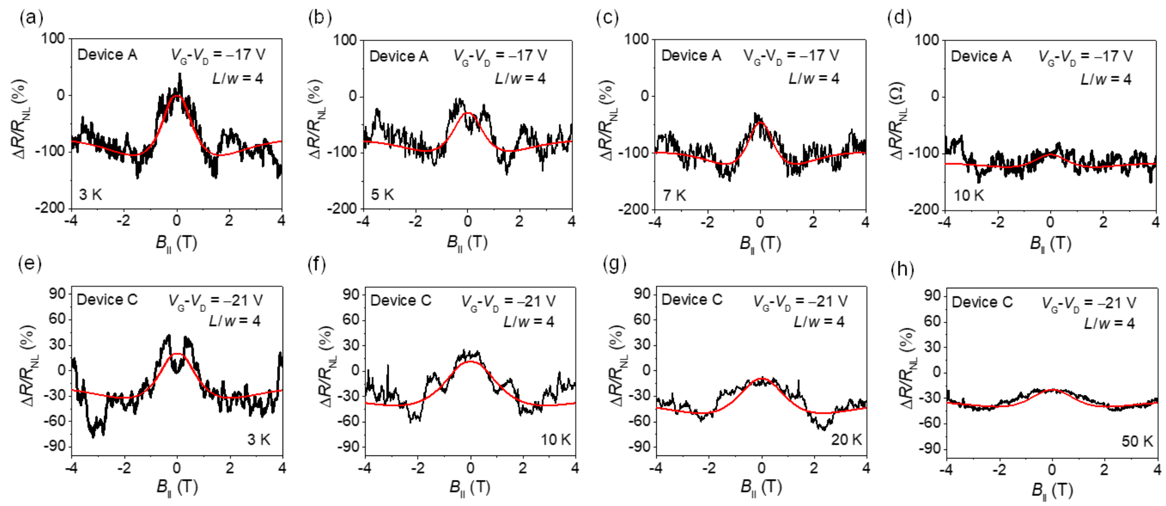

Figure 43. R_{NL} as a function of in-plane magnetic field measured at various temperatures. (a)-(d) R_{NL} measured at V_G-V_D = - 17 V for the channel of L/w = 4 in the device A. (e)-(f) R_{NL} measured at V_G-V_D = - 21 V for the channel of L/w = 4 in the device C.

5.5 Symmetry spin-orbit scattering

The spin relaxation mechanisms can be further studied through the quantum interference effect on the diffusive transport[56, 122-123]. The presence of spin-orbit coupling affects the phase coherence of electrons, leading to reduced weak localization (WL) or even weak anti-localization (WAL). A recent theoretical study showed that the symmetry of spin-orbit coupling in graphene can also be inferred from magneto-conductivity[122]. Here, we further investigate the symmetry of spin-orbit coupling in Au-clustered graphene. According to Ref 122, asymmetric spin-orbit coupling causes DP spin relaxation and symmetric spin-orbit coupling induces EY spin relaxation, which leads to the following expression for magneto-conductivity.

$$\Delta\sigma(B) = -\frac{e^2}{2\pi h}\left[F\left(\frac{B_z}{B_\varphi}\right) - F\left(\frac{B_z}{B_\varphi + B_{asy}}\right) - 2F\left(\frac{B_z}{B_\varphi + B_{SO}}\right)\right] \quad (33)$$

$$F(\mathrm{z}) = \ln z + \psi\left(\frac{1}{2} + \frac{1}{z}\right), \qquad B_{\varphi,SO} = \frac{\hbar c}{4De}\tau_{\varphi,SO}^{-1}, \qquad B_{asy} = \frac{\hbar c}{2De}\tau_{asy}^{-1}, \qquad \tau_{SO}^{-1} = \tau_{sym}^{-1} + \tau_{asy}^{-1}$$

where ψ is the digamma function, $\hbar$ is the Planck constant, τ_φ^{-1} is the inelastic de-phasing, and τ_{asy}^{-1} is the SOS rate associated with asymmetric spin-orbit coupling. τ_s^{-1} is the total spin-orbit scattering rate, and thus, $\tau_s^{-1} = \tau_{asy}^{-1} + \tau_{sy}^{-1}$ (where τ_{sy}^{-1} is the symmetric spin-orbit scattering rate). The solid lines in Figure 44 (a) are the fits of Equation (33) to the measured MCs of the device B. Similar to previous reports[30], the estimated phase coherence time is in order of 10^{-12} s, which gradually increased as the carrier concentration was increased. Near the charge neutral point ($V_G - V_D = 0$ V), estimated τ_{asy}^{-1} and τ_{sy}^{-1} were 7×10^{12} and 1×10^{12} s^{-1}, respectively. In contrast, estimated τ_{asy}^{-1} and τ_{sy}^{-1} at $V_G - V_D = -33$ V were 5×10^{11} and 3×10^{12} s^{-1}, respectively. Thus, asymmetric spin-orbit scattering prevails near the charge neutral point, which is gradually reduced as the concentration is increased. At $V_G - V_D = -33$ V, the ratio of $\tau_{sy}^{-1} / \tau_s^{-1}$ was ~85% (Figure 44(b)). This dominance of symmetric spin-orbit scattering leads to EY spin relaxation rather than DP spin relaxation at higher carrier concentrations. This result is consistent with the spin relaxation mechanism deduced from the temperature-dependent behavior of the measured R_{NL}^{SHE}. Here, the estimated τ_s using weak localization and weak antilocalization theory is much shorter than that obtained from non-local measurements. I note that the estimation of τ_s using weak localization and weak antilocalization theory typically produces reduced lifetime by one order of magnitude as studied elsewhere[56].

ULSAN NATIONAL INSTITUTE OF
SCIENCE AND TECHNOLOGY

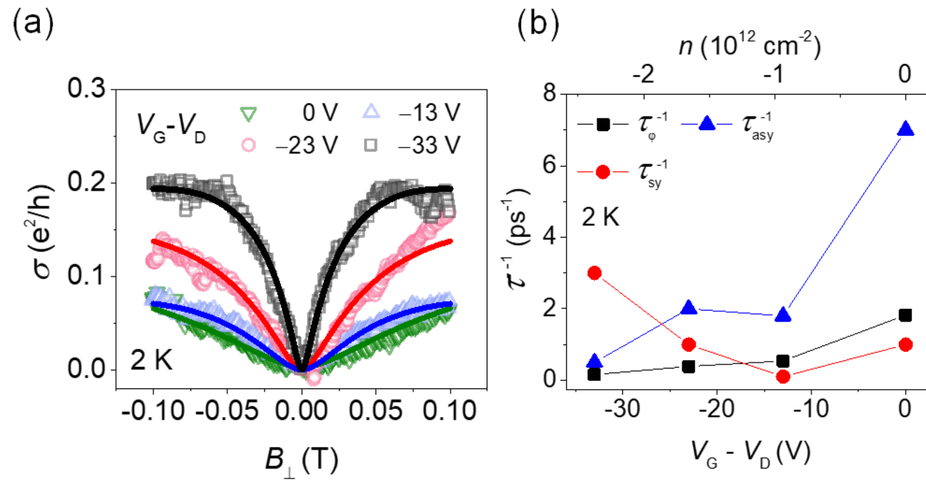

Figure 44. Gate voltage dependence of MC and the symmetry of the SOS rate. (a) The MC of the Au-clustered graphene device at 2 K measured for various gate voltages ($V_G - V_D = -33, -23, -13$, and 0 V). All curves display a WL behavior. The solid lines are fits of Eq. (2) to the measured data. (b) Gate dependence of the extracted τ_φ^{-1}, τ_{sy}^{-1}, and τ_{asy}^{-1}.

ULSAN NATIONAL INSTITUTE OF
SCIENCE AND TECHNOLOGY

5.6 Summary and discussion.

In conclusion, I showed the generation of a spin current by the spin Hall effect and the spin detection by the inverse spin Hall effect in Au-clustered graphene hall bar device. The observed non-local resistance exhibits significant fluctuation with applied gate voltage, which is likely due to in part conductance fluctuation and spin Hall angle fluctuation. The dominance of spin Hall effect induced nonlocal resistance was observed at particular carrier concentration, which was further confirmed through the Hanle curve and its temperature dependence. The behavior of $\tau_s(T)$ obtained from Hanle curves is consistent with the determined spin-orbit coupling symmetry, which is asymmetric near the Dirac point and symmetric at higher concentrations.

Here, the reason why the spin Hall effect appear at particular charge density in this Au-clustered graphene can be inferred from following papers[109, 124-125].

Dink Van Tuan and coworker theoretically reported that the mixing between spin and pseudospin-related Berry's phases results in fast spin dephasing with increasing relaxation times away from Dirac point in adatom-decorated graphene[124]. According to their paper, the presence of non-magnetic adatoms randomly adsorbed on the graphene sheet (in figure 45 (a)) introduces additional spin-orbit coupling terms defined as[124]

$$H = -\gamma_0 \sum_{<ij>} c_i^{\dagger} c_i + \frac{2i}{\sqrt{3}} V_{\mathrm{I}} \sum_{\ll ij \gg \in R} c_i^{\dagger} \vec{s} \cdot (\vec{d}_{kj} \times \vec{d}_{ik}) c_j$$

$$+ iV_R \sum_{<ij>\in R} c_i^{\dagger} \vec{z} \cdot (\vec{s} \times \vec{d}_{ij}) c_j - \mu \sum_{i \in R} c_i^{\dagger} c_i \quad (60)$$

where γ_0 is hopping parameter with 2.7 eV, $c_i^{\dagger}$ and c_i indicate the annihilation and creation operators of one electron at site i, respectively, $\vec{d}_{kj}$ and $\vec{d}_{ik}$ are the unit vectors along the two bonds connecting second neighbors, $\vec{s}$ is the Pauli matrices, V_{I} is the intrinsic spin-orbit coupling strength, and V_{R} is Rashba spin-orbit coupling. The first term of equation (60) indicates the nearest neighbor hopping term. The second term is the complex next-nearest-neighbor hopping term which represents the intrinsic spin-orbit coupling induced by adatoms. The third term describes the Rashba spin-orbit coupling with z-asymmetry normal to the graphene plane. The last term denotes a potential shift μ associated with the carbon atoms in the random plaquettes adjacent to adatoms as shown in figure 45 (a).

With this Hamiltonian, they explored the spin relaxation time as a function of the adatom density and adatom-induced local potential shift, and focused on the expectation value of the spin z-component.

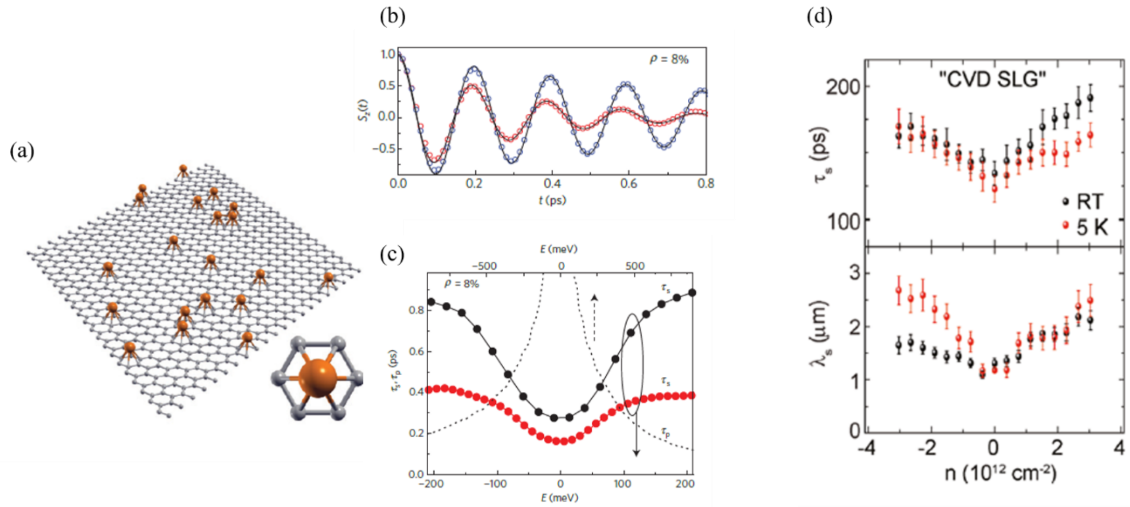

Figure 45. Spin dynamics in adatom-decorated graphene. (a) A random distribution of adatoms on graphene. (b) Time-dependent projected spin polarization S_z of charge carriers in adatom density $\rho = 8\%$ at Dirac point (red) and at 150 meV. (c) spin (symbol) and momentum (dotted in line) relaxation time as function of energy. Black (red) solid symbols indicate spin relaxation time for $\mu = 0.1\boldsymbol{\gamma_0}$($\mu = 0.2\boldsymbol{\gamma_0}$). (d) Experimental result of charge carrier dependent spin relaxation time and length[124].

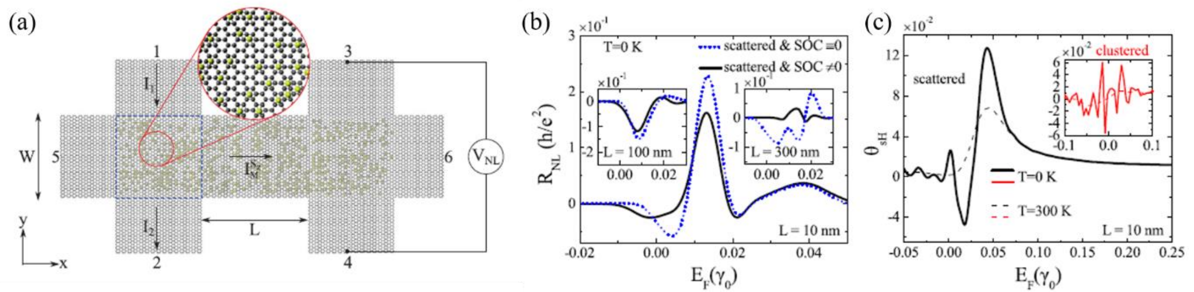

Figure 46. Spin Hall angle of Adatom-decorated graphene. (a) Schematic view of a six-terminal graphene employed to compute the nonlocal resistance and the spin Hall angle. (b) Nonlocal resistance for six-terminal graphene with scattered Au adatoms. Channel width is W=50 nm, channel lengths are L=10 nm (main), 100 nm (left inset), and 300 nm (right inset). Dotted lines are nonlocal resistance without spin-orbit coupling. (c) Spin Hall angle obtained from Landauer-Buttiker formulas for scattered graphene and clustered (inset) graphene[109].

ULSAN NATIONAL INSTITUTE OF SCIENCE AND TECHNOLOGY

Figure 45 (b) shows the behavior of spin dynamics investigated by computing the time dependence of the spin polarization for two selected energies (Dirac point and 150 meV) and adatom density $\rho = 8\%$. The spin relaxation time τ_s extracted from the fits of spin dynamics is shown in figure 45 (c). From this result, the spin relaxation time exhibited a significant energy dependence, and a V-shape was obtained for low energy with minimal spin relaxation time at Dirac point. The V-shaped spin relaxation time as functional of Fermi energy are experimentally observed as shown in figure 45 (d)

Dink Van Tuan and coworker explained the reason for this behavior by the entangled dynamics of spin and pseudospin from spin-orbit coupling, leading to the faster spin relaxation at Dirac point. Also, they suggested that spin could be manipulated by inducing psedomagnetic fields by straining graphene in this system[124].

Meanwhile, in the same group[109], the nonlocal spin Hall resistance of H-bar was numerically studied with equation (60) in adatom-decorated graphene system as shown in figure 46. They applied Kubo and Landauer-Buttiker formulas to the system (figure 46 (a)) to obtain the nonlocal resistance, the spin Hall conductivity, and angle. Consequently, the spin Hall angle in multiterminal graphene device was dependent on Fermi level, and the large spin Hall angle was observed at particular energy not Dirac point as shown in figure 46 (b), (c). These theoretical results are consistent with my experimental result in chapter 5.

Now, I am going to review the other tight-binding Hamiltonian reported by Zibo Wang and coworkers[125] for four-terminal graphene system without intrinsic spin-orbit coupling and potential shift μ due to adatoms on graphene.

They considered Rashba spin-orbit coupling to Hamiltonian, then the tight-binding Hamiltonian can be written as[125]

$$H = \sum_i \epsilon_i c_i^\dagger c_i + t \sum_{<ij>} c_i^\dagger c_j + i\lambda_R \sum_{<ij>} c_i^\dagger (\vec{s} \times \vec{d}_{ij}) c_j \qquad (61)$$

where $c_i^\dagger$ and c_i indicate the annihilation and creation operators, and λ_R is the strength of the external Rashba effect. They calculated the current flowing through the four-terminal system from the Landauer-Buttiker formula similar to Dink Van Tuan and coworkers.

Figure 47 shows the nonlocal resistance (red line) and local resistance (blue line) as function of the Fermi energy from calculation. The maximum nonlocal resistance was located at Dirac point both without (figure 47 (a)) and with (figure 47 (b)) Rashba effect. Just, the negative nonlocal resistance in figure 47 (a) becomes disappeared with the increase of Rashba spin-orbit coupling. Namely, this means that spin Hall effect with Rashba spin-orbit coupling do not affect the value of nonlocal resistance around Dirac point, mainly. This theoretical result also supports my experimental nonlocal resistance in Au-clustered graphene system, indirectly.

ULSAN NATIONAL INSTITUTE OF SCIENCE AND TECHNOLOGY

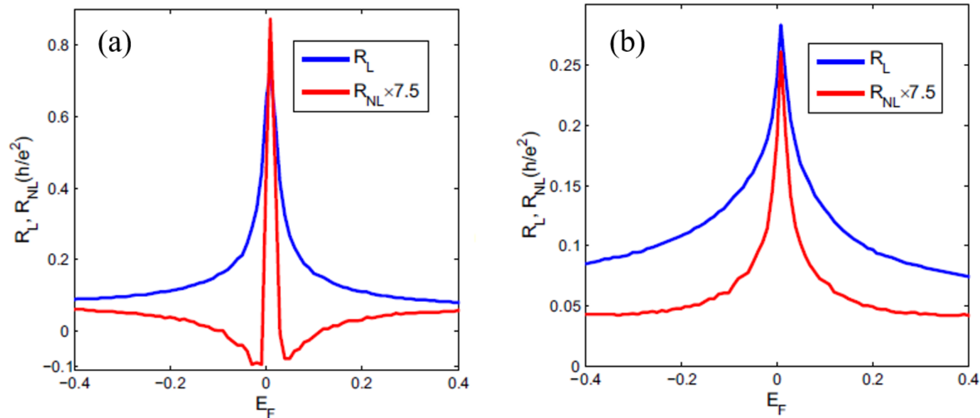

Figure 47. The local (blue line) and nonlocal (red line) resistance of 4-terminal graphene geometry (a) without and (b) with Rashba effect. In order to make the comparison clear enough, the value of nonlocal resistance is amplified 7.5 times[125].

The difference between Hamiltonian (60) and (61) is intrinsic spin-orbit coupling and local potential shift terms from adatoms on graphene. And my results indicated that nonlocal resistance in Au-decorated graphene H-bar device came from the symmetry spin-orbit scattering like Kane and Mele type than asymmetry Rashba spin-orbit coupling, corresponding to the expected results from Hamiltonian (60) with Landauer-Buttiker formula. Thus, we can infer that the intrinsic spin-orbit coupling and local potential shift terms due to adatoms on graphene paly important role to nonlocal spin Hall resistance in decorated graphene system. As shown in figure 45, the adatom-induced local potential shift influenced the spin relaxation with mixing pseudospin-related Berry phase. Therefore, the results of nonlocal resistance in decorated graphene system can be summarized as follows;

1. The gate-dependent nonlocal resistance in graphene H-bar type is not directly associated with spin Hall effect and inverses spin Hall effect.

2. The spin Hall effect occurred at the particular gate voltage due to large spin Hall angle in the gate voltage. This means it can overcome the other factors contributed to nonlocal resistance in H-bar type.

3. The possible explanation why the spin Hall effect appear at the particular charge density is spin-valley relation with the influence of adatom-induced local potential shift

These results provide important insights for the spin Hall effect in physically decorated graphene and inspire an alternative route for generating and detecting spin currents in valley systems as well as graphene.

ULSAN NATIONAL INSTITUTE OF SCIENCE AND TECHNOLOGY

VI. Metal insulator transition and the splitting of zeroth Landau level in AlO_2/Fe/graphene system.

The pristine graphene described with massless Dirac fermion[3] can be evolved into topological state or ferromagnetism by engineering the band structure of graphene through various adatoms and proximity effect of substrate[26, 65, 68]. For example, graphene on the magnetic insulator acquires strong exchange interaction, and quantized spin-polarized edge transport is expected therein[68]. The various adatoms on graphene give rise to strong spin-orbit coupling[91, 126-128] and spin scattering related Berry's phases[124]. The strong spin orbit coupling of graphene can lead to spin Hall effect[126] and quantum spin Hall state[25]. Also, it was predicted[129] that the Anderson metal insulator transition can be achieved by changing the carrier density in doped graphene.

In this study, I designed Al_2O_3/Fe (0.5 nm)/graphene structure to apply strain and exchange interaction to graphene and observed strong localization around charge neutral point and metal insulator transition with changing carrier density. Despite strong localization with disorder, quantum Hall edge state existed in the sample. Furthermore, the splitting of resistivity at charge neutral point was showed under the magnetic field. These phenomena could be understood with topological Anderson insulator state

This chapter is organized as follows: In section 6.1, I introduce a research trend of disordered graphene including proximity effect. In section 6.2, I show resistivity via gate voltage, quantum hall effect and metal insulator transition of Al_2O_3_Fe_graphene system. In section 6.3, the splitting of zeroth Landau level in resistivity with magnetic field is investigated. Finally, I discuss the behavior of magnetoresistance and the splitting of zeroth Landau level in section 6.4.

6.1 Introduction

Electron band structure of pristine graphene have been extensively studied in recent years because of its unusual transport properties[3-4, 8, 10-11], and it has been shown that the properties can be strongly modified when graphene is functionalized with various adatoms[58, 91, 102, 105, 110, 127], proximity effect from substrate[56, 65, 67-68, 123, 130], and molecules attached to surface and edge state[131]. As results, various properties were observed including spin Hall effect by spin-orbit coupling[126], valley Hall effect with broken inversion symmetry[46-47], anomalous Hall effect[65], ferromagnetism[62], strong exchange interaction[67-69], spin modulation[132], and ferroelectric field effect transistor behavior with ferroelectric substrate[130].

For a decade, there have been many studies about electronic band structure of graphene modified by adatoms (physisorption) on its surface, theoretically[58, 90-91, 105, 127, 133-134]. Chao Cao and co-workers[133]

predicted magnetic properties of graphene due to adsorbed Fe, Co, Ni and Cu atoms. In magnetic properties, Fe and Co adatoms on graphene caused local magnetic moment. Xiaojie Liu and co-workers reported[134] that transition metal (Fe, Co and Ni) adsorption on graphene exhibited strong covalent bonding with graphene, which caused large in-plane lattice distortion in graphene layer with strong magnetic moment and spin polarized density of state. Also, it was theoretically reported that adatom (disorder) on graphene can give rise to Anderson localization and transition (metal insulator transition with changing carrier density)[129, 135-136].

In this study, I deposited Fe (0.5 nm) particle on graphene surface to explore carrier transport on Fe-adatoms/graphene system and covered Al_2O_3 to protect Fe from oxidizing. Electrical transport measurements displayed strong localization around charge neutral point and metal insulator transition with changing carrier density in low temperature, which can be attributed to Anderson transition. Despite strong localization with disorder, quantum Hall edge state existed in the sample. Furthermore, the splitting of resistivity at charge neutral point appeared under the magnetic field. These phenomena will be discussed in the final last section.

6.2 Metal Insulator Transition

Figure 48 (a) shows the illustration of Al_2O_3/Fe/graphene system. Fe ~ 0.5 nm was deposited with e-beam deposition on graphene Hall bar device with a channel width (w) of ~ 1 μm and lengths (L_s) of ~ 3 μm. Then, the device was covered with Al_2O_3 ~ 20 nm by using E-beam deposition to protect Fe from oxidizing. Resistivity (ρ_{xx}) as function of gate dependent is shown in figure 48 (b). Inset is optical microscopy image of the device. Temperature dependence of field effect displayed two different regimes as in figure 48 (b). Around charge neutral point, the resistance increases with decreasing temperature, whereas metallic behavior appears at the gate voltage away from the charge neutral point. In this metallic regime of gate voltage, metal insulator transition was also observed around 55K as shown in figure 49. The estimated mobility around the charge neutral point is about 600 cm^2 / V·s at 2 K. The mobility of the Al_2O_3/Fe/graphene device dramatically decreased in comparison to the pristine graphene (~5000 cm^2 / V·s, see chapter 4). This indicates that Fe adatoms give rise to significant disorder for graphene.

Figure 50 shows magnetoresistance upon applying perpendicular magnetic field. All results display negative magneto-resistance is negative. The SdH oscillation can be observed at high charge carrier density. To find the influence of quantum interference in insulator region (at charge neutral point), I fit obtained results according to a localization theory developed for graphene, where the correction to the semiclassical resistivity is given by

ULSAN NATIONAL INSTITUTE OF
SCIENCE AND TECHNOLOGY

$$\Delta\rho(B) = -\frac{e^2\rho^2}{\pi h}\left[F\left(\frac{B}{B_\varphi}\right) - F\left(\frac{B}{B_\varphi + 2B_{inter}}\right) - 2F\left(\frac{B}{B_\varphi + B_{intra}}\right)\right]$$

$$F(\mathrm{z}) = \ln z + \psi\left(\frac{1}{2} + \frac{1}{z}\right) \qquad B_{\varphi,inter,intra} = \frac{\hbar}{4De}\tau^{-1}_{\varphi,inter,intra} \tag{61}$$

where ψ is digamma function, D is the diffusion coefficient, τ^{-1}_{inter} is intervalley scattering rate, τ^{-1}_{intra} is intravalley scattering rate, and τ^{-1}_{φ} is dephasing rate.

Fitting curves with equation (61) are shown in figure 50 (a). Here, I plot $\Delta\rho = \rho(0) - \rho(B)$ from experimental data. The dotted blue line indicates typical weak localization of graphene on SiO_2 substrate ($\tau_\varphi = 0.3\ ps$, $\tau_{inter} = 0.14\ ps$, $\tau_{intra} = 0.05\ ps$). Without changing phases coherence time (τ_φ), the dotted red line appears when both inter- and intra- valley scattering increase ($\tau_\varphi = 0.3\ ps$, $\tau_{inter} = 0.01\ ps$, $\tau_{intra} = 0.014\ ps$) as shown in figure 50 (a). Then, we can extract a value for phases coherence length $L_\varphi = \sqrt{\tau_\varphi D}$ around charge neutral point, where diffusion coefficient (D) ~0.01 was estimated from field effect properties (figure 48 (b)) with equation (11).

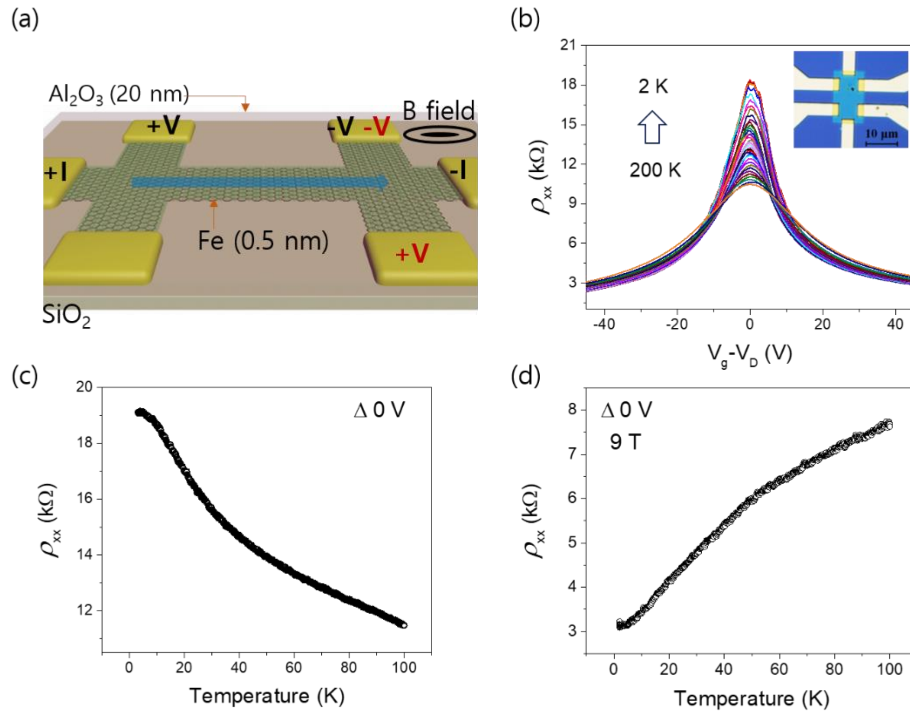

Figure 48. Hall bar geometry and charge transport for the Al_2O_3/Fe/grapehen device. (a) Schematic of the H-bar geometry of the graphene device. (b) Resistivity as function of gate voltage at various temperatures. Inset is optical microscopy of the device. (c) Resistivity at charge neutral point (CNP) measured at temperature between 2K and 100K, indicating insulator state. (d) Resistivity at charge neutral point (CNP) measured at temperature between 2K and 100K under the magnetic field of 9 T, indicating metallic state.

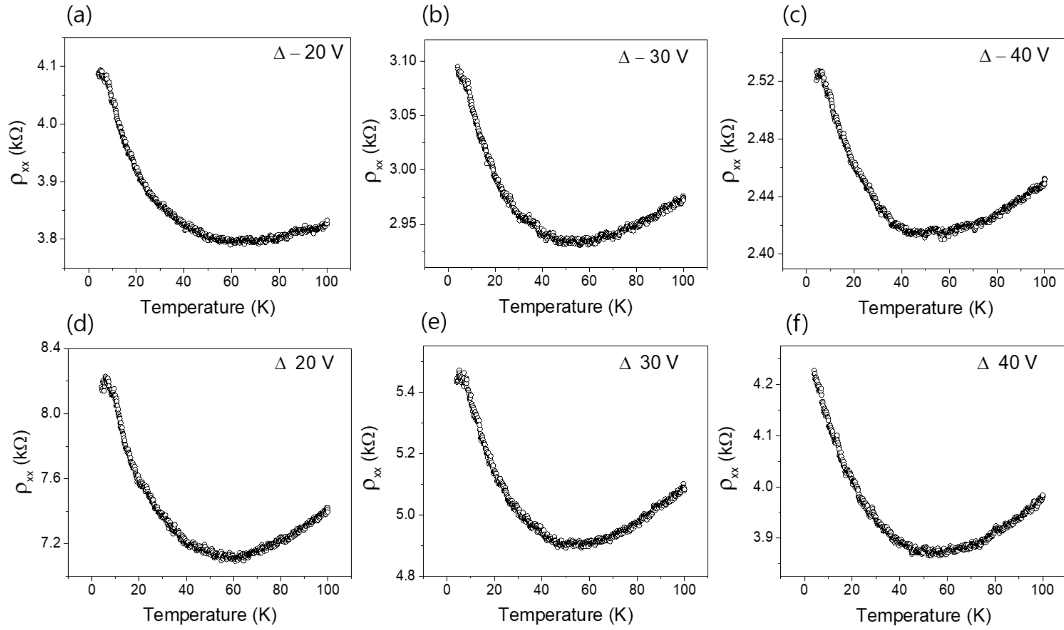

Figure 49. Metal insulator transition measured at various gate voltage for the Al_2O_3/Fe/grapehen device without magnetic field (a-f).

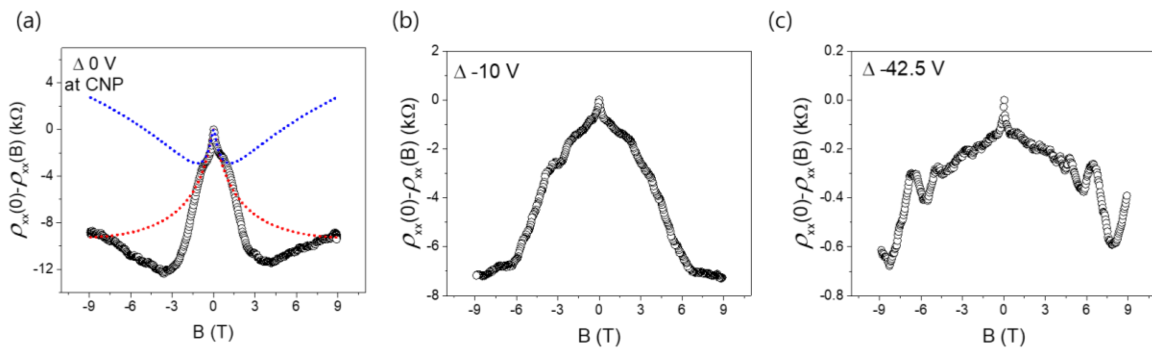

Figure 50. Magnetoresistance under the perpendicular magnetic field. (a) Negative magnetoresistance at charge neutral point (a), $V_g - V_D$= -10V (b), and $V_g - V_D$= -42.5V. The dot line indicates fitting curve with equation (61). The dotted red and blue lines are fitting curves based on equation (61).

ULSAN NATIONAL INSTITUTE OF SCIENCE AND TECHNOLOGY

The estimated phases coherence length around charge neutral point is ~ 57 nm. The localization length given by

$$\xi_D \cong L_e exp\left(\frac{\sigma_D}{e^2/h}\right) \tag{62}$$

where, L_e is the elastic length from $L_e = \sigma_D h/2e^2(\pi n)^{1/2}$, σ_D is Drude conductivity, and n is charge carrier density.

The estimation of localization length around the charge neutral point is ~3.2 nm. Thus, phases coherence length is larger than localization length, reflecting strong localization regime.

In disordered graphene, it has been already reported that the strong localization exhibits around charge neutral point. Previous works showed that disorder of sp^3-type obtained by hydrogenation and exposing ozone give rise to strong localization in low carrier density region. However, metal insulator transition was not observed by changing carrier density as observed in my study.

To compare influence of Fe adatom on graphene, I introduced Al_2O_3/graphene structure excluding Fe layer. Experimentally, there was reported [137-139] that evaporation of aluminum oxide on graphene give rise to defect in graphene.

Figure 51 (a) indicates gate dependent resistivity (ρ_{xx}) in control device measured at various temperatures. Unlike Al_2O_3/Fe/graphene system, insulator behavior was observed exhibited in all region. Giant negative magneto resistance is observed as shown in figure 51 (b), and resistivity increase with decreasing temperature at charge neutral point with $B = 9$T as shown in figure 51 (c), indicating insulator state. However, in Al_2O_3/Fe/graphene sample, metallic state appeared at charge neutral point when B =9 T, whereas insulating state existed at charge neutral point without magnetic field. And quantum Hall effect was not observed due to defects (figure 51 (d)).

However, the Al_2O_3/Fe/graphene device exhibits quantum Hall state, as shown in figure 52. Figure 52 (a) shows resistivity versus gate voltage under $B = 9$T. The inset of figure 52 (a) indicates Hall resistivity at gate 10 V. Quantum Hall state corresponding to filling factor $\nu = 2$ of Landau level is clearly visible at the magnetic field of 3T. Figure 52 (b) shows traces of $\nu = \pm 2$ state upon varying magnetic field, indicating that orbital effect induced by Fe adatom is negligible.

The possible scenario to explain strong localization with metal insulator transition and quantum Hall state is Anderson transition[140]. Yun Song and coworkers [129] theoretically predicted that the Anderson metal insulator transition can be introduced by the presence of quenched random disorder from the Anderson tight-binding model in doped graphene, and four mobility edges can be observed for the honeycomb lattice with specific disorder strength and impurity concentration.

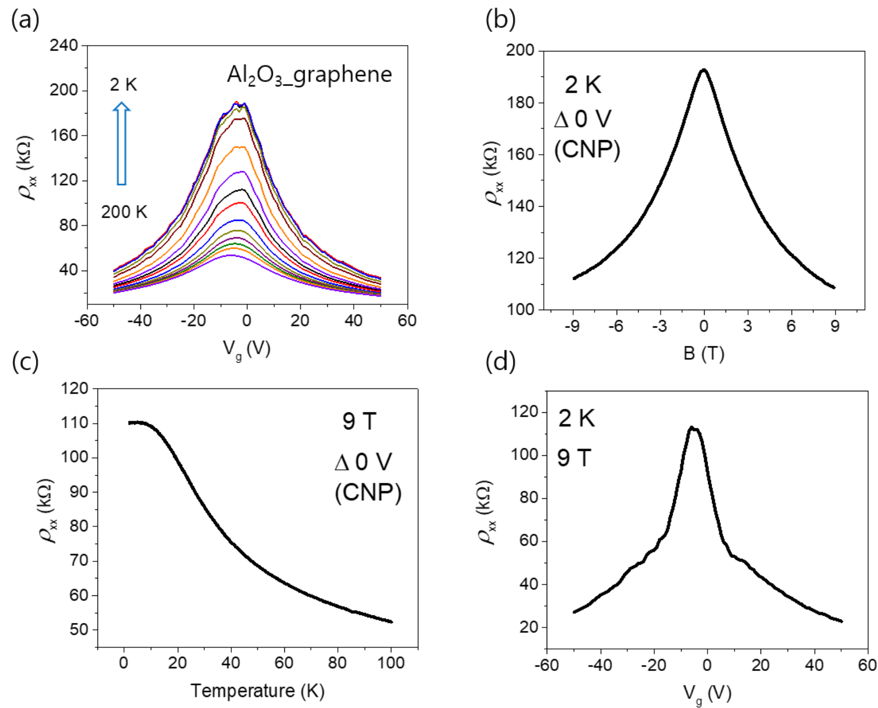

Figure 51. Transport properties of Al_2O_3/graphene device. (a) Resistivity as function of gate voltage at various temperatures. Insulator behavior can be observed in all region. (b) Giant negative magnetoresistance at CNP. (c) Temperature resistivity under magnetic field of 9 T at CNP, indicating insulator state. (d) Resistivity as functional of gate voltage under B = 9 T at 2K, showing no clear quantum Hall effect.

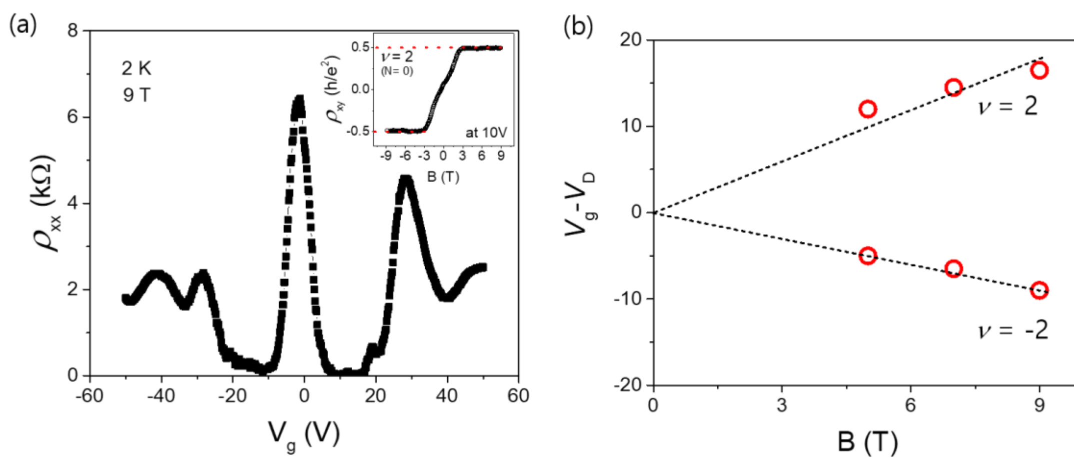

Figure 52. Quantum Hall effect of Al_2O_3/Fe/graphene device. (a) resistivity as functional of gate voltage under B = 9 T at 2K. The inset is Hall resistivity measured at gate 10 V. (b) Magnetic field dependence of the gate voltage (V_g–V_D) for ν= ±2 states.

ULSAN NATIONAL INSTITUTE OF
SCIENCE AND TECHNOLOGY

6.3 The splitting of zeroth Landau level

In high magnetic field, the ν= 0 and ν= ±1states in quantum Hall region is known as arising from the spin and valley degeneracy of the zeroth Landau level, respectively[141-143]. And, the ν= 0 state from the splitting of zeroth Landau level can be a spin-polarized state with gapless chiral edge mode, a valley-polarized state without gapless chiral edge mode or the intermediate state between spin and valley polarized[69, 144].

Figure 53 shows resistivity as function of gate voltage in Al_2O_3/Fe/graphene device at 2 K. The charge neutral point is located at 3.5 V without magnetic field. In contrast to the single peak without magnetic field, the main peak of resistivity around charge neutral point develops double-peak features at 5 T as shown in figure 53 (b). The new peak appeared at 7.5 V. However, an unprecedented phenomenon is observed with increasing magnetic field. The magnitude of new peak is no big difference between 5 T and 9T, but the magnitude of peak observed at 3.5 V decreases with increasing magnetic field. Finally, the peak observed at 3.5 V disappears at 9 T as shown figure 53 (d). Namely, the charge neutral point shift from 3.5 V to 7.5 V with high field.

As mentioned in section 2.4, it was experimentally reported that strong interfacial magnetic exchange field in the graphene/EuS heterostructure can generate the splitting of zeroth Landau level and may give rise to quantized spin-polarized edge transport[68]. Also, it was theoretically predicted that Fe adatom on graphene has spin polarized density of state and Anderson localization from localized electron and plaquette potential at impurity site[129, 136].

In my study, Fe layer on graphene cause strong (Anderson) localization around charge neutral point including metal insulator transition with changing carrier density. And quantum Hall state is present with metallic state at charge neutral point although insulator behavior was exhibited point without magnetic field at that point. Furthermore, the splitting of zeroth Landau level is being considered as spin or valley polarized edge transport state. As for these experimental results, Al_2O_3/Fe/graphene system is similar to topological Anderson insulator[135], which can be obtained by introducing impurities in a two-dimensional metal. This disorder cause metal insulator transition and extended edge state (like quantum spin Hall effect) in system. Finally, it can be explained that the charge neutral point shifts with increasing magnetic field because of Berry curvature imbalance of two k and k' point from strain and perpendicular magnetic field (see section 1.4)[34-35, 145-146].

ULSAN NATIONAL INSTITUTE OF
SCIENCE AND TECHNOLOGY

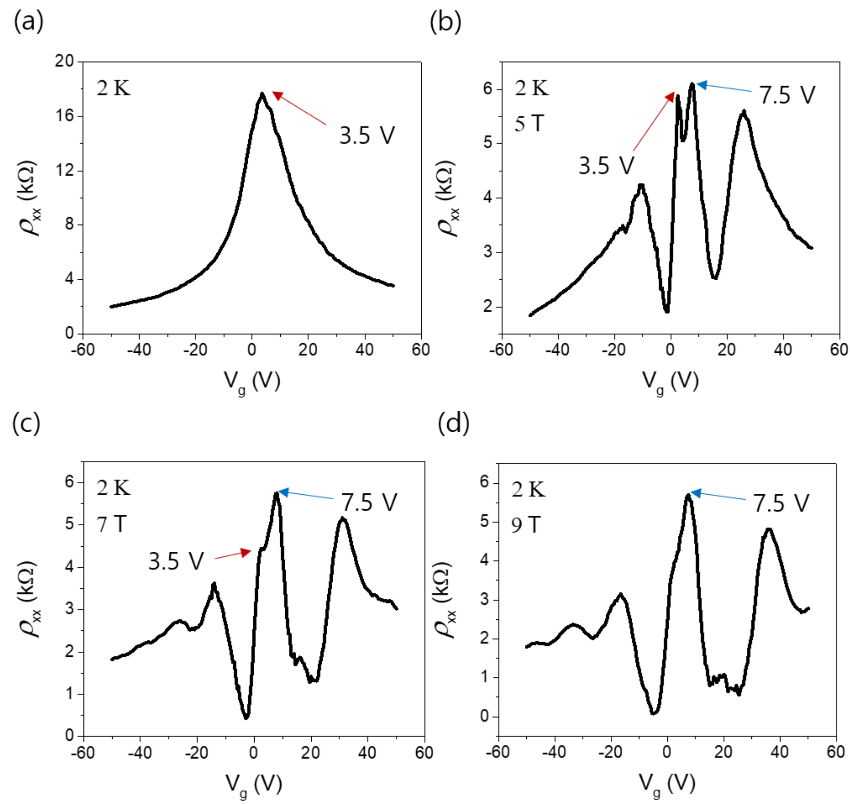

Figure 53. The splitting of zeroth Landau level in Al_2O_3/Fe/graphene device. The resistivity as a function of gate voltage measured at 2K for 0T (a), 5T (b), 7T (c), 9T (d). The splitting around charge neutral point was observed for B = 5T.

ULSAN NATIONAL INSTITUTE OF
SCIENCE AND TECHNOLOGY

6.4 Summary and discussion

In summary, I have studied the influence of Fe(0.5nm) adatoms on graphene at low temperature and high magnetic field up to 9T.

Based on these experimental results, I summarize as follows;

1. The mobility of the Al_2O_3/Fe (0.5nm)/graphene device (~600 cm^2 / V·s) dramatically decreased in comparison with the pristine graphene (~5000 cm^2 / V·s) at low temperature, meaning that Fe adatoms give rise to disorder for graphene.

2. It was observed that metal insulator transition with changing carrier density and strong localization around charge neutral point, indicating Anderson transition

3. With Anderson localization, spin polarized edge state was exhibited with metallic states under magnetic field. This phenomenon could be understood with topological Anderson insulator.

4. It was exhibited that the charge neutral point shift with increasing magnetic field, which can be explained as Berry curvature imbalance of two k and k’ point from strain and perpendicular magnetic field.

Therefore, Al_2O_3/Fe (0.5nm)/graphene system will be good candidate for Anderson transition or topological Anderson insulator.

ULSAN NATIONAL INSTITUTE OF
SCIENCE AND TECHNOLOGY

VII. Conclusion

I have studied the influence of metal (Au, Fe) adatom on graphene because the pristine graphene can be empowered to spin hall state and topological insulator from adatom. Especially, the nonlocal resistance of the adatom-decorated graphene has given rise to controversy whether it is from spin Hall effect or unknown origin.

So, I studied spin Hall effect in Au-clustered graphene Hall bar device to find origin of nonlocal resistance. Based on experimental results, I summarize the conclusion for nonlocal signal of disordered graphene as following;

1. The gate-dependent nonlocal resistance in graphene H-bar type is not directly associated with spin Hall effect because nonlocal signal can contain many contributions such as valley Hall, Ohmic potential, off-set voltage and ballistic limits.
2. The spin current is only generated at the particular gate voltage because of large spin Hall angle, overcoming the other factors contributed to nonlocal resistance.
3. The possible explanation why the spin Hall effect appear at the particular charge density is spin-valley relation with the influence of adatom-induced local potential shift

Also, I explored the transport properties of Al_2O_3/Fe (0.5nm)/graphene system under high magnetic field up to 9T at low temperature. As the results, metal insulator transition with changing carrier density, Anderson localization around charge neutral point, and spin polarized edge state with metallic state appeared. These phenomena could be understood with topological Anderson insulator. Therefore, I suggest that Al_2O_3/Fe/graphene system is good candidate for Anderson transition or topological Anderson insulator state.

These results provide important insights for spin Hall effect and topological state of graphene with metal adatom.

Reference

1. Wallace, P. R., The Band Theory of Graphite. *Physical Review* **1947,** *71* (9), 622-634.

2. Novoselov, K. S.; Geim, A. K.; Morozov, S. V.; Jiang, D.; Zhang, Y.; Dubonos, S. V.; Grigorieva, I. V.; Firsov, A. A., Electric Field Effect in Atomically Thin Carbon Films. *Science* **2004,** *306* (5696), 666.

3. Castro Neto, A. H.; Guinea, F.; Peres, N. M. R.; Novoselov, K. S.; Geim, A. K., The electronic properties of graphene. *Reviews of Modern Physics* **2009,** *81* (1), 109-162.

4. Novoselov, K. S.; Geim, A. K.; Morozov, S. V.; Jiang, D.; Katsnelson, M. I.; Grigorieva, I. V.; Dubonos, S. V.; Firsov, A. A., Two-dimensional gas of massless Dirac fermions in graphene. *Nature* **2005,** *438*, 197.

5. Semenoff, G. W., Condensed-Matter Simulation of a Three-Dimensional Anomaly. *Physical Review Letters* **1984,** *53* (26), 2449-2452.

6. Klein, O., Die Reflexion von Elektronen an einem Potentialsprung nach der relativistischen Dynamik von Dirac. *Zeitschrift für Physik* **1929,** *53* (3), 157-165.

7. Calogeracos, A.; Dombey, N., History and physics of the Klein paradox. *Contemporary Physics* **1999,** *40* (5), 313-321.

8. Katsnelson, M. I.; Novoselov, K. S.; Geim, A. K., Chiral tunnelling and the Klein paradox in graphene. *Nature Physics* **2006,** *2*, 620.

9. Schwierz, F., Graphene transistors. *Nature Nanotechnology* **2010,** *5*, 487.

10. Geim, A. K.; Novoselov, K. S., The rise of graphene. *Nature Materials* **2007,** *6*, 183.

11. Zhang, Y.; Tan, Y.-W.; Stormer, H. L.; Kim, P., Experimental observation of the quantum Hall effect and Berry's phase in graphene. *Nature* **2005,** *438*, 201.

12. Kanda, A., Experimental Approaches to graphene electron transport for deivce application. In *Physics and chemistrry of graphene* Toshiaki Enoki, T. A., Ed. 2012; pp 89-205.

13. McClure, J. W., Diamagnetism of Graphite. *Physical Review* **1956,** *104* (3), 666-671.

14. Haldane, F. D. M., Model for a Quantum Hall Effect without Landau Levels: Condensed-Matter Realization of the "Parity Anomaly". *Physical Review Letters* **1988,** *61* (18), 2015-2018.

15. Ando, M. K. a. T., electronic Properties of Monolayer and Multilayer Graphene. In *Physics of graphene*, Hideo Aoki, M. S. D., Ed. 2014; pp 173-211.

16. Andrea F. Young, Y. Z., and Philip Kim, Experimental Manifestation of Berry Phase in Graphene. In *Phyiscs of Graphene*, Hideo Aoki, M. S. D., Ed. 2014; pp 3-27.

17. Peres, N. M. R., Colloquium: The transport properties of graphene: An introduction. *Reviews of Modern Physics* **2010,** *82* (3), 2673-2700.

ULSAN NATIONAL INSTITUTE OF SCIENCE AND TECHNOLOGY

18. Cahay, S. B. a. M., *Introduction to Spincurrent*. CRC press: 2008.

19. Thomas, L. H., The Motion of the Spinning Electron. *Nature* **1926,** *117*, 514.

20. Strange, P., *Relativistic Quantum Mechanics*. Cambridge University Press: 1998.

21. Konschuh, S.; Gmitra, M.; Fabian, J., Tight-binding theory of the spin-orbit coupling in graphene. *Physical Review B* **2010,** *82* (24), 245412.

22. Gmitra, M.; Konschuh, S.; Ertler, C.; Ambrosch-Draxl, C.; Fabian, J., Band-structure topologies of graphene: Spin-orbit coupling effects from first principles. *Physical Review B* **2009,** *80* (23), 235431.

23. Boettger, J. C.; Trickey, S. B., First-principles calculation of the spin-orbit splitting in graphene. *Physical Review B* **2007,** *75* (12), 121402.

24. McClure, J. W. Y., Y., Theory of the g-factor of the current carriers in graphite single crystals. *Proc. 5th Conf. Carbon* **1962,** *1* (12).

25. Kane, C. L.; Mele, E. J., Quantum Spin Hall Effect in Graphene. *Physical Review Letters* **2005,** *95* (22), 226801.

26. Kane, C. L.; Mele, E. J., Z_2 Topological Order and the Quantum Spin Hall Effect. *Physical Review Letters* **2005,** *95* (14), 146802.

27. Lu, H.-Z.; Shen, S.-Q., Finite-Temperature Conductivity and Magnetoconductivity of Topological Insulators. *Physical Review Letters* **2014,** *112* (14), 146601.

28. Lu, H.-Z.; Shen, S.-Q. In *Weak localization and weak anti-localization in topological insulators*, SPIE NanoScience + Engineering, SPIE: 2014; p 11.

29. McCann, E.; Kechedzhi, K.; Fal'ko, V. I.; Suzuura, H.; Ando, T.; Altshuler, B. L., Weak-Localization Magnetoresistance and Valley Symmetry in Graphene. *Physical Review Letters* **2006,** *97* (14), 146805.

30. Tikhonenko, F. V.; Kozikov, A. A.; Savchenko, A. K.; Gorbachev, R. V., Transition between Electron Localization and Antilocalization in Graphene. *Physical Review Letters* **2009,** *103* (22), 226801.

31. Morozov, S. V.; Novoselov, K. S.; Katsnelson, M. I.; Schedin, F.; Ponomarenko, L. A.; Jiang, D.; Geim, A. K., Strong Suppression of Weak Localization in Graphene. *Physical Review Letters* **2006,** *97* (1), 016801.

32. Low, T.; Guinea, F., Strain-Induced Pseudomagnetic Field for Novel Graphene Electronics. *Nano Letters* **2010,** *10* (9), 3551-3554.

33. Levy, N.; Burke, S. A.; Meaker, K. L.; Panlasigui, M.; Zettl, A.; Guinea, F.; Neto, A. H. C.; Crommie, M. F., Strain-Induced Pseudo–Magnetic Fields Greater Than 300 Tesla in Graphene Nanobubbles. *Science* **2010,** *329* (5991), 544.

34. Mañes, J. L.; de Juan, F.; Sturla, M.; Vozmediano, M. A. H., Generalized effective Hamiltonian for graphene under nonuniform strain. *Physical Review B* **2013,** *88* (15), 155405.

35. Wu, Q.-P.; Liu, Z.-F.; Chen, A.-X.; Xiao, X.-B.; Miao, G.-X., Tunable Dirac points and high spin polarization in ferromagnetic-strain graphene superlattices. *Scientific Reports* **2017,** *7* (1), 14636.

ULSAN NATIONAL INSTITUTE OF SCIENCE AND TECHNOLOGY

36. Farajollahpour, T.; Phirouznia, A., The role of the strain induced population imbalance in Valley polarization of graphene: Berry curvature perspective. *Scientific Reports* **2017,** *7* (1), 17878.

37. Žutić, I.; Fabian, J.; Das Sarma, S., Spintronics: Fundamentals and applications. *Reviews of Modern Physics* **2004,** *76* (2), 323-410.

38. Jansen, R., Silicon spintronics. *Nature Materials* **2012,** *11*, 400.

39. Žutić, I.; Fuhrer, M., A path to spin logic. *Nature Physics* **2005,** *1*, 85.

40. Tombros, N.; Jozsa, C.; Popinciuc, M.; Jonkman, H. T.; van Wees, B. J., Electronic spin transport and spin precession in single graphene layers at room temperature. *Nature* **2007,** *448*, 571.

41. Han, W.; McCreary, K. M.; Pi, K.; Wang, W. H.; Li, Y.; Wen, H.; Chen, J. R.; Kawakami, R. K., Spin transport and relaxation in graphene. *Journal of Magnetism and Magnetic Materials* **2012,** *324* (4), 369-381.

42. Drögeler, M.; Volmer, F.; Wolter, M.; Terrés, B.; Watanabe, K.; Taniguchi, T.; Güntherodt, G.; Stampfer, C.; Beschoten, B., Nanosecond Spin Lifetimes in Single- and Few-Layer Graphene–hBN Heterostructures at Room Temperature. *Nano Letters* **2014,** *14* (11), 6050-6055.

43. Kamalakar, M. V.; Groenveld, C.; Dankert, A.; Dash, S. P., Long distance spin communication in chemical vapour deposited graphene. *Nature Communications* **2015,** *6*, 6766.

44. Avsar, A.; Yang, T.-Y.; Bae, S.; Balakrishnan, J.; Volmer, F.; Jaiswal, M.; Yi, Z.; Ali, S. R.; Güntherodt, G.; Hong, B. H.; Beschoten, B.; Özyilmaz, B., Toward Wafer Scale Fabrication of Graphene Based Spin Valve Devices. *Nano Letters* **2011,** *11* (6), 2363-2368.

45. Guimarães, M. H. D.; Veligura, A.; Zomer, P. J.; Maassen, T.; Vera-Marun, I. J.; Tombros, N.; van Wees, B. J., Spin Transport in High-Quality Suspended Graphene Devices. *Nano Letters* **2012,** *12* (7), 3512-3517.

46. Gorbachev, R. V.; Song, J. C. W.; Yu, G. L.; Kretinin, A. V.; Withers, F.; Cao, Y.; Mishchenko, A.; Grigorieva, I. V.; Novoselov, K. S.; Levitov, L. S.; Geim, A. K., Detecting topological currents in graphene superlattices. *Science* **2014,** *346* (6208), 448.

47. Shimazaki, Y.; Yamamoto, M.; Borzenets, I. V.; Watanabe, K.; Taniguchi, T.; Tarucha, S., Generation and detection of pure valley current by electrically induced Berry curvature in bilayer graphene. *Nature Physics* **2015,** *11*, 1032.

48. Aronov, A. G., spin injection in metals and polarization of neclei. *Nucleae Physics Institute, USSR Academy of Sciences* **1976,** *27*, 32-34.

49. Johnson, M.; Silsbee, R. H., Interfacial charge-spin coupling: Injection and detection of spin magnetization in metals. *Physical Review Letters* **1985,** *55* (17), 1790-1793.

50. Han, W.; Kawakami, R. K.; Gmitra, M.; Fabian, J., Graphene spintronics. *Nature Nanotechnology* **2014,** *9*, 794.

51. Elliott, R. J., Theory of the Effect of Spin-Orbit Coupling on Magnetic Resonance in Some Semiconductors. *Physical Review* **1954,** *96* (2), 266-279.

ULSAN NATIONAL INSTITUTE OF SCIENCE AND TECHNOLOGY

52. MI Dyakonov, V. P., Spin relaxation of conduction electrons in noncentrosymmetric semiconductors. *Soviet Physics Solid State, USSR* **1972,** *13* (12), 3023-3026.

53. Han, W.; Kawakami, R. K., Spin Relaxation in Single-Layer and Bilayer Graphene. *Physical Review Letters* **2011,** *107* (4), 047207.

54. Manchon, A.; Koo, H. C.; Nitta, J.; Frolov, S. M.; Duine, R. A., New perspectives for Rashba spin–orbit coupling. *Nature Materials* **2015,** *14*, 871.

55. Qin, Y.; Wang, S.; Wang, R.; Bu, H.; Wang, X.; Wang, X.; Song, F.; Wang, B.; Wang, G., Sizeable Kane–Mele-like spin orbit coupling in graphene decorated with iridium clusters. *Applied Physics Letters* **2016,** *108* (20), 203106.

56. Wang, Z.; Ki, D.-K.; Khoo, J. Y.; Mauro, D.; Berger, H.; Levitov, L. S.; Morpurgo, A. F., Origin and Magnitude of `Designer' Spin-Orbit Interaction in Graphene on Semiconducting Transition Metal Dichalcogenides. *Physical Review X* **2016,** *6* (4), 041020.

57. Yazyev, O. V.; Helm, L., Defect-induced magnetism in graphene. *Physical Review B* **2007,** *75* (12), 125408.

58. Boukhvalov, D. W.; Katsnelson, M. I.; Lichtenstein, A. I., Hydrogen on graphene: Electronic structure, total energy, structural distortions and magnetism from first-principles calculations. *Physical Review B* **2008,** *77* (3), 035427.

59. Červenka, J.; Katsnelson, M. I.; Flipse, C. F. J., Room-temperature ferromagnetism in graphite driven by two-dimensional networks of point defects. *Nature Physics* **2009,** *5*, 840.

60. McCreary, K. M.; Swartz, A. G.; Han, W.; Fabian, J.; Kawakami, R. K., Magnetic Moment Formation in Graphene Detected by Scattering of Pure Spin Currents. *Physical Review Letters* **2012,** *109* (18), 186604.

61. Nair, R. R.; Sepioni, M.; Tsai, I. L.; Lehtinen, O.; Keinonen, J.; Krasheninnikov, A. V.; Thomson, T.; Geim, A. K.; Grigorieva, I. V., Spin-half paramagnetism in graphene induced by point defects. *Nature Physics* **2012,** *8*, 199.

62. Giesbers, A. J. M.; Uhlířová, K.; Konečný, M.; Peters, E. C.; Burghard, M.; Aarts, J.; Flipse, C. F. J., Interface-Induced Room-Temperature Ferromagnetism in Hydrogenated Epitaxial Graphene. *Physical Review Letters* **2013,** *111* (16), 166101.

63. Lieb, E. H., Two theorems on the Hubbard model. *Physical Review Letters* **1989,** *62* (10), 1201-1204.

64. Costa, N. C.; Mendes-Santos, T.; Paiva, T.; Santos, R. R. d.; Scalettar, R. T., Ferromagnetism beyond Lieb's theorem. *Physical Review B* **2016,** *94* (15), 155107.

65. Wang, Z.; Tang, C.; Sachs, R.; Barlas, Y.; Shi, J., Proximity-Induced Ferromagnetism in Graphene Revealed by the Anomalous Hall Effect. *Physical Review Letters* **2015,** *114* (1), 016603.

ULSAN NATIONAL INSTITUTE OF SCIENCE AND TECHNOLOGY

66. Evelt, M.; Ochoa, H.; Dzyapko, O.; Demidov, V. E.; Yurgens, A.; Sun, J.; Tserkovnyak, Y.; Bessonov, V.; Rinkevich, A. B.; Demokritov, S. O., Chiral charge pumping in graphene deposited on a magnetic insulator. *Physical Review B* **2017,** *95* (2), 024408.

67. Wu, Y.-F.; Song, H.-D.; Zhang, L.; Yang, X.; Ren, Z.; Liu, D.; Wu, H.-C.; Wu, J.; Li, J.-G.; Jia, Z.; Yan, B.; Wu, X.; Duan, C.-G.; Han, G.; Liao, Z.-M.; Yu, D., Magnetic proximity effect in graphene coupled to $BiFeO_3$ nanoplate. *Physical Review B* **2017,** *95* (19), 195426.

68. Wei, P.; Lee, S.; Lemaitre, F.; Pinel, L.; Cutaia, D.; Cha, W.; Katmis, F.; Zhu, Y.; Heiman, D.; Hone, J.; Moodera, J. S.; Chen, C.-T., Strong interfacial exchange field in the graphene/EuS heterostructure. *Nature Materials* **2016,** *15*, 711.

69. Song, H.-D.; Wu, Y.-F.; Yang, X.; Ren, Z.; Ke, X.; Kurttepeli, M.; Tendeloo, G. V.; Liu, D.; Wu, H.-C.; Yan, B.; Wu, X.; Duan, C.-G.; Han, G.; Liao, Z.-M.; Yu, D., Asymmetric Modulation on Exchange Field in a Graphene/$BiFeO_3$ Heterostructure by External Magnetic Field. *Nano Letters* **2018,** *18* (4), 2435-2441.

70. Tang, C.; Cheng, B.; Aldosary, M.; Wang, Z.; Jiang, Z.; Watanabe, K.; Taniguchi, T.; Bockrath, M.; Shi, J., Approaching quantum anomalous Hall effect in proximity-coupled YIG/graphene/h-BN sandwich structure. *APL Materials* **2017,** *6* (2), 026401.

71. Sinova, J.; Valenzuela, S. O.; Wunderlich, J.; Back, C. H.; Jungwirth, T., Spin Hall effects. *Reviews of Modern Physics* **2015,** *87* (4), 1213-1260.

72. Jungwirth, T.; Wunderlich, J.; Olejník, K., Spin Hall effect devices. *Nature Materials* **2012,** *11*, 382.

73. M.I.Dyakonov and V.I. Perel, Possibility of orienting electron spins with current. *Zh.Eksp.Teor.Fiz.* **1971,** *13* (11), 657-660.

74. Hirsch, J. E., Spin Hall Effect. *Physical Review Letters* **1999,** *83* (9), 1834-1837.

75. Kato, Y. K.; Myers, R. C.; Gossard, A. C.; Awschalom, D. D., Observation of the Spin Hall Effect in Semiconductors. *Science* **2004,** *306* (5703), 1910.

76. Valenzuela, S. O.; Tinkham, M., Direct electronic measurement of the spin Hall effect. *Nature* **2006,** *442*, 176.

77. Hall, E. H., On a New Action of the Magnet on Electric Currents. *American Journal of Mathematics* **1879,** *2* (3), 287-292.

78. Hall, E. H., XVIII. On the “Rotational Coefficient” in nickel and cobalt. *The London, Edinburgh, and Dublin Philosophical Magazine and Journal of Science* **1881,** *12* (74), 157-172.

79. Karplus, R.; Luttinger, J. M., Hall Effect in Ferromagnetics. *Physical Review* **1954,** *95* (5), 1154-1160.

80. Zhang, S., Spin Hall Effect in the Presence of Spin Diffusion. *Physical Review Letters* **2000,** *85* (2), 393-396.

81. Xiao, D.; Chang, M.-C.; Niu, Q., Berry phase effects on electronic properties. *Reviews of Modern Physics* **2010,** *82* (3), 1959-2007.

ULSAN NATIONAL INSTITUTE OF
SCIENCE AND TECHNOLOGY

82. M. V. Berry, F. R. S., Quantal phase factors accompanying adiabatic changes. *Proceedings of the Royal Society of London. A. Mathematical and Physical Sciences* **1984,** *392* (1802), 45.

83. Smit, J., The spontaneous hall effect in ferromagnetics II. *Physica* **1958,** *24* (1), 39-51.

84. Berger, L., Side-Jump Mechanism for the Hall Effect of Ferromagnets. *Physical Review B* **1970,** *2* (11), 4559-4566.

85. Fisher, G. P., The Electric Dipole Moment of a Moving Magnetic Dipole. *American Journal of Physics* **1971,** *39* (12), 1528-1533.

86. Branislav K. Nikolic, L. P. Z., Satofumi Souma, Spin Currents in Semiconductor Nanostructures: A Nonequilibrium Green-Function Approach. In *The Oxford Handbook on Nanoscience and Technology: Frontiers and Advances*, Fu, A. V. N. a. Y. Y., Ed. Oxford University Press: 2010; Vol. 1, pp 814-866.

87. 이경진, 유천열, 이현우, 전류구동 스핀 동역학. In *자성재료와 스핀트로닉스*, 김희중, Ed. 한국자기학회: 2014; pp 173-206.

88. Smit, J., The spontaneous hall effect in ferromagnetics I. *Physica* **1955,** *21* (6), 877-887.

89. Berger, L., Influence of spin-orbit interaction on the transport processes in ferromagnetic nickel alloys, in the presence of a degeneracy of the 3d band. *Physica* **1964,** *30* (6), 1141-1159.

90. Castro Neto, A. H.; Guinea, F., Impurity-Induced Spin-Orbit Coupling in Graphene. *Physical Review Letters* **2009,** *103* (2), 026804.

91. Weeks, C.; Hu, J.; Alicea, J.; Franz, M.; Wu, R., Engineering a Robust Quantum Spin Hall State in Graphene via Adatom Deposition. *Physical Review X* **2011,** *1* (2), 021001.

92. Balakrishnan, J.; Kok Wai Koon, G.; Jaiswal, M.; Castro Neto, A. H.; Özyilmaz, B., Colossal enhancement of spin–orbit coupling in weakly hydrogenated graphene. *Nature Physics* **2013,** *9*, 284.

93. Abanin, D. A.; Shytov, A. V.; Levitov, L. S.; Halperin, B. I., Nonlocal charge transport mediated by spin diffusion in the spin Hall effect regime. *Physical Review B* **2009,** *79* (3), 035304.

94. Balakrishnan, J.; Koon, G. K. W.; Avsar, A.; Ho, Y.; Lee, J. H.; Jaiswal, M.; Baeck, S.-J.; Ahn, J.-H.; Ferreira, A.; Cazalilla, M. A.; Neto, A. H. C.; Özyilmaz, B., Giant spin Hall effect in graphene grown by chemical vapour deposition. *Nature Communications* **2014,** *5*, 4748.

95. Kaverzin, A. A.; van Wees, B. J., Electron transport nonlocality in monolayer graphene modified with hydrogen silsesquioxane polymerization. *Physical Review B* **2015,** *91* (16), 165412.

96. Wang, Y.; Cai, X.; Reutt-Robey, J.; Fuhrer, M. S., Neutral-current Hall effects in disordered graphene. *Physical Review B* **2015,** *92* (16), 161411.

97. Yun, H. D.; Kwak, J.; Kim, S.-Y.; Seo, H.; Bang, I. C.; Kim, S. Y.; Kang, S.; Kwon, S.-Y., High performance all-carbon composite transparent electrodes containing uniform carbon nanotube networks. *Journal of Alloys and Compounds* **2016,** *675*, 37-45.

ULSAN NATIONAL INSTITUTE OF SCIENCE AND TECHNOLOGY

98. Datta, S.; Das, B., Electronic analog of the electro-optic modulator. *Applied Physics Letters* **1990,** *56* (7), 665-667.

99. Koo, H. C.; Kwon, J. H.; Eom, J.; Chang, J.; Han, S. H.; Johnson, M., Control of Spin Precession in a Spin-Injected Field Effect Transistor. *Science* **2009,** *325* (5947), 1515.

100. Choi, W. Y.; Kim, H.-j.; Chang, J.; Han, S. H.; Koo, H. C.; Johnson, M., Electrical detection of coherent spin precession using the ballistic intrinsic spin Hall effect. *Nature Nanotechnology* **2015,** *10*, 666.

101. Chuang, P.; Ho, S.-C.; Smith, L. W.; Sfigakis, F.; Pepper, M.; Chen, C.-H.; Fan, J.-C.; Griffiths, J. P.; Farrer, I.; Beere, H. E.; Jones, G. A. C.; Ritchie, D. A.; Chen, T.-M., All-electric all-semiconductor spin field-effect transistors. *Nature Nanotechnology* **2014,** *10*, 35.

102. Gmitra, M.; Kochan, D.; Fabian, J., Spin-Orbit Coupling in Hydrogenated Graphene. *Physical Review Letters* **2013,** *110* (24), 246602.

103. Irmer, S.; Frank, T.; Putz, S.; Gmitra, M.; Kochan, D.; Fabian, J., Spin-orbit coupling in fluorinated graphene. *Physical Review B* **2015,** *91* (11), 115141.

104. Pachoud, A.; Ferreira, A.; Özyilmaz, B.; Castro Neto, A. H., Scattering theory of spin-orbit active adatoms on graphene. *Physical Review B* **2014,** *90* (3), 035444.

105. Chan, K. T.; Neaton, J. B.; Cohen, M. L., First-principles study of metal adatom adsorption on graphene. *Physical Review B* **2008,** *77* (23), 235430.

106. Marchenko, D.; Varykhalov, A.; Scholz, M. R.; Bihlmayer, G.; Rashba, E. I.; Rybkin, A.; Shikin, A. M.; Rader, O., Giant Rashba splitting in graphene due to hybridization with gold. *Nature Communications* **2012,** *3*, 1232.

107. Ahmet, A.; Jong Hak, L.; Gavin Kok Wai, K.; Barbaros, Ö., Enhanced spin–orbit coupling in dilute fluorinated graphene. *2D Materials* **2015,** *2* (4), 044009.

108. Jia, Z.; Yan, B.; Niu, J.; Han, Q.; Zhu, R.; Yu, D.; Wu, X., Transport study of graphene adsorbed with indium adatoms. *Physical Review B* **2015,** *91* (8), 085411.

109. D. Van Tuan; J.M. Marmolejo-Tejada; X. Waintal; B. K. Nikolic; S. O. Valenzuela; Roche, S., spin Hall effect and origins of nonlocal resistance in adatom-decorated graphene. *Physical Review Letters* **2016,** *117*, 176602.

110. Chen, J. H.; Jang, C.; Adam, S.; Fuhrer, M. S.; Williams, E. D.; Ishigami, M., Charged-impurity scattering in graphene. *Nature Physics* **2008,** *4*, 377.

111. Mihajlović, G.; Pearson, J. E.; Garcia, M. A.; Bader, S. D.; Hoffmann, A., Negative Nonlocal Resistance in Mesoscopic Gold Hall Bars: Absence of the Giant Spin Hall Effect. *Physical Review Letters* **2009,** *103* (16), 166601.

112. Abanin, D. A.; Morozov, S. V.; Ponomarenko, L. A.; Gorbachev, R. V.; Mayorov, A. S.; Katsnelson, M. I.; Watanabe, K.; Taniguchi, T.; Novoselov, K. S.; Levitov, L. S.; Geim, A. K., Giant Nonlocality Near the Dirac Point in Graphene. *Science* **2011,** *332* (6027), 328.

ULSAN NATIONAL INSTITUTE OF SCIENCE AND TECHNOLOGY

113. Renard, J.; Studer, M.; Folk, J. A., Origins of Nonlocality Near the Neutrality Point in Graphene. *Physical Review Letters* **2014,** *112* (11), 116601.

114. Pal, A. N.; Kochat, V.; Ghosh, A., Direct Observation of Valley Hybridization and Universal Symmetry of Graphene with Mesoscopic Conductance Fluctuations. *Physical Review Letters* **2012,** *109* (19), 196601.

115. Ojeda-Aristizabal, C.; Monteverde, M.; Weil, R.; Ferrier, M.; Guéron, S.; Bouchiat, H., Conductance Fluctuations and Field Asymmetry of Rectification in Graphene. *Physical Review Letters* **2010,** *104* (18), 186802.

116. Guimarães, M. H. D.; Zomer, P. J.; Vera-Marun, I. J.; van Wees, B. J., Spin-Dependent Quantum Interference in Nonlocal Graphene Spin Valves. *Nano Letters* **2014,** *14* (5), 2952-2956.

117. Kondou, K.; Yoshimi, R.; Tsukazaki, A.; Fukuma, Y.; Matsuno, J.; Takahashi, K. S.; Kawasaki, M.; Tokura, Y.; Otani, Y., Fermi-level-dependent charge-to-spin current conversion by Dirac surface states of topological insulators. *Nature Physics* **2016,** *12*, 1027.

118. Chen, J.-H.; Jang, C.; Xiao, S.; Ishigami, M.; Fuhrer, M. S., Intrinsic and extrinsic performance limits of graphene devices on SiO2. *Nature Nanotechnology* **2008,** *3*, 206.

119. Huertas-Hernando, D.; Guinea, F.; Brataas, A., Spin-Orbit-Mediated Spin Relaxation in Graphene. *Physical Review Letters* **2009,** *103* (14), 146801.

120. Ochoa, H.; Castro Neto, A. H.; Guinea, F., Elliot-Yafet Mechanism in Graphene. *Physical Review Letters* **2012,** *108* (20), 206808.

121. Pramanik, S.; Bandyopadhyay, S.; Cahay, M., The inequality of charge and spin diffusion coefficients. *Journal of Applied Physics* **2008,** *104* (1), 014304.

122. McCann, E.; Fal'ko, V. I., z → -z Symmetry of Spin-Orbit Coupling and Weak Localization in Graphene. *Physical Review Letters* **2012,** *108* (16), 166606.

123. Wang, Z.; Ki, D. K.; Chen, H.; Berger, H.; MacDonald, A. H.; Morpurgo, A. F., Strong interface-induced spin–orbit interaction in graphene on WS2. *Nature Communications* **2015,** *6*, 8339.

124. Tuan, D. V.; Ortmann, F.; Soriano, D.; Valenzuela, S. O.; Roche, S., Pseudospin-driven spin relaxation mechanism in graphene. *Nature Physics* **2014,** *10*, 857.

125. Wang, Z.; Liu, H.; Jiang, H.; Xie, X. C., Numerical study of the giant nonlocal resistance in spin-orbit coupled graphene. *Physical Review B* **2016,** *94* (3), 035409.

126. Park, J.; Yun, H. D.; Jin, M.-J.; Jo, J.; Oh, I.; Modepalli, V.; Kwon, S.-Y.; Yoo, J.-W., Gate-dependent spin Hall induced nonlocal resistance and the symmetry of spin-orbit scattering in Au-clustered graphene. *Physical Review B* **2017,** *95* (24), 245414.

127. Ma, D.; Li, Z.; Yang, Z., Strong spin–orbit splitting in graphene with adsorbed Au atoms. *Carbon* **2012,** *50* (1), 297-305.

128. Ferreira, A.; Rappoport, T. G.; Cazalilla, M. A.; Castro Neto, A. H., Extrinsic Spin Hall Effect Induced by Resonant Skew Scattering in Graphene. *Physical Review Letters* **2014,** *112* (6), 066601.

129. Yun, S.; Hongkang, S.; Shiping, F., The effects of disorder and interactions on the Anderson transition in doped graphene. *Journal of Physics: Condensed Matter* **2011,** *23* (20), 205501.

130. Hong, X.; Hoffman, J.; Posadas, A.; Zou, K.; Ahn, C. H.; Zhu, J., Unusual resistance hysteresis in n-layer graphene field effect transistors fabricated on ferroelectric Pb(Zr0.2Ti0.8)O3. *Applied Physics Letters* **2010,** *97* (3), 033114.

131. Zberecki, K.; Swirkowicz, R.; Wierzbicki, M.; Barnas, J., Spectacular enhancement of thermoelectric phenomena in chemically synthesized graphene nanoribbons with substitution atoms. *Physical Chemistry Chemical Physics* **2016,** *18* (27), 18246-18254.

132. Singh, S.; Katoch, J.; Zhu, T.; Meng, K.-Y.; Liu, T.; Brangham, J. T.; Yang, F.; Flatté, M. E.; Kawakami, R. K., Strong Modulation of Spin Currents in Bilayer Graphene by Static and Fluctuating Proximity Exchange Fields. *Physical Review Letters* **2017,** *118* (18), 187201.

133. Cao, C.; Wu, M.; Jiang, J.; Cheng, H.-P., Transition metal adatom and dimer adsorbed on graphene: Induced magnetization and electronic structures. *Physical Review B* **2010,** *81* (20), 205424.

134. Liu, X.; Wang, C. Z.; Yao, Y. X.; Lu, W. C.; Hupalo, M.; Tringides, M. C.; Ho, K. M., Bonding and charge transfer by metal adatom adsorption on graphene. *Physical Review B* **2011,** *83* (23), 235411.

135. Li, J.; Chu, R.-L.; Jain, J. K.; Shen, S.-Q., Topological Anderson Insulator. *Physical Review Letters* **2009,** *102* (13), 136806.

136. García, J. H.; Uchoa, B.; Covaci, L.; Rappoport, T. G., Adatoms and Anderson localization in graphene. *Physical Review B* **2014,** *90* (8), 085425.

137. Zheng, L.; Cheng, X.; Cao, D.; Wang, G.; Wang, Z.; Xu, D.; Xia, C.; Shen, L.; Yu, Y.; Shen, D., Improvement of Al2O3 Films on Graphene Grown by Atomic Layer Deposition with Pre-H2O Treatment. *ACS Applied Materials & Interfaces* **2014,** *6* (10), 7014-7019.

138. Vervuurt, R. H. J.; Karasulu, B.; Verheijen, M. A.; Kessels, W. M. M.; Bol, A. A., Uniform Atomic Layer Deposition of Al2O3 on Graphene by Reversible Hydrogen Plasma Functionalization. *Chemistry of Materials* **2017,** *29* (5), 2090-2100.

139. Tang, X.; Reckinger, N.; Poncelet, O.; Louette, P.; Ureña, F.; Idrissi, H.; Turner, S.; Cabosart, D.; Colomer, J.-F.; Raskin, J.-P.; Hackens, B.; Francis, L. A., Damage evaluation in graphene underlying atomic layer deposition dielectrics. *Scientific Reports* **2015,** *5*, 13523.

140. Evers, F.; Mirlin, A. D., Anderson transitions. *Reviews of Modern Physics* **2008,** *80* (4), 1355-1417.

141. Jiang, Z.; Zhang, Y.; Stormer, H. L.; Kim, P., Quantum Hall States near the Charge-Neutral Dirac Point in Graphene. *Physical Review Letters* **2007,** *99* (10), 106802.

142. Checkelsky, J. G.; Li, L.; Ong, N. P., Zero-Energy State in Graphene in a High Magnetic Field. *Physical Review Letters* **2008,** *100* (20), 206801.

ULSAN NATIONAL INSTITUTE OF
SCIENCE AND TECHNOLOGY

143. Giesbers, A. J. M.; Ponomarenko, L. A.; Novoselov, K. S.; Geim, A. K.; Katsnelson, M. I.; Maan, J. C.; Zeitler, U., Gap opening in the zeroth Landau level of graphene. *Physical Review B* **2009,** *80* (20), 201403.

144. Abanin, D. A.; Novoselov, K. S.; Zeitler, U.; Lee, P. A.; Geim, A. K.; Levitov, L. S., Dissipative Quantum Hall Effect in Graphene near the Dirac Point. *Physical Review Letters* **2007,** *98* (19), 196806.

145. Luk'yanchuk, I. A.; Bratkovsky, A. M., Lattice-Induced Double-Valley Degeneracy Lifting in Graphene by a Magnetic Field. *Physical Review Letters* **2008,** *100* (17), 176404.

146. Li, S.-Y.; Bai, K.-K.; Yin, L.-J.; Qiao, J.-B.; Wang, W.-X.; He, L., Observation of unconventional splitting of Landau levels in strained graphene. *Physical Review B* **2015,** *92* (24), 245302.

The list of achievements

(* co-first author)

1. "Organic Ferromagnetism: Trapping Spins in the Glassy State of an Organic Network Structure"
J. Mahmood*, J. Park*, D. Shin*, H. J. Choi, J. M. Seo, J. W. Yoo, J. B. Baek
Manuscript Submitted (2018)

2. "Solution processed ferrimagnetic insulator thin film for microelectronic spin Seebeck power conversion"
I. Oh*, J. Park*, J. Jo, M.J. Jin, M. S. Jang, K. S. Lee, and J. W. Yoo
Manuscript Submitted (2018)

3. "Gate-dependent spin Hall induced nonlocal resistance and the symmetry of spin-orbit scattering in Au-clustered graphene"
J. Park, H.D. Yun, M.J. Jin, J. Jo, I. Oh, V. Modepalli, S.Y. Kwon, J.W. Yoo
Physical Review B 95 (24), 245414 (2017)

4. "Recent Progress in Potassium Sodium Niobate Lead-free Thin Films" (*review article*)
H. J. Seog, A. Ullah, C. W. Ahn, I. W. Kim, S. Y. Lee, J. Park, S. S. Won, S.H. Kim
Journal of the Korean Physical Society 72, 1467 (2018)

5. "Synthesis of High-Quality Monolayer Graphene by Low-Power Plasma"
H. K. Hong, N. Y. Kim, A. Yoon, S. W. Lee, J. Park, J. W. Yoo, Z. Lee
Manuscript Submitted (2018)

6. "Single-Crystalline Nanobelts Composed of Transition Metal Ditellurides"
J. Kwak, Y. Jo, S. Song, J. H. Kim, S.Y. Kim, J. U. Lee, S. Lee, J. Park, K. Kim, G. D. Lee, J. W. Yoo, S. Y. Kim, Y. M. Kong, G. H. Lee, W. G. Lee, J. Park, X. Xu, H. Cheong, E. Yoon, Z. Lee and S. Y. Kwon
Advanced Materials 1707260(1-8) (2018)

7. "Highly stretchable organic thermoelectrics with an enhanced power factor due to extended localization length"

J Jo, I Oh, MJ Jin, J Park, JS Son, KS An, JW Yoo

Organic Electronics 50, 367-375 (2017)

8. "Dramatic enhancement of the saturation magnetization of a sol-gel synthesized Y3Fe5O12 by a mechanical pressing process"

MS Jang, IJ Roh, J Park, CY Kang, WJ Choi, SH Baek, SS Park, JW Yoo, ...

Journal of Alloys and Compounds 711, 693-697 (2017)

9. "Nonlocal Spin Diffusion Driven by Giant Spin Hall Effect at Oxide Heterointerfaces"

MJ Jin, SY Moon, J Park, V Modepalli, J Jo, SI Kim, HC Koo, BC Min, ...

Nano letters 17 (1), 36-43 (2016)

10. "Local crystallization and enhanced thermoelectric performance of glassy carbon induced by the electron beam irradiation"

I Oh, J Jo, J Park, J Lee, H Shin, JW Yoo

Current Applied Physics 16 (11), 1511-1516 (2016)

11. "Gate-tunable spin exchange interactions and inversion of magnetoresistance in single ferromagnetic ZnO nanowires"

V Modepalli, MJ Jin, J Park, J Jo, JH Kim, JM Baik, C Seo, J Kim, JW Yoo

ACS nano 10 (4), 4618-4626 (2016)

12. "Cobalt Oxide Encapsulated in C2N-h 2D Network Polymer as a Catalyst for Hydrogen Evolution"

J Mahmood, SM Jung, SJ Kim, J Park, JW Yoo, JB Baek

Chemistry of Materials 27 (13), 4860-4864 (2015)

13. "Organic-based magnetic semiconductor thin film of Fe (TCNQ) $_{x\sim2}$ developed by physical vapor deposition and local spin density induced core-level shifts"

J Jo, MJ Jin, J Park, V Modepalli, CY Kao, AJ Epstein, M Choi, N Park, ...

Synthetic Metals 196, 56-60 (2014)

ULSAN NATIONAL INSTITUTE OF
SCIENCE AND TECHNOLOGY

Acknowledgement

First of all, I would like to express appreciation for advice on my studies to advisor Prof. Jung-Woo Yoo. I learned a lot about the spintronics from advisor. And I was able to improve my capability for experiment and research. It is a great honor to work under Prof. Jung-Woo Yoo. Also. I would like to thank my laboratory members in Nano Spin Transport Lab and coworkers that they are Inseon Oh, Junhyeon Jo, Mi-Jin Jin. Daesung Choi, JongHyeon Choi, Jaebyeong Lee, Javeed Mahmood, Min-Sun Jang, Hyung Duk Yun. Among others, I can progress all experiment for graphene spin transport from graphene received by Dr. Yun. I think that there is very little I can do single-handed. Thanks again.

Also, I would like to express appreciation to dissertation examining committee, Prof. Soon-Yong Kwon, Prof. Ki-Suk Lee, Prof. Hosub Jin, Prof. Suk Bum Chung. I think that their thoughtful question and comments are greatly valued for my research in the future.

Lastly, I would like to specifically thank my family. They truly showed the love and devotion for me. They also supported me with all their heart during the doctor's course. If not for my family I would not have been carry doctor’s degree out.

I could earn a doctorate with the help of all these people. I am really thankful again!